Protection and Cybersecurity in Inverter-Based Microgrids

Ardavan Mohammadhassani

Dissertation submitted to the Faculty of the
Virginia Polytechnic Institute and State University
in partial fulfillment of the requirements for the degrees of

Doctor of Philosophy
in
Electrical Engineering

Ali Mehrizi-Sani, Chair
Chen-Ching Liu
Qiang Li
Daniel J. Stilwell
Hoda Eldardiry

May 15, 2023
Blacksburg, Virginia

Keywords: Cybersecurity, inverter-based resources, microgrids, power system protection

Protection and Cybersecurity in Inverter-Based Microgrids

Ardavan Mohammadhassani

(ABSTRACT)

Developing microgrids is an attractive solution for integrating inverter-based resources (IBR) in the power system. Distributed control is a potential strategy for controlling such microgrids. However, a major challenge toward the proliferation of distributed control is cybersecurity. A false data injection (FDI) attack on a microgrid using distributed control can have severe impacts on the operation of the microgrid. Simultaneously, a microgrid needs to be protected from system faults to ensure the safe and reliable delivery of power to loads. However, the irregular response of IBRs to faults makes microgrid protection very challenging. A microgrid is also susceptible to faults inside IBR converters. These faults can remain undetected for a long time and shutdown an IBR. This dissertation first proposes a method that reconstructs communicated signals using their autocorrelation and cross-correlation measurements to make distributed control more resilient against FDI attacks. Next, this dissertation proposes a protection scheme that works by classifying measured harmonic currents using support vector machines. Finally, this dissertation proposes a protection and fault-tolerant control strategy to diagnose and clear faults that are internal to IBRs. The proposed strategies are verified using time-domain simulation case studies using the PSCAD/EMTDC software package.

Protection and Cybersecurity in Inverter-Based Microgrids

Ardavan Mohammadhassani

(GENERAL AUDIENCE ABSTRACT)

Renewable energy resources, such as wind, solar, and geothermal, are interfaced with the grid using DC-to-AC power electronic converters, popularly known as inverters. These "inverter-based resources (IBR)" are mostly distributed and located near consumers. During outages, IBRs can be used to provide power to customers. This gives developers the idea of integrating IBRs in microgrids. A microgrid is a miniature grid that consists of IBRs and customers. A microgrid is normally connected to the grid but can disconnect from the grid and operate on its own. To run efficiently, a microgrid uses fast and reliable communication between IBRs to create a high-performance distributed control strategy. However, this creates cybersecurity concerns for microgrids. This dissertation proposes a cybersecure distributed control strategy to make sure microgrids can keep their advantages. This dissertation also proposes a protection method that relies on machine learning to clear short circuits in the microgrid. Finally, this dissertation proposes a strategy to diagnose failures inside IBRs and ride through them. The proposed solutions are verified using the industry-grade simulation software PSCAD/EMTDC.

To my parents, Sholeh and Masoud.

Acknowledgments

What, without asking, hither hurried whence?
And, without asking, whither hurried hence!
Another and another Cup to drown
The Memory of this Impertinence!
– Omar Khayyam, Persian Philosopher and Mathematician

Omar Khayyam lived in 11th century Persia. Yet, those who seek his loyalty, find it everbounding. Aye, I have felt weak and cast aside. Yet, in this infinite pursuit of This and That endeavour and dispute, I have never known defeat. Indeed, I have learned from the master himself: better be merry with the fruitful grape than sadden after none, or bitter, fruit.

I would like to begin by expressing my sincere gratitude toward my advisor, Dr. Ali Mehrizi-Sani. Without his support, I would have achieved only little. I would also like to thank my committee, Drs. Liu, Li, Stilwell, and Eldardiry for their help and support during my studies. I owe my parents everything. They taught me to be strong, ethical, and fearless. I also want to acknowledge my dear friend, Nick Skoff, who made my transition into the U.S. much easier. Carter, thank you for being such a kind person and helping me in my moments of need. Yousef, thank you for the conversations and support. Fabrizio and Beatrice, you will always have a special place in my heart. Faris and Raja', you are lovely people and I appreciate our friendship dearly. To my Albanian friends, Arba, Jonilda, and Sara: You are great people and I wish you all the best! Finally, I also want to acknowledge all my other friends at PEC.

Contents

List of Figures xi

List of Tables xv

1 Introduction 1

1.1 The Emergence of Microgrids 2

1.1.1 Grid-Connected Control 2

1.1.2 Islanded Control 3

1.2 Challenges in Microgrid Control and Operation 4

1.2.1 Cybersecurity 5

1.2.2 Protection 6

1.3 Problem Statement and Proposed Solution 6

1.4 Research Objectives 8

1.5 Dissertation Outline 9

2 Cybersecure Distributed Control of Microgrids 10

2.1 Proposed IBR Coordination Using CSPM 12

2.1.1 Basics of CSPM 12

2.1.2 Microgrid Control Using CSPM 14

2.1.3 CSPM Operation Under FDI Attacks 16

2.2 Overview of Signal Reconstruction Using Autocorrelation and Cross-Correlation . . . 18
2.2.1 Autocorrelation and Cross-Correlation . . . 18
2.2.2 Overview of the Classic Reconstruction Approach . . . 19
2.2.3 Overview of the SDP-Based Reconstruction Approach . . . 20
2.3 Proposed Resilient CSPM Strategy . . . 21
2.3.1 Proof . . . 21
2.3.2 Proposed Resilient CSPM . . . 24
2.3.3 Computational Efficiency . . . 24
2.4 Performance Evaluation . . . 26
2.4.1 Case 1: Corruption in One Tracking Error . . . 28
2.4.2 Case 2: Corruption in Multiple Tracking Errors . . . 29
2.4.3 Case 3: Impact of Noise Power . . . 30

3 Protection of Microgrids Against System Faults 31

3.1 Introduction . . . 31
3.2 Overview of Microgrid Protection Using Harmonic Current Injection 34
3.2.1 Overview of the Harmonic Current Injection Strategy . . . 34
3.2.2 Overview of the Directionality Element . . . 36
3.2.3 Overview of the Directional Relay Coordination . . . 38
3.3 Proposed SVM-Based Protection Scheme . . . 38
3.3.1 Motivation . . . 38

3.3.2 Overview of Classification Using SVM 39
3.3.3 Problem Formulation 42
3.3.4 Proposed SVM-Based Directional Relaying 43
3.3.5 Acquisition of Training Data 44
3.4 Performance Analysis 47
3.4.1 Model Verification 47
3.4.2 Fault Type 47
3.4.3 Fault Resistance 48
3.4.4 Performance Comparison 50

4 Protection of IBRs Against OC Converter Faults **51**

4.1 Introduction 51
4.2 Basics of Operation 55
4.2.1 Steady-State Operation 55
4.2.2 Dynamic Modeling 57
4.3 MMC Operation under OC SM Faults 59
4.3.1 S_u OC Fault 60
4.3.2 S_l OC Failure 60
4.3.3 Simultaneous S_u and S_l OC Failures 61
4.4 Proposed OC SM Fault Diagnosis Method 62
4.4.1 Capacitor Voltage Balancing During OC SM Failures . . . 62
4.4.2 OC SM Fault Diagnosis Using SVM 65

4.5 Performance Evaluation 69

4.5.1 Training Data Acquisition and Statistical Analysis 69

4.5.2 Case 1: S_u Fault in SM_{ua1} 71

4.5.3 Case 2: S_l Fault in SM_{ua1} 73

4.5.4 Case 3: Simultaneous S_u and S_l Faults in SM_{ua1} 74

4.5.5 Performance Comparison 75

4.5.6 Parametric Sensitivity to Parameter Changes 78

5 Fault-Tolerant Control of IBRs Under OC Faults **79**

5.1 Proposed FT SHE Waveform Design Procedure 83

5.1.1 Overview of the $(2N + 1)$-Level SHE 83

5.1.2 Proposed FT SHE 85

5.2 Proposed MPC-Based Strategy for Circulating Current Control . 87

5.3 Performance Evaluation: Offline 92

5.3.1 Steady-State Performance 92

5.3.2 Response to Change in m_a 92

5.3.3 Response to HBSM Failures 95

5.4 Performance Evaluation: Real-Time 96

5.4.1 Steady-State Performance 97

5.4.2 Response to HBSM Failures 98

5.4.3 Performance Comparison 100

6 Conclusions **101**

6.1 Summary 101

6.2 Conclusions 102

6.3 Contributions 104

6.4 Future Work 104

6.5 Publications 106

6.5.1 Journal Articles 106

6.5.2 Conference Papers 106

Bibliography **108**

List of Figures

2.1 Block diagram representation of CSPM for a sample closed-loop control system. 12

2.2 An example radial microgrid with N IBRs demonstrating the system-level implementation of CSPM. 14

2.3 The proposed IBR control strategy using CSPM. 15

2.4 A single-phase LCL filter. 22

2.5 Resilient IBR control using CSPM including the proposed signal reconstruction module. 25

2.6 Employed study system. 25

2.7 Simulation results for IBR2 under Case 1. 26

2.8 Simulation results for IBR2 under Case 2. 27

2.9 Simulation results for IBR3 under Case 2. 28

2.10 Simulation results for IBR2 under Case 2. 29

3.1 Block diagram demonstration of the IBR controller proposed in [32]. 34

3.2 Overview of the directional element logic proposed in [32]. 37

3.3 Sample linear training dataset. 39

3.4 Proposed SVM-based directional relaying scheme. 42

3.5 Proposed SVM-based directional relaying scheme. 43

3.6 Employed study system: an IBR is connected to all buses 1–14. . 45

3.7 Measured harmonic currents by forward- and reverse-looking relays under a bolted ABC-G fault at the midpoint of line 9–10: (a) R910, (b) R109, (c) R89, (d) R98, (e) R1011, and (f) R1110. . . . 48

3.8 SVM (a) directionality and (b) zone detection scores for forward- and reverse-looking relays under a bolted ABC-G fault at the midpoint of line 9–10. 48

3.9 Harmonic current measurements by relay R56 under (a) ABC-G, (b) B-C, and (c) A-G faults at the midpoint of line 5–6. 49

3.10 SVM (a) directionality and (b) zone detection scores for relay R56 under ABC-G, B-C, and A-G fault at the midpoint of line 5–6. . . 49

3.11 Performance summary for relay R87 under an ABC-G fault with a fault resistance of 10 Ω at the midpoint of line 8–7: (a) harmonic current measurements, (b) directionality score, and (c) zone detection score. 50

4.1 Generic topology of a three-phase MMC. 54

4.2 Equivalent circuit for a single-phase MMC with $N = 2$. 58

4.3 OC SM fault cases in MMCs with HBSMs: (a) S_u OC failure, (b) S_l OC failure, and (c) simultaneous S_u and S_l OC failures. 59

4.4 Sample graphical representations of (a) $f(N_{\text{sum}}^{\text{discharge}})$ during normal operation and (b) $N_{\text{sum}}^{\text{discharge}}$ during normal and faulty operation. 64

4.5 A linearly-separable sample training data. 67

4.6 Proposed SVM-based OC SM fault diagnosis method. 68

4.7 Learning curves for (a) detection and localization SVM and (b) classification SVM of SM_{ua1}. 70

4.8 Simulation results after applying a S_u fault in SM_{ua1}: (a) capacitor voltages of SMs in the upper arm of phase a, (b) $N_{\text{sum}}^{\text{discharge}}$ for SMs in the upper arm of phase a, (c) detection and localization flag for SMs in the upper arm of phase a, (d) $N_{\text{sum}}^{\text{charge}}$ for SMs in the upper arm of phase a, and (e) classification flag for SM_{ua1}. 72

4.9 Simulation results after applying a S_l fault in SM_{ua1}: (a) capacitor voltages of SMs in the upper arm of phase a, (b) $N_{\text{sum}}^{\text{discharge}}$ for SMs in the upper arm of phase a, (c) detection and localization flag for SMs in the upper arm of phase a, (d) $N_{\text{sum}}^{\text{charge}}$ for SMs in the upper arm of phase a, and (e) classification flag for SM_{ua1}. 74

4.10 Simulation results after applying S_u and S_l faults in SM_{ua1}: (a) capacitor voltages of SMs in the upper arm of phase a, (b) $N_{\text{sum}}^{\text{discharge}}$ for SMs in the upper arm of phase a, (c) detection and localization flag for SMs in the upper arm of phase a, (d) $N_{\text{sum}}^{\text{charge}}$ for SMs in the upper arm of phase a, and (e) classification flag for SM_{ua1}. . . 76

4.11 Simulation results after applying S_u and S_l faults in SM_{ua1} with $C_{\text{SM}}^{\text{new}} = 0.8C_{\text{SM}}$ and $L_{\text{arm}}^{\text{new}} = 1.2L_{\text{arm}}$: (a) capacitor voltages of SMs in the upper arm of phase a, (b) $N_{\text{sum}}^{\text{discharge}}$ for SMs in the upper arm of phase a, (c) detection and localization flag for SMs in the upper arm of phase a, (d) $N_{\text{sum}}^{\text{charge}}$ for SMs in the upper arm of phase a, and (e) classification flag for SM_{ua1}. 77

5.1 $V_{o,i}$ waveform during (a) normal operation, (b) an HBSM failure, and (c) FT operation when $M = 1$. 84

5.2 Proposed process for designing the FT SHE waveforms. 88

5.3 Proposed MPC-based circulating current controller. 89

5.4 Control loop for generating i^*_{diff}. 91

5.5 Steady-state simulation results for (a) $v^a_{cu,j}$ and $v^a_{cl,j}$, (b) $i_{\text{diff,a}}$, (c) $i_{o,i}$, (d) $V_{o,i}$, and (e) harmonic spectrum of $V_{o,i}$. 93

5.6 Simulation results for step change in m_a: (a) $v^a_{cu,j}$ and $v^a_{cl,j}$, (b) $i_{\text{diff,a}}$, (c) $i_{o,i}$, (d) $V_{o,i}$, and (e) harmonic spectrum of $V_{o,i}$ with $m_a = 1$. 94

5.7 Simulation results after an HBSM failure in phase a: (a) $v^a_{cu,j}$ and $v^a_{cl,j}$, (b) $i_{\text{diff,a}}$, (c) $i_{o,i}$, (d) $V_{o,i}$, and (e) harmonic spectrum of $V_{o,a}$. 95

5.8 Real-time steady-state results for (a) $v^a_{cu,j}$ and $v^a_{cl,j}$, (b) $i_{\text{diff,a}}$, (c) $i_{o,i}$, (d) $V_{o,i}$, and (e) harmonic spectrum of $V_{o,a}$ during normal operation. 97

5.9 Real-time results after an HBSM failure in phase a: (a) $v^a_{cu,j}$ and $v^a_{cl,j}$, (b) $i_{\text{diff,a}}$, (c) $i_{o,i}$, (d) $V_{o,i}$, and (e) harmonic spectrum of $V_{o,a}$ during FT operation. 99

List of Tables

3.1 Optimal Injection Patterns for the Employed Study System 45

3.2 Performance Comparison between CS-Based Protection and the Proposed Scheme 49

4.1 Effects of S_u OC Failure on MMC Operation 60

4.2 Effects of S_l OC Failure on MMC Operation 61

4.3 Effects of Simultaneous S_u and S_l OC Failures on MMC Operation 61

4.4 Simulation Parameters 71

4.5 Performance Comparison with other Proposed Methods 75

5.1 Solution Summary for the Proposed FT SHE during Normal Operation 86

5.2 Solution Summary for the Proposed FT SHE during FT Operation 87

5.3 Performance Comparison with Recently Proposed Methods 100

Chapter 1

Introduction

Traditionally, the power grid, henceforth known as the grid, relies on synchronous generators (SG) to convert mechanical energy into electrical energy. SGs have an inherent capability to control their output voltage and frequency. This enables the stable operation of the grid through the strong disturbance rejection capabilities of the SGs [1]. However, the grid is experiencing a growing trend today for the large-scale integration of inverter-based resources (IBR). IBRs operate very differently from SGs and this poses various challenges toward the secure and stable operation of the future grid [2], [3].

Most IBRs today operate in the grid-following (GFL) mode, where they synchronize to grid voltage and frequency to start injecting power. GFL IBRs cannot regulate their output voltage and frequency and their growing integration in the grid makes the grid more sensitive to disturbances [4], [5]. An emerging solution to this issue is the grid-forming (GFM) technology. Similar to an SG, a GFM IBR can control its output voltage and frequency. Adding more GFM IBRs to the grid adds more synthetic inertia to the grid and reduces grid sensitivity to disturbances [6]–[11].

This work focuses on addressing protection and cybersecurity challenges in microgrids. Microgrids are the building block of the future grid and their efficient control and operation is essential for transitioning into the future grid.

1.1 The Emergence of Microgrids

IBRs are most prevalent in the power distribution system. They are located near the loads that they serve. Therefore, developers can integrate IBRs within microgrids. A microgrid is a group of interconnected loads and IBRs that act as a single controllable entity to the grid. A microgrid normally operates in connection to the grid. However, it can disconnect from the grid during abnormal conditions and operate autonomously in the islanded mode. Therefore, a microgrid can increase grid reliability and resiliency by maintaining the supply of power to loads when the grid is unavailable [12].

A microgrid can be thought of as a miniature grid and the same control hierarchy in place for the grid also applies to a microgrid. The rest of this section discusses microgrid control in its two distinct modes: (i) grid-connected and (ii) islanded [13], [14].

1.1.1 Grid-Connected Control

In the grid-connected mode of operation, the IBRs operate in the GFL mode and supply power to serve the nearby loads. The dynamics of IBR control in this mode is strictly dependent on grid strength. Grid strength is measured using short-circuit ratio (SCR) at the point of common coupling (PCC). In the grid-connected mode of operation, the hosting utility grid may also ask IBRs to provide ancillary support at the PCC, depending on the size of IBRs and their proximity to the PCC.

1.1.2 Islanded Control

Hierarchical microgrid control becomes activated when the microgrid disconnects from the bulk grid and starts to operate in the islanded mode. In this mode of operation, the microgrid controller must tightly control voltage and frequency while maintaining balance between generation and load. The three levels of control in this mode of operation, i.e., primary, secondary, and tertiary are discussed as follows.

Primary Control

Primary control has the fastest response time and refers to the linear IBR controllers that must detect islanding conditions. To do so, a number of IBRs usually operate as GFM units, while the rest operate as GFL units. The GFM units regulate voltage and frequency throughout the microgrid so that the GFL units can synchronize to those measurements and maintain their normal operation. The GFM units typically use droop control to regulate frequency according to real power and voltage in relationship with reactive power. This concept is adapted from the typical primary control approach for SGs in the bulk grid. However, a microgrid uses very short lines with very low X/R ratios. Therefore, real and reactive powers are not decoupled in microgrids. This makes droop control less efficient for controlling GFM units in the islanded mode of operation. A microgrid also experiences frequent changes in its operating conditions. This adversely impacts the response of GFL units as their control systems use fixed gains that are designed for a fixed range of operation. To address these issues, researchers propose various novel high-performance control systems for primary control of GFM and GFL units in islanded microgrids.

Secondary Control

Secondary comes after primary control and has a slower operating time frame. Secondary control further adjusts the set points for the GFM units after primary control reaches the steady state to make sure voltage and frequency do not violate their limits. The slower response time of secondary control also decouples it from primary control and reduces bandwidth requirements for the communication system as secondary control needs sampled measurements from the microgrid.

Tertiary Control

Tertiary control is the last layer of control and is the slowest of all in the microgrid control hierarchy. Tertiary control performs optimal power flow according to weather and load forecasts and the status of IBRs while minimizing losses in the microgrid.

1.2 Challenges in Microgrid Control and Operation

Apart from needing a high-performance controller, a microgrid must also be protected from cyberattacks and faults in its boundaries. However, microgrid protection is very challenging as IBRs respond very differently to faults and they are also susceptible faults inside their converters [15], [16]. A microgrid is also a cyber-physical system that inherits both information technology (IT) and operational technology (OT) vulnerabilities. This creates several entry points for adversaries to conduct cyberattacks on microgrids. Therefore, cybersecurity is critical for stable microgrid operation [17]. The rest of this section analyzes these two issues in more detail.

1.2.1 Cybersecurity

Currently, the hierarchical control of microgrids is implemented using the centralized architecture. However, centralized control has the following limitations:

1. heavy computational burden;
2. frequent redesign requirements;
3. single point of failure;
4. extensive communication needs.

A decentralized control architecture can potentially address the above issues by allowing the IBR controllers to operate on their own. However, this means that subsystem interactions are not considered in the decentralized architecture. A distributed architecture, however, addresses this issue by enabling communication between the IBR controllers to make them reach a concensus. However, it has cybersecurity concerns [18].

A microgrid is a cyber-physical system. The cyber layer in a microgrid comprises the communication infrastructure as well as various software applications for monitoring and control. The physical layer refers to the physical infrastructure of the microgrid consisting of components such as IBRs, loads, and intelligent electronic devices (IED). A microgrid inherits vulnerabilities from both layers. An intrusion into a weakly secure communication channel provides an adversary the ability to conduct false data injection. A malicious firmware upgrade on an IBR can grant an adversary access over its control system. A cyberattack on distributed control can have severe outcomes as a single attack can propagate quickly throughout the microgrid. This work contributes to adding cybersecurity to distributed control of microgrids.

1.2.2 Protection

The ultimate goal of any protection scheme is to detect and isolate faults quickly while minimizing outage span [19]. This is accomplished by properly coordinating protective relays in a microgrid using a sensitive and selective protection scheme. However, the maximum amount of current drawn from an IBR is usually between 120%–150% of its rated current [20]. This means that the amount of available fault current in a microgrid is significantly different in grid-connected and islanded modes of operation. Conventionally, most protection devices in the distribution system rely on overcurrent schemes. Therefore, coordinating conventional protection devices in microgrids becomes nearly impossible. Additionally, the dynamic response of an IBR to faults depends completely on its mode of operation, i.e., GFL or GFM [21]. These issues render designing conventional protection schemes infeasible for microgrids. Microgrids are also susceptible to faults on the power electronic devices inside IBRs. These faults are difficult to diagnose and potentially degrade the power quality produced by IBRs and lead to their shutdown [22]. Hence, new microgrid protection schemes should be proposed that address these two problems to ensure the stable operation of microgrids.

1.3 Problem Statement and Proposed Solution

A high-performance distributed control system could potentially address control challenges in a microgrid and enable its efficient operation. However, distributed control is highly susceptible to cyberattacks, especially FDI attacks, that could potentially disrupt its operation. However, ensuring cybersecurity in distributed control is challenging. The lack of information about microgrid components as

well as the distributed control itself makes attack detection and mitigation very difficult. Therefore, model-free techniques are more suitable for designing cybersecure distributed control strategies. Simultaneously, a microgrid should also be protected from faulty components that may appear on a system level as well as on a converter level. Conventional protection schemes are not applicable to microgrids, especially in the islanded mode of operation. Hence, novel techniques must be proposed to maintain safe and reliable delivery of power to loads. Converter faults, e.g., open-circuit (OC) switch faults, are also very common as IBRs typically use insulated-gate bipolar transistors (IGBT) switches in their converters that are very fragile and prone to OC faults. OC faults are hard to detect and isolate and may remain in the converter for long period of times. OC faults deteriorate the power quality of converters and eventually lead to their shut down. Such converter faults must be diagnosed and rode through to prevent IBR outages in a microgrid that may lead to its cascading failure.

This dissertation addresses the cybersecurity in distributed control by proposing a signal reconstruction module for IBRs that relies on the autocorrelation of remote signals in addition to their cross-correlation with similar local measurements. By reconstructing corrupted remote signals before passing them to the IBR control system, the proposed method ensures that the employed distributed control strategy remains resilient to FDI attacks on its communication links.

Microgrid protection is address in this dissertation via two proposed solutions. System protection is ensured in a fast and reliable manner by using support vector machines (SVM) to interpret measured harmonic currents that are injected by IBRs only when a system fault occurs in the microgrid. The proposed method is a nonpilot directional method that can enable relay coordination in

a microgrid without needing a dedicated communication infrastructure. Protection against OC IGBT faults in IBRs is performed using SVM but using a novel trick. The capacitors inside IBRs respond differently to the different types of OC faults. Hence, the capacitor voltage balancing algorithm of IBRs blindly tries to charge or discharge the capacitors. The patterns emerging from this particular phenomenon is used by SVM to diagnose the OC fault and activate the protection system. To close this loop and maintain normal operation of the converter afterward, this dissertation also proposes a fault-tolerant (FT) control strategy implemented using model predictive control. The proposed strategy ensures the seamless transition into the fault-tolerant mode of operation without the need for redundant components.

1.4 Research Objectives

The research objectives of this dissertation are as below:

1. To develop a cybersecure distributed control scheme for microgrids that is resilient to FDI attacks;
2. To develop a fast and reliable system protection strategy for islanded microgrids;
3. To develop a protection strategy for IBRs to detect and isolate OC converter faults;
4. To develop an FT control strategy to ride through OC converter faults.

1.5 Dissertation Outline

This dissertation covers 6 chapters. The material covered in each chapter is as follows.

Chapter 2 presents the proposed cybersecure distributed control strategy. This chapter first discusses the fundamentals behind the employed control strategy. Next, chapter 2 presents the theory behind signal reconstruction using autocorrelation and cross-correlation measurements. Finally, this chapter discusses the application of this particular signal reconstruction method to microgrids using distributed control and how it increases their resiliency against FDI attacks.

Chapter 3 presents the proposed nonpilot directional protection scheme. This chapter first discusses the employed control strategy to inject harmonic currents during faults and then presents the base method used to implement protection coordination by measuring harmonic currents. Next, this chapter presents the motivation behind the proposed protection strategy and formulates this problem. Finally, chapter 3 presents the proposed SVM-based protection strategy.

Chapter 4 presents the proposed strategy to protect IBRs against OC converter faults. This chapter first discusses the operation of converters under OC faults. Finally, it proposes an SVM-based method to detect, locate, and classify such faults within converters.

Chapter 5 presents the design of an FT control strategy to maintain normal converter operation after OC SM faults are diagnosed.

Chapter 6 provides the summary, contributions, and conclusions of this dissertation. It also provides suggestions on future work.

Chapter 2

Cybersecure Distributed Control of Microgrids

A microgrid experiences frequent variations in its topology and operating conditions. This adversely impacts the performance of IBR controllers as they are designed for a specific range of operation [4], [13]. To address this issue, references [24]–[26] propose set point modulation (SPM) techniques to improve microgrid control under varying operating conditions. SPM can be implemented hierarchically in a centralized, decentralized, or distributed framework. However, centralized and decentralized architectures have limitations, as explained in Chapter 1. Using this, [27] proposes a distributed implementation of SPM called coordinated SPM (CSPM) to improve the response of a microgrid providing ancillary services as a virtual power plant. However, the presence of communication in CSPM makes it vulnerable to cyberattacks including false data injection (FDI) [28].

An FDI attack is typically realized via a man-in-the-middle (MitM) attack, where

Portions of this chapter are submitted as

[23] B. Choudhury, A. Mohammadhassani, B. Alexander, R. Iyer, A. Mehrizi-Sani, J. H. Reed, and V. K. Shah, "Control coordination in inverter-based microgrids using AoI-based 5G schedulers," IET Smart Grid, Mar. 2023, under review.

an attacker is placed between two IBRs that are communicating with each other. This usually starts with an attacker installing Trojan horse malware on a device within the IBR communication network through phishing to bypass the security mechanisms of that network [29]. From this point onward, the attacker has control over the signals communicated by the IBR, where conducting an FDI begins. An FDI attack on CSPM disrupts its operation by corrupting the communicated tracking error signals. However, designing attack detection and mitigation methods is challenging for distributed control due to the lack of knowledge about the controller [30]. Therefore, using model-free techniques can be a more suitable alternative for improved resiliency toward FDI attacks.

This chapter proposes a signal reconstruction method to make CSPM resilient to FDI attacks. The tracking error signals communicated in CSPM can be approximated as decaying exponentials with different amplitudes and settling times as the response of an IBR to a disturbance depends on its severity, type, and location. This enables the possibility of reconstructing remote tracking error signals using their autocorrelation and cross-correlation with local tracking error signals before passing them to CSPM. The proposed signal reconstruction method is implemented using semidefinite programming (SDP). SDP is a powerful optimization tool that is also resilient to noise. Finally, the reconstructed signals are filtered to further improve their quality. The performance of the proposed method is evaluated via time-domain simulation case studies on a microgrid modeled in PSCAD/EMTDC software in cosimulation with signal reconstruction running in Python. Simulation results confirm the validity of the proposed solution.

The specific contributions of this chapter are

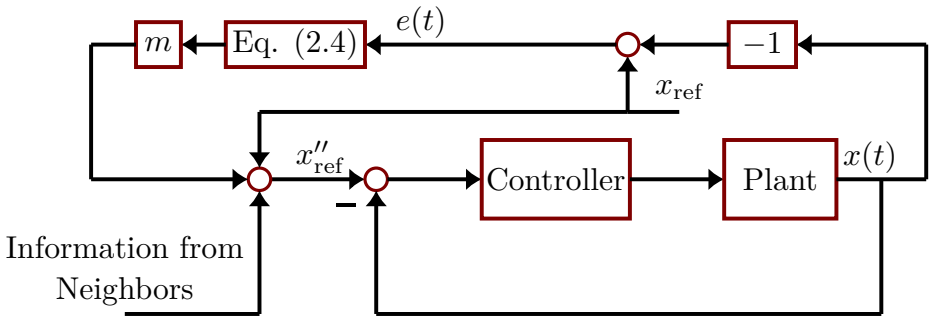

Figure 2.1: Block diagram representation of CSPM for a sample closed-loop control system.

- Design of a CSPM framework for a microgrid operating in grid-connected and islanded modes;
- Analytical assessment of CSPM under FDI attacks.
- Design of a resilient CSPM using signal reconstruction.

2.1 Proposed IBR Coordination Using CSPM

2.1.1 Basics of CSPM

Fig. 2.1 shows the generic block diagram representation of CSPM. CSPM modulates a particular set point x_{ref} in two stages. The first stage of CSPM is done using local measurements as

$$x'_{\text{ref}}(t) = x_{\text{ref}}(t) + me(t), \tag{2.1}$$

where x'_{ref} is the modulated set point, m is a design parameter, and $e(t)$ is the tracking error defined as

$$e(t) = x_{\text{ref}}(t) - x(t), \tag{2.2}$$

where x is the control variable. To further enhance CSPM performance, (2.2) is modified using the predicted tracking error as

$$x'_{\text{ref}}(t) = x_{\text{ref}}(t) + m\hat{e}_{\text{pred}}(t). \tag{2.3}$$

where $\hat{e}_{\text{pred}}$ is the predicted tracking error, defined as

$$\hat{e}_{\text{pred}}(t_0 + T_{\text{pred}}) = e(t_0) + r(t_0)T_{\text{pred}}, \tag{2.4}$$

where t_0 is the current time instant, T_{pred} is the prediction horizon, and $r(t_0)$ is the average rate of change calculated over the past measurements using the least squares method. The second stage of CSPM relies on communicating predicted tracking errors. Fig. 2.2 shows an example microgrid implementation of this concept. Communication is done using an undirected graph with N nodes and an adjacency matrix $A = [a_{ij}] \in R^{N\times N}$. The element a_{ij} determines a connection between nodes i and j on the communication graph. If $a_{ij} = 1$, then the two nodes communicate. If $a_{ij} = 0$, then the nodes do not communicate. Incorporating communication in (2.3) yields

$$x''_{\text{ref}}(t) = x'_{\text{ref}}(t) + \sum_{\substack{j=1 \\ j\neq i}}^{N} m_{ij}a_{ij}\hat{e}_{\text{pred},j}(t). \tag{2.5}$$

The second term in (2.5), which is depicted in Fig. 2.1 as "information from neighbors," brings situational awareness into CSPM. This term allows the nodes to achieve concensus on how to improve global system performance.

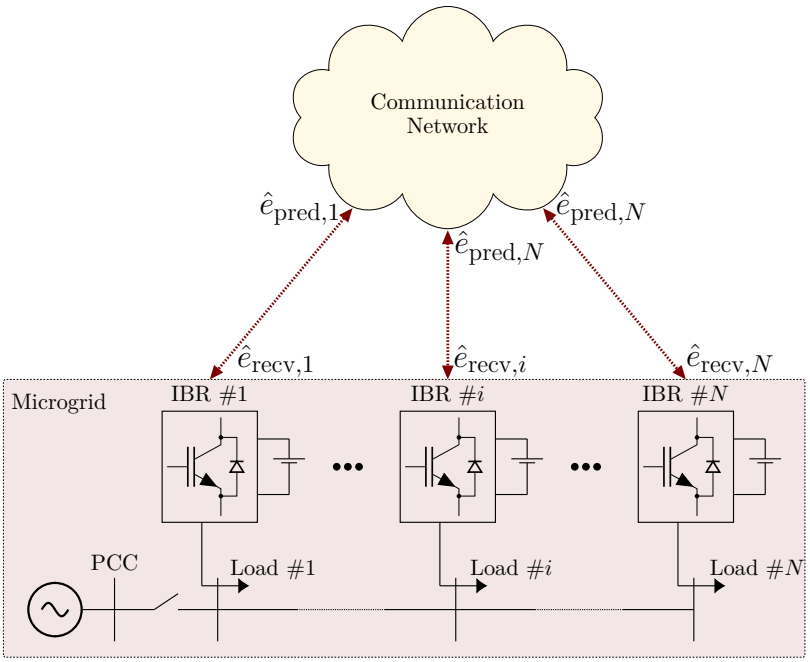

Figure 2.2: An example radial microgrid with N IBRs demonstrating the system-level implementation of CSPM.

2.1.2 Microgrid Control Using CSPM

Fig. 2.3 shows an IBR connected to the point of common coupling (PCC) through an LCL filter. Decoupled current control strategy, designed in the dq frame, is employed in this paper [5]. When the microgrid operates in the grid-connected mode, the IBRs operate in grid-following mode by synchronizing to the grid voltage and frequency to inject power. However, changes in grid topology, e.g., line outages, affect grid strength at the PCC. Grid strength is usually measured using short-circuit ratio (SCR) defined as

$$\text{SCR} = \frac{1}{\sqrt{R_{th}^2 + X_{th^2}}}, \tag{2.6}$$

where R_{th} and X_{th} are the Thevenin equivalent grid resistance and reactance at the PCC. A higher SCR translates into a stronger grid, while a lower SCR means

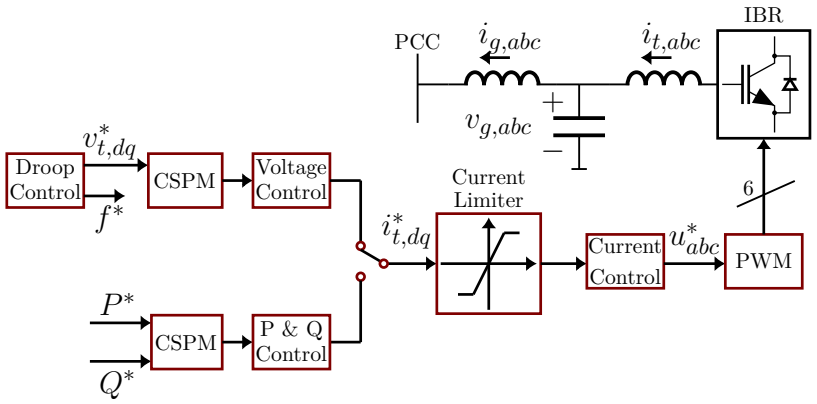

Figure 2.3: The proposed IBR control strategy using CSPM.

a weaker grid. A change in SCR affects IBR response. Therefore, the real and reactive power set points P^* and Q^* are modulated using CSPM, before being passed onto the power control unit that then generates the current set points $i^*_{t,dq}$.

In the islanded mode of operation, a number of IBRs need to operate in grid-forming mode, where they control voltage and frequency at their PCC. The other IBRs may operate in grid-forming or grid-following modes. In grid-forming mode of operation, the droop control unit first generates the voltage set points $v^*_{t,d}$ and $v^*_{t,q}$ using

$$v^*_{t,d} = 1 - m_v Q, \tag{2.7}$$

and

$$v^*_{t,q} = 0, \tag{2.8}$$

where m_v is the voltage droop coefficient. The droop control unit also generates

the frequency set point f^* using

$$f^* = 1 - m_f P, \tag{2.9}$$

where m_f is the frequency droop coefficient. In the islanded mode of operation, the microgrid is much smaller in size and has little to zero inertia. Moreover, it experiences frequent changes in generation and consumption as well as topological changes. Hence, $v^*_{t,d}$ is first modulated using CSPM and then passed to the voltage control unit. The voltage control unit then generates $i^*_{t,dq}$. Eventually, in both operating modes, $i^*_{t,dq}$ are passed through a limiter block to the current control block, and finally to the pulse-width modulation (PWM) block to control the switches. The PWM block needs a phase angle reference to generate the proper gating signals. This phase shift is usually generated using the internal clock of the IBR microcontroller. However, the internal clock uses a crystal oscillator that is nonideal and its accuracy drifts over time. Therefore, GPS communication can also be used to provide a precise timing solution to generating the phase reference for PWM [31], [32].

2.1.3 CSPM Operation Under FDI Attacks

During a successful FDI attack on CSPM, an attacker injects a malicious signal into the predicted tracking error of an IBR. The malicious predicted tracking error $\hat{e}^{\text{mal}}_{\text{pred}}(t)$ is found as

$$\hat{e}^{\text{mal}}_{\text{pred}}(t) = \hat{e}_{\text{pred}}(t) + \eta(t), \tag{2.10}$$

where $\eta(t)$ is the malicious injection. $\hat{e}^{\text{mal}}_{\text{pred},j}(t)$ is then communicated to the recipient IBR, where it enters its CSPM module and subsequently, its control system. Consider the basic scenario where an IBR is receiving a malicious predicted tracking error. Using (2.5), the corrupted modulated set point for the IBR $x''_{\text{ref,att}}(t)$ is found as

$$x''_{\text{ref,att}}(t) = x'_{\text{ref},i}(t) + m\hat{e}^{\text{mal}}_{\text{pred}}(t). \tag{2.11}$$

Equation (2.10) shows that injecting a malicious signal into a transmitted predicted tracking error corrupts the modulated set point for the recipient IBR. The impact of an FDI attack on CSPM depends on the magnitude of corruption in $x''_{\text{ref,att}}(t)$. If the amount of corruption is small, the FDI attack decreases the voltage and power quality of the IBR, which then propagates throughout the microgrid with different intensity. In case of more severe attacks, the recipient IBR can become unstable and trip. This causes a disturbance in microgrid voltage and frequency. If the disturbance is severe enough, the microgrid may experience a cascading failure, which may lead to its complete shut down. Hence, it is imperative that CSPM becomes resilient to FDI attacks to prevent such circumstances.

2.2 Overview of Signal Reconstruction Using Autocorrelation and Cross-Correlation

2.2.1 Autocorrelation and Cross-Correlation

Autocorrelation is a measure of similarity between a signal and itself. Cross-correlation is defined as a measure of similarity between two different signals. Consider the two signals x_1 and x_2 with lengths N_1 and N_2:

$$x_1 = (x_1[0], x_1[1], \ldots, x_1[N_1 - 1]), \tag{2.12}$$

and

$$x_2 = (x_2[0], x_2[1], \ldots, x_2[N_2 - 1]), \tag{2.13}$$

The autocorrelation vectors of the two signals are defined as

$$R_{11}[m] = \sum_{n=0}^{N_1-1} x_1[n] x_1^*[n-m], \tag{2.14}$$

and

$$R_{22}[m] = \sum_{n=0}^{N_2-1} x_2[n] x_2^*[n-m], \tag{2.15}$$

where R_{11} is the autocorrelation vector of x_1 and R_{22} is the autocorrelation vector of x_1. The cross-correlation vectors of x_1 and x_2 are defined as

$$R_{12}[m] = \sum_{n=0}^{N_1-1} x_1[n]x_2^*[n-m], \tag{2.16}$$

and

$$R_{21}[m] = \sum_{n=0}^{N_2-1} x_2[n]x_1^*[n-m], \tag{2.17}$$

where R_{12} is the cross-correlation between x_1 and x_2 and R_{21} is the cross-correlation between x_2 and x_1. In this section, the goal is to reconstruct x_1 and x_2 from R_{11}, R_{22}, R_{12}, and R_{21}.

2.2.2 Overview of the Classic Reconstruction Approach

Traditionally, signal reconstruction using autocorrelation and cross-correlation is performed by finding the common factors between their z-transforms. The z-transform polynomials of x_1, x_2, R_{11}, R_{22}, R_{12}, and R_{21} are related as

$$R_{11}(z) = X_1(z)X_1^*(z^{-*}), \tag{2.18}$$

$$R_{22}(z) = X_2(z)X_2^*(z^{-*}), \tag{2.19}$$

$$R_{12}(z) = X_1(z)X_2^*(z^{-*}), \tag{2.20}$$

and

$$R_{21}(z) = X_2(z)X_1^*(z^{-*}), \tag{2.21}$$

where z^{-*} is the inverse conjugate of z. Suppose that polynomials $z^{N_1-1}X_1(z)$ and $z^{N_2-1}X_2(z)$ are co-prime, i.e., they have no common roots. Then, $X_1(z)$ can be reconstructed via identifying the common factors between the polynomials $z^{N_1-1}R_{11}(z)$ and $z^{N_1-1}R_{12}(z)$. Analogously, $X_2(z)$ can be reconstructed via identifying the common factors between the polynomials $z^{N_2-1}R_{22}(z)$ and $z^{N_2-1}R_{21}(z)$. Reference [33] proves this concept using Sylvester matrices and shows that the co-prime condition is a necessary and sufficient criterion for the solving reconstruction problem.

2.2.3 Overview of the SDP-Based Reconstruction Approach

Autocorrelation and cross-correlation measurements are quadratic in nature. Therefore, signal reconstruction using autocorrelation and cross-correlation can be formulated as an optimization problem with quadratic constraints. The reconstruction problem is formulated and solved using SDP, as SDP shows robustness and theoretical guarantees [34], [35]. First, x_1 and x_2 are stacked in the vector $x = \left[\begin{smallmatrix} x_1 \\ x_2 \end{smallmatrix}\right]$. Then, x is embedded into a higher-dimensional space via $X = xx^*$. Finally, the signal reconstruction problem is defined as:

$$\begin{aligned} &\text{find} \quad X, \\ &\text{subject to} \;\; \operatorname{trace}(A_m X) = b_m \;\; \text{for} \;\; 0 \le m < M, \\ &\qquad\qquad X \succcurlyeq 0 \;\; \& \;\; \operatorname{rank}(X) = 1, \end{aligned} \tag{2.22}$$

where the A_m matrices are appropriate sensing matrices and b_m is an element in the autocorrelation and cross-correlation vector. To make the optimization problem convex, the rank constraint is relaxed and a rank-one approximation of X is found using singular value decomposition (SVD) instead. Additionally, the objective function of the problem is modified to make SDP more resilient to noise.

2.3 Proposed Resilient CSPM Strategy

2.3.1 Proof

Consider the single-phase LCL filter in Fig. 2.4. Using KVL and KCL, the state-space model is found as

$$\begin{cases} \dfrac{di_t}{dt} = \dfrac{1}{L_t}(v_t - v_c) \\ \dfrac{di_g}{dt} = \dfrac{1}{L_g}(v_c - v_g) \\ \dfrac{dv_c}{dt} = \dfrac{1}{C}(i_t - i_g) \end{cases}, \tag{2.23}$$

where L_t is the input inductance, C is the shunt capacitance, L_g is the output inductor, v_t is the input voltage, i_t is the input current, v_c is the capacitor voltage, i_g is the output current, and v_g is the output voltage. By applying the Laplace transform to (2.23) and simplifying, the transfer function relating the output current to the input voltage is found as

$$G(s) = \frac{I_g(s)}{V_t(s)} = \frac{1}{L_t L_g C s^3 + (L_t + L_g)s}, \tag{2.24}$$

The values for L_t, L_g, and C are in the milli and micro ranges. Therefore, their product results in a very small number. Therefore, the s^3 term in (2.23) can be

Algorithm 1 SDP-Based Signal Reconstruction Using Autocorrelation and Cross-Correlation

Inputs: Autocorrelation and Cross-correlation measurements concatenated in vector b with length M and signal lengths N_1 and N_2.

Outputs: Signal estimates $\hat{x}_1$ and $\hat{x}_2$.

- Solve the following to obtain the $(N_1 + N_2) \times (N_1 + N_2)$ estimated matrix $\hat{X}$

$$\begin{aligned} &\text{minimize} && \sum_{m=0}^{M-1} |\text{trace}(A_m X) - b_m|^2, \\ &\text{subject to} && X \succcurlyeq 0. \end{aligned} \tag{2.25}$$

- Calculate the best rank-one estimation of $\hat{X}$ and obtain $\hat{x}\hat{x}^*$.
- Return $\hat{x}_1$ and $\hat{x}_2$ from $\hat{x}$.

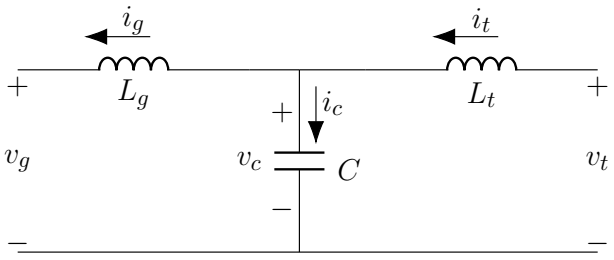

Figure 2.4: A single-phase LCL filter.

ignored and $G(s)$ can be simplified into a first-order transfer function as

$$G(s) = \frac{I_g(s)}{V_t(s)} = \frac{1}{(L_t + L_g)s}. \tag{2.26}$$

Considering a proportional integral (PI) controller, the complete open-loop transfer function is found as

$$G_{\text{OL}} = K_p(\frac{1 + sT_i}{sT_i})(\frac{1}{(L_t + L_g)s}), \tag{2.27}$$

where K_p is the proportional gain and T_i is the integrator time constant. The ultimate goal is to design K_p and T_i to optimize IBR response. This results in a

fast and smooth first-order response for the output current. Hence, the response for the output current to a step change in input voltage is found in time-domain as

$$i_g(t) = I_2 - (I_2 - I_1)e^{-t/\tau}, \tag{2.28}$$

where I_1 is the initial current, I_2 is the new current, and τ is a time constant related to the settling time of the response as $t_s \approx 5\tau$. The tracking error for $i_g(t)$ is found as

$$e_{i_g}(t) = (I_2 - I_1)e^{-t/\tau}, \tag{2.29}$$

where $e_{i_g}(t)$ is the tracking error. Equation (2.29) shows that the tracking error is a decaying exponential. Using this, let two generic tracking errors be $e_1[n] = A_1 e^{-a_1 n}$ and $e_2[n] = A_2 e^{-a_2 n}$. The z-transforms of these signals are found as

$$E_1(z) = \frac{A_1 z}{z - e^{-a_1}}, \tag{2.30}$$

and

$$E_2(z) = \frac{A_2 z}{z - e^{-a_2}}, \tag{2.31}$$

where $E_1(z)$ is the z-transform of e_1 and $E_2(z)$ is the z-transform of e_2. Multiplying (2.30) by z^{N_1-1} and (2.31) by z^{N_2-1} yields

$$z^{N_1-1}E_1(z) = \frac{A_1 z^{N_1}}{z - e^{-a_1}}, \tag{2.32}$$

and

$$z^{N_2-1}E_2(z) = \frac{A_2 z^{N_2}}{z - e^{-a_2}}. \tag{2.33}$$

While the response of all IBR controllers are optimized in practice, the settling time of an error signal depends on the location of a disturbance within a microgrid, i.e., $a_1 \neq a_2$ for $e_1[n]$ and $e_2[n]$. Hence, the polynomials in (2.32) and (2.33) are co-prime and e_1 and e_2 can be reconstructed using their autocorrelation and cross-correlation measurements.

2.3.2 Proposed Resilient CSPM

Fig. 2.5 shows the proposed resilient CSPM strategy. The proposed signal reconstruction strategy is added to the IBR control system as an additional module. The tracking errors received from remote IBRs are passed into the proposed signal reconstruction module along with local tracking errors. In the grid-forming mode of operation, tracking errors are of voltage type, while in the grid-following mode, tracking errors of power type. The remote tracking errors are then reconstructed using the SDP as described in Algorithm 1. The reconstructed tracking errors are then passed to the corresponding CSPM module according to the mode of operation. The reconstruction of tracking errors makes CSPM more resilient to FDI attacks by reducing the amount of bad injection. This maintains the advantages of CSPM and prevents the microgrid from becoming unstable.

2.3.3 Computational Efficiency

The computational burden of the proposed reconstruction algorithm is mainly related to the size of the autocorrelation and cross-correlation vector and the run-

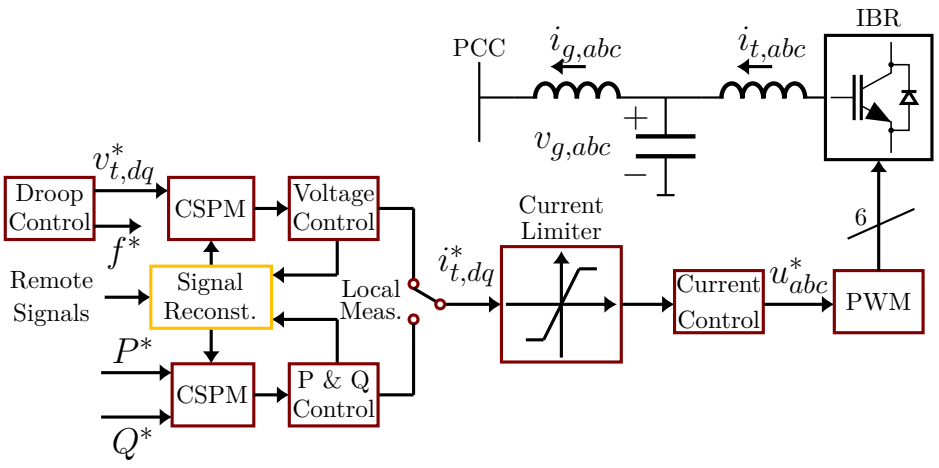

Figure 2.5: Resilient IBR control using CSPM including the proposed signal reconstruction module.

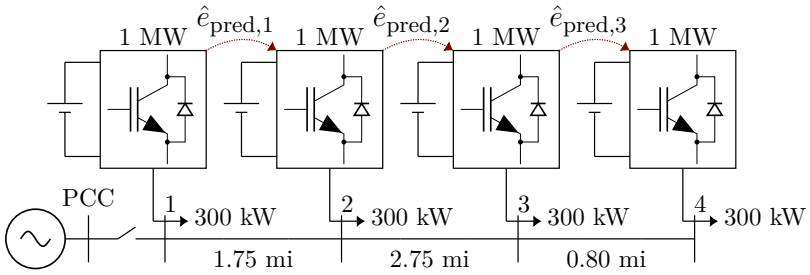

Figure 2.6: Employed study system.

ning time of the employed SDP solver. The computational burden of calculating autocorrelation and cross-correlation can be minimized by achieving tradeoff between the sampling rate and size. This also reduces the input data size for SDP. Even though faster algorithms are proposed to solve SDP problems [36], [37], an SDP optimization algorithm can also run faster by enabling the proper settings such as warm start and acceleration.

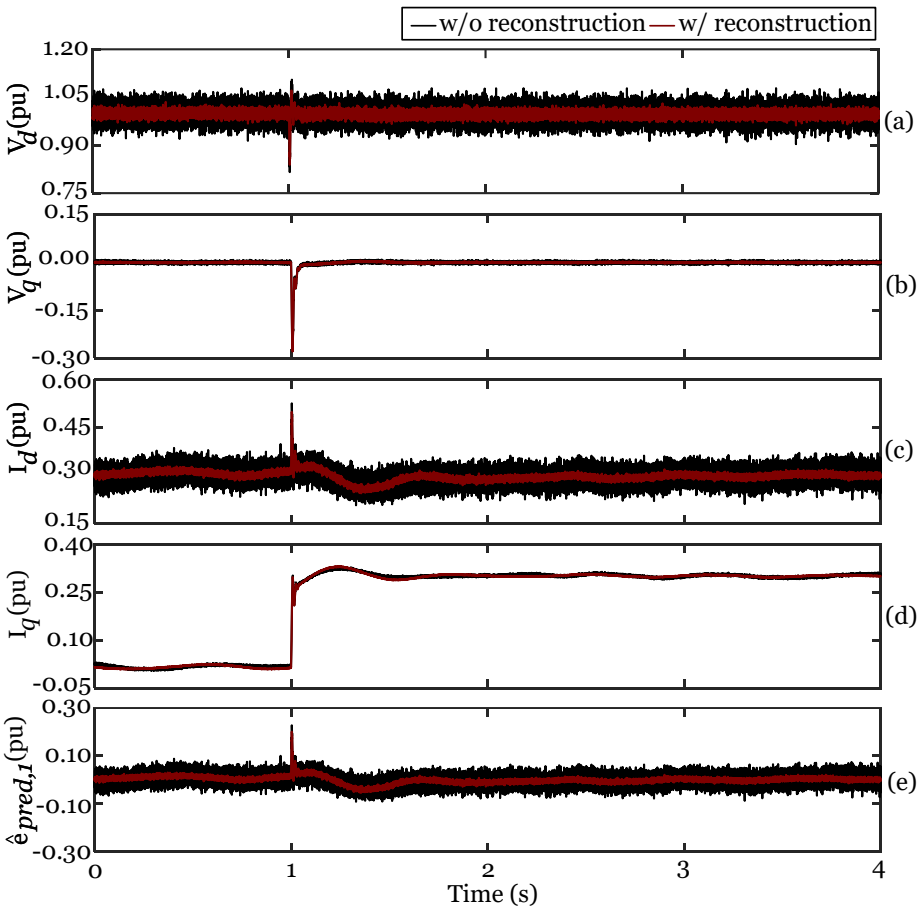

Figure 2.7: Simulation results for IBR2 under Case 1.

2.4 Performance Evaluation

Fig. 2.6 shows the study system modeled using PSCAD/EMTDC software to evaluate the performance of the proposed method. The study system is a radial microgrid with 4 IBRs, each rated at 1 MW and 12.47 kV. The droop constants of each IBR is also set to 1%. The breaker at the PCC controls the mode of operation for the microgrid. Each IBR also supplies a 300 kW load with a lagging power factor of 0.95 at its bus. The IBRs are interconnected using three short lines. Each IBR communicates its error signal with its adjacent IBR. In this

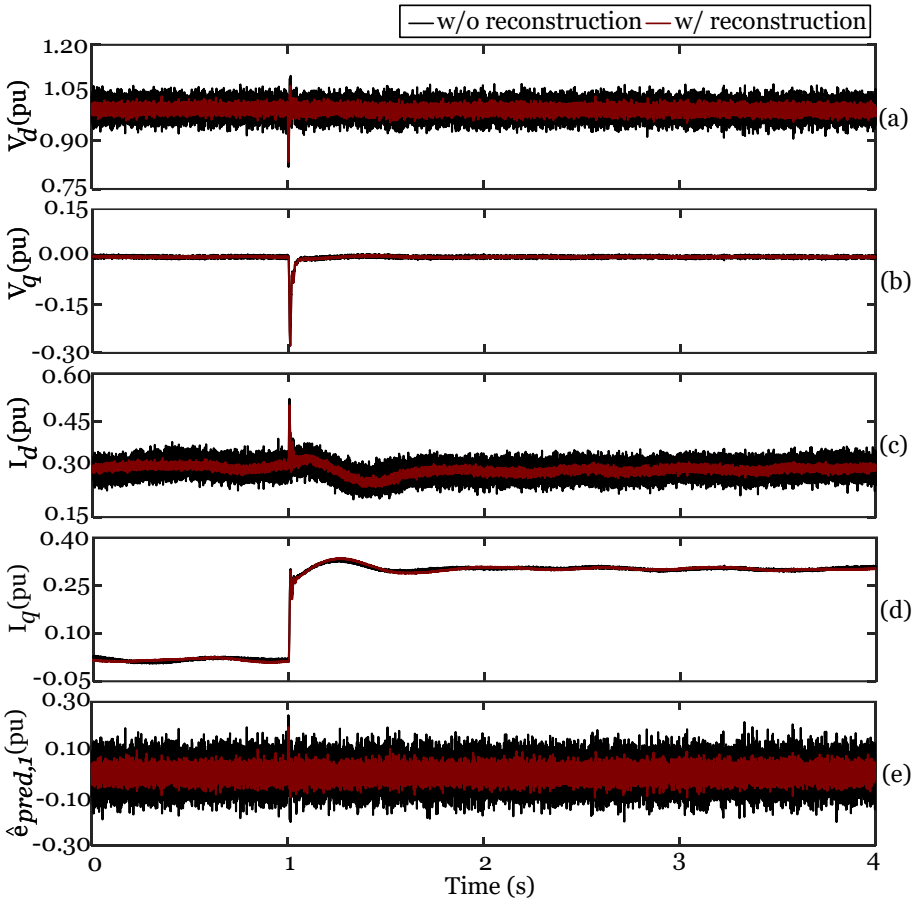

Figure 2.8: Simulation results for IBR2 under Case 2.

work, it is assumed that the attacker has limited information about the microgrid control design and operation. Hence, and additive white Gaussian noise (AWGN) is considered as the bad injection during an FDI attack. The proposed signal reconstruction strategy is implemented using the CVXPY library in Python. The employed sampling rate is 10 μs and reconstruction is performed every 100 μs. The cutoff frequency of the LPF is 10 kHz. Finally, the cosimulation API of PSCAD/EMTDC is used to link the signal reconstruction program in Python with PSCAD/EMTDC and evaluate the performance of the proposed strategy under various time-domain simulation case studies.

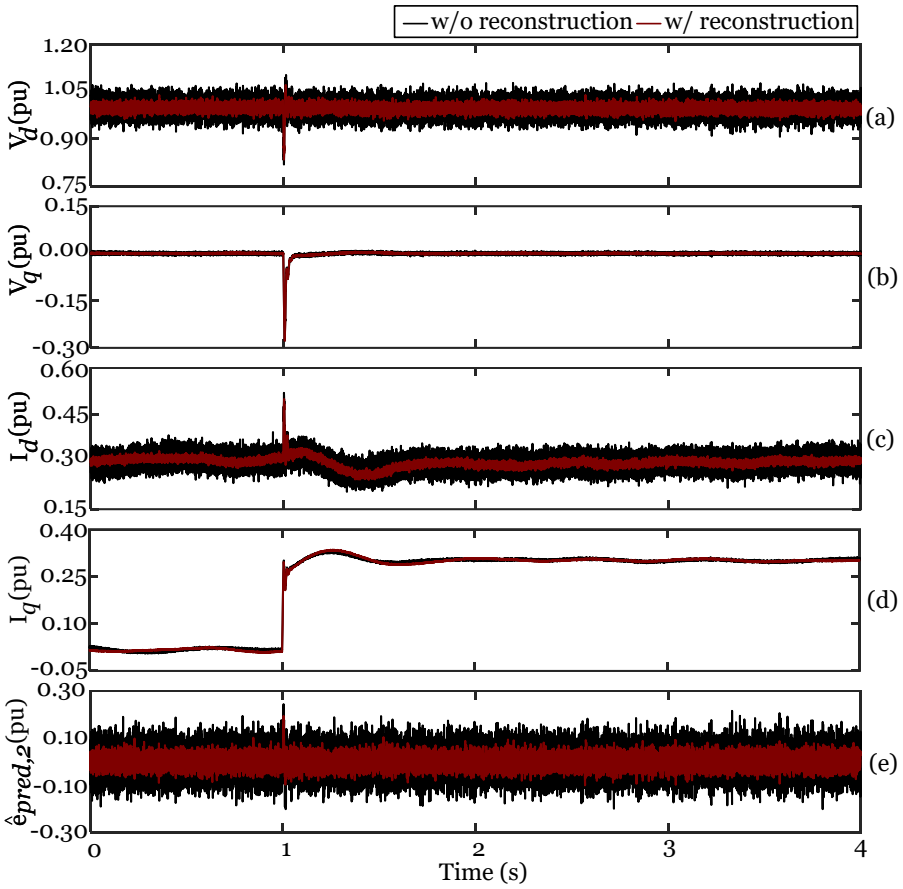

Figure 2.9: Simulation results for IBR3 under Case 2.

2.4.1 Case 1: Corruption in One Tracking Error

Fig. 2.7 shows the simulation results for Case 1. In this case study, the tracking error transmitted by IBR1 $\hat{e}_{\text{pred},1}$ is hijacked by an adversary and corrupted by injecting an AWGN with a standard deviation of $\sigma = 0.5$. Simulation results clearly demonstrate that the proposed signal reconstruction strategy is able to significantly reduce the amount of noise in the other IBR measurements. To test the microgrid performance under sever contingencies, a large reactive load of 1 MVAr is energized at bus 2 at $t = 1$ s. Energization of a large reactive load has a significant impact on voltage and is a potential disturbance for a microgrid.

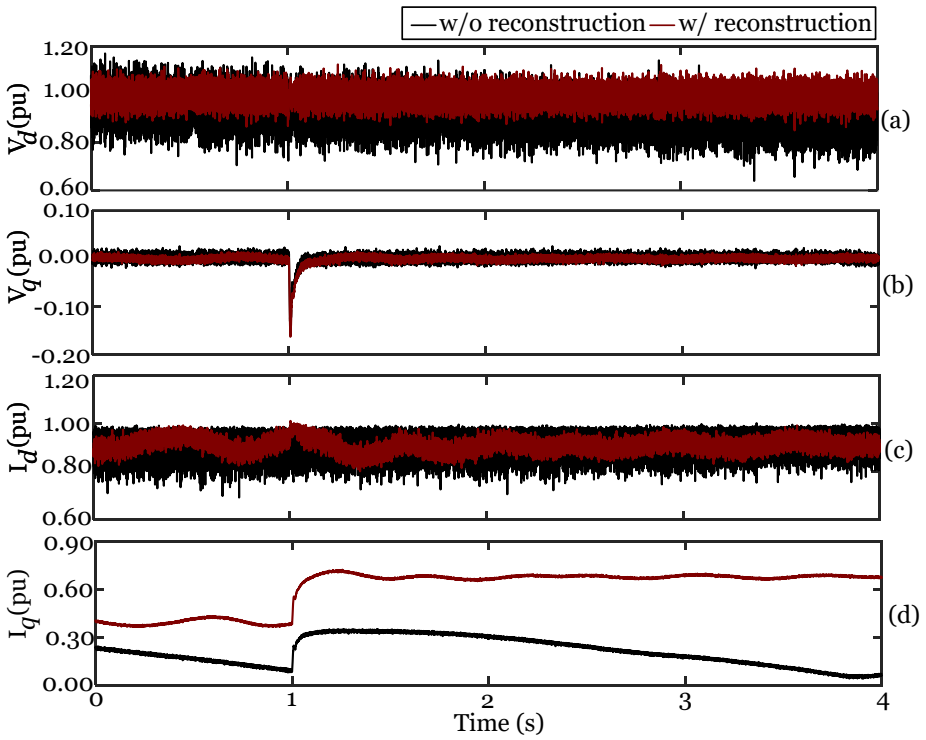

Figure 2.10: Simulation results for IBR2 under Case 2.

Once again, the simulation results depict that the proposed signal reconstruction method is able to perform better by reducing the undershoot in the d-axis voltage V_d and the d-axis current I_d.

2.4.2 Case 2: Corruption in Multiple Tracking Errors

Figs. 2.8 and 2.9 show the simulation results for IBRs 2 and 3 for Case 2. In this case study, it is assumed that an attacker is injecting n AWGN with a standard deviation of $\sigma = 0.5$ into the communicated tracking errors $\hat{e}_{\text{pred},1}$ and $\hat{e}_{\text{pred},2}$. The simulation results indicate that the proposed signal reconstruction method is able to maintain a much lowered amount of noise in IBR measurements. Moreover, it is also able to reduce the overshoot in I_d and the undershoot in V_d after a large reactive load of 1 MVAr is energized at bus 2 at $t = 1$ s.

2.4.3 Case 3: Impact of Noise Power

Fig. 2.10 shows the simulation results for Case 3. In this case study, the tracking error transmitted by IBR1 $\hat{e}_{\text{pred},1}$ is corrupted by injecting a powerful AWGN with a standard deviation of $\sigma = 2$. Moreover, all IBRs are operating near their limits with all loads consuming 900 kW. Simulation results show that the proposed signal reconstruction strategy significantly improves the quality of $\hat{e}_{\text{pred},1}$ and all other measurements. Once again, a large reactive load of 1 MVAr is energized at bus 2 at $t = 1$ s to evaluate the dynamic performance of the proposed method. Simulation results indicate that the proposed signal reconstruction method is able to prevent the microgrid from becoming unstable.

Chapter 3

Protection of Microgrids Against System Faults

3.1 Introduction

A microgrid should be properly protected from faults within its boundaries to ensure its stable operation is maintained. However, microgrid protection is challenging. The maximum fault current contribution of an IBR is usually limited to 120%–150% of its rated current [20]. Therefore, fault current magnitude is significantly different in grid-connected and islanded modes of operation. Consequently, it is difficult or even impossible for traditional protection devices such as fuses, reclosers, and overcurrent relays to detect faults in the islanded mode of operation [15]. The unconventional response of IBRs to faults also corrupts phasor estimation in digital relays, causing recurring false trips [39]. Distance protection is not a viable option because of small measured impedance due to short lines and corrupted phasor estimations [15]. While differential relaying can overcome these problems, it requires a high-bandwidth communication system.

Portions of this chapter are submitted as

[38] A. Mohammadhassani and A. Mehrizi-Sani, "Nonpilot directional protection of a microgrid," IET Gener. Transm. Distrib., Apr. 2023, under review.

Therefore, installing differential relays on every line can be uneconomical. Moreover, a differential relay cannot operate on lines with multiple branches. The operation of a differential relay is significantly impacted by current transformer (CT) mismatches [15], [40]. Traveling wave–based protection is also proposed for microgrids [41]–[43]. This method is immune to fault current variations; however, its performance is not evaluated on short lines and it requires instrument transformers with bandwidths in the MHz range.

Utilizing IBR control for microgrid protection is proposed in [44]–[48]. Reference [45] proposes a control loop for an IBR that enables it to inject 5th harmonic current during a fault to improve the performance of overcurrent relays in the distribution system. However, overcurrent relays are difficult to coordinate in islanded microgrids. Reference [46] proposes a differential protection scheme that compares off-nominal frequency current measurements by two relays protecting line. However, this scheme requires communication. Reference [47] proposes a control loop for an IBR to inject low-order harmonic currents and designs a directional element that measures harmonic currents to implement protection coordination. However, using cosine similarity (CS) reduces the reliability of this method and requires communication.

Utilizing artificial intelligence for microgrid protection is proposed in [49]–[51]. Intelligent sequence current-based differential protection methods are proposed in [49], [50]. However, they require communication and are not suitable for microgrids due to their small and unconventional sequence currents [52]. Reference [51] uses a wavelet-based deep neural network-based method for protection of microgrids. However, it uses fault current magnitude to train the neural network, which makes it unsuitable for islanded microgrids. The benefits of using SVM

for protection of microgrids are explored in [53]–[55]. An SVM-based directional element is proposed in [53] for islanded microgrids. However, its performance is only explored for three-phase-to-ground faults. An SVM-based overcurrent protection scheme is proposed for distribution systems with renewable resources in [54]. However, this relies on fault current magnitude to train SVMs, which significantly reduces its operating speed. A protection scheme using SVM and Gaussian processes is proposed for microgrids in [55]. However, it is focused on systems with synchronous generation.

Building on the method in [47], this chapter proposes a nonpilot, i.e., without using a dedicated communication system, directional protection scheme for an islanded microgrid using SVM to recognize and interpret the harmonic current measurement for each relay. The measured harmonic currents have a different arrangement but similar magnitudes under forward and reverse faults. A forward fault occurs in front of a relay, while a reverse fault occurs behind a relay. Moreover, a forward fault at different locations along the protected line results in harmonic current measurements with similar arrangement but different magnitudes. Hence, measured harmonic currents can be used as training data for SVM to detect fault current directionality and relay zone of operation. Therefore, the proposed method does not require a feature extraction method. Utilizing this, the proposed method offers a fast and robust relay coordination scheme. The performance of the proposed method is evaluated in PSCAD/EMTDC software via transient simulation of different contingency scenarios.

The specific contributions of this chapter are

- An SVM-based directional element.
- An SVM-based zone detection element.

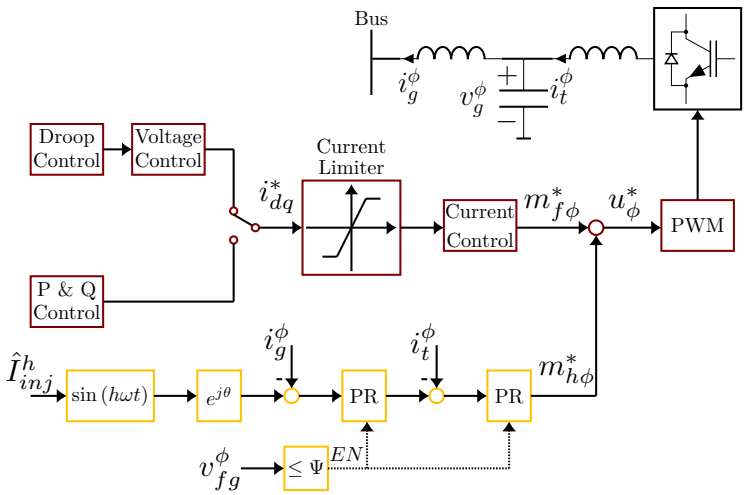

Figure 3.1: Block diagram demonstration of the IBR controller proposed in [32].

- A robust nonpilot directional relay coordination scheme.

3.2 Overview of Microgrid Protection Using Harmonic Current Injection

3.2.1 Overview of the Harmonic Current Injection Strategy

Fig. 3.1 shows the per-phase IBR control system designed in [47]. This controller has two main loops, one for normal operation of the IBR and one for during faults. The control loop for normal operation of the IBR samples the grid current i_g^ϕ, extracts its dq components i_g^{dq}, and feeds them to the current controller. The reference dq components of i_g^ϕ are generated by the real power P and reactive power Q controllers during grid-connected operation and the droop controllers during islanded mode of operation. Finally, the current controller generates the reference modulation index $m_{f\phi}^*$.

The IBR enters the low-voltage ride-through (LVRT) mode of operation when the voltage on any phase is less than 0.88 pu, according to the IEEE standard 1547-2018 [56]. The control loop for harmonic current injection takes advantage of this mode and adds a modified modulation index $m^*_{h\phi}$ to $m^*_{f\phi}$ so that the IBR injects three harmonic currents only during the LVRT mode as

$$i^h_{\text{inj}} = \hat{I}^h_{\text{inj}} \sin\left(h\omega_o t + \theta\right), \;\; h = 3, 5, 7, \tag{3.1}$$

where $\hat{I}^h_{\text{inj}}$ is the magnitude of the hth harmonic current, ω_o is the fundamental angular frequency, and θ is the phase shift of each harmonic. The reason the 3rd, 5th, and 7th harmonics are chosen is that using higher harmonic orders increases the switching frequency of the IBR and requires a high-bandwidth controller. Additionally, the order of the injected harmonic currents should be less than 10 to prevent overlapping with the resonant frequency of the LCL filter. Finally, The 2nd and 6th harmonics are dominant during unbalanced transients. The harmonic currents utilize a phase shift of θ rather than $h\theta$ to convert them from zero- and negative-sequence currents to positive-sequence ones. This enables the harmonic current injection controller to inject triplen and low-order harmonics. It should be noted that the injection of 3rd and 5th harmonics may falsely block the differential protection scheme of the IBR transformer. However, this can be easily solved by carefully designing this particular setting for the transformer differential relay [57].

To prevent overloading an IBR, the active IBR current $i_{t,d}$ is limited to its maximum $i^{\max}_{t,d} = +\beta I_{\text{nom}}$ and its minimum $i^{\min}_{t,d} = -\beta I_{\text{nom}}$, where I_{nom} is the rated current of the IBR and β is typically set to a value between 1 and 1.5. The reactive current $i_{t,q}$ is limited such that priority is given to the active current.

Therefore, the reactive current is limited to $\pm\sqrt{(i_{t,d}^{\max})^2 - (i_{t,d}^{*})^2}$. Using this, the maximum total rms fault current contribution of an IBR is αI_{nom}. A margin should be set between α and β to account for the IBR injecting all three harmonic currents. Hence,

$$(\alpha I_{\text{nom}})^2 = (\beta I_{\text{nom}})^2 + 3(\hat{I}_{\text{inj}}^{h})^2. \tag{3.2}$$

In this paper, $\alpha = 1.2$ and $\beta = 1$ to limit the maximum total fault current of an IBR to 120% of its I_{nom}. Consequently,

$$\hat{I}_{\text{inj}}^{h} = \sqrt{\frac{\alpha^2 - \beta^2}{3}} I_{\text{nom}} = 0.38 I_{\text{nom}}. \tag{3.3}$$

The control loop for injecting the harmonic currents is designed in the *abc* frame. Two proportional-resonant controllers (PR) are used to regulate i_g^{ϕ} and i_t^{ϕ}. These PR controllers have the following transfer function

$$F(s) = K_p + \frac{K_r s}{s^2 + \omega_r^2}, \tag{3.4}$$

where K_p is the proportional gain, K_r is the resonant gain, and ω_r is the resonant frequency which is set to the frequency of the injected harmonic current.

3.2.2 Overview of the Directionality Element

Fig. 3.2 shows an overview of the directionality element in [47]. Three-phase currents are measured at each relay station and their positive-sequence components are extracted and fed to the fast Fourier transform (FFT) block to extract the harmonic currents. A microgrid may include nonlinear loads that inject harmonic currents. However, nonlinear loads must comply with the IEEE standard

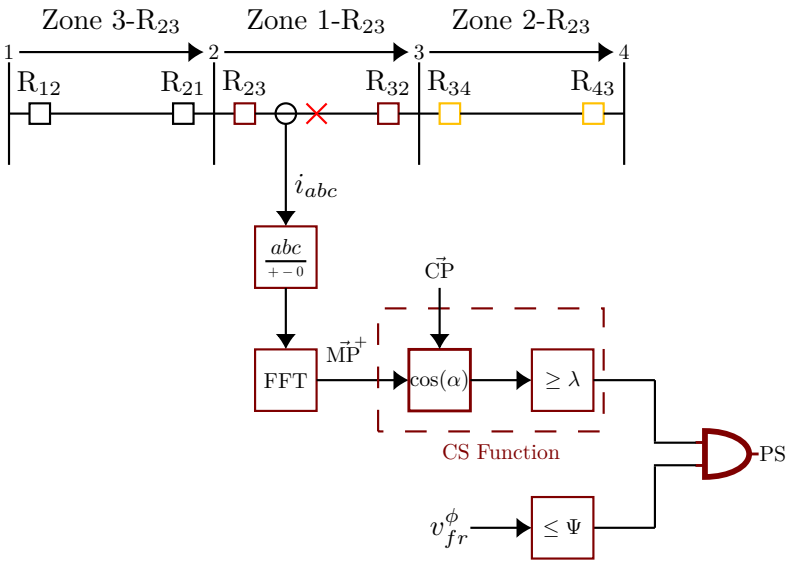

Figure 3.2: Overview of the directional element logic proposed in [32].

519 which strictly limits their voltage and current distortion. Additionally, the largest harmonic harmonic current injected by such loads is typically the 3rd harmonic, which is a zero-sequence harmonic component. This harmonic is filtered out by the relay, as it measures only positive-sequence harmonic currents. Hence, the impact of nonlinear loads on the performance of the directionality scheme is negligible. The measured pattern (MP) is then compared with the characteristic pattern (CP) of the relay using CS to determine fault current directionality:

$$\cos(\alpha) = \frac{\langle \vec{\mathrm{MP}}, \vec{\mathrm{CP}} \rangle}{\|\vec{\mathrm{MP}}\| \, \|\vec{\mathrm{CP}}\|}, \tag{3.5}$$

where $\langle \cdot, \cdot \rangle$ denotes inner product, $\| \cdot \|$ is the norm function, and α is the angle between the two vectors. If MP and CP align, or $\cos(\alpha) = 1$, the fault current is in forward direction. Otherwise, the fault current is in reverse direction. However, the diversity of IBR ratings and locations forces the use of a threshold $\lambda = 0.85$ in CS, which makes it less reliable.

3.2.3 Overview of the Directional Relay Coordination

The reliability issue of CS can be addressed by using communication between the relays. The permissive overreaching transfer trip (POTT) is used in [47] to implement a pilot directional coordination scheme. In this technique, the two relays on each line exchange their POTT signals through a communication channel. In Fig. 3.2, consider a fault in zone 1 of R_{23}. A forward fault is flagged and R_{23}'s POTT operates if both R_{23} and R_{32} detect forward direction. Otherwise, a reverse fault is flagged. For a fault in zone 2 of R_{23}, the POTT signal received from relay R_{34} blocks the operation of R_{23} for a coordination time interval (CTI) of 10 cycles as defined in [56]. If relay R_{34} does not operate in its designed CTI, R_{23} operates. The protection scheme in [47] de-energizes the microgrid if the fault is not cleared in 15 cycles.

3.3 Proposed SVM-Based Protection Scheme

3.3.1 Motivation

Reference [47] shows that harmonic currents can be used as reliable inputs for microgrid protection. However, the reliability issue of CS in tandem with the need for communication necessitates an improved protection scheme. This paper proposes a protection scheme that uses SVM to coordinate the relays by recognizing patterns in the measured harmonic currents. This eliminates the need for threshold calculation in CP and the need for communication in POTT. Hence, the proposed method offers better robustness and reliability.

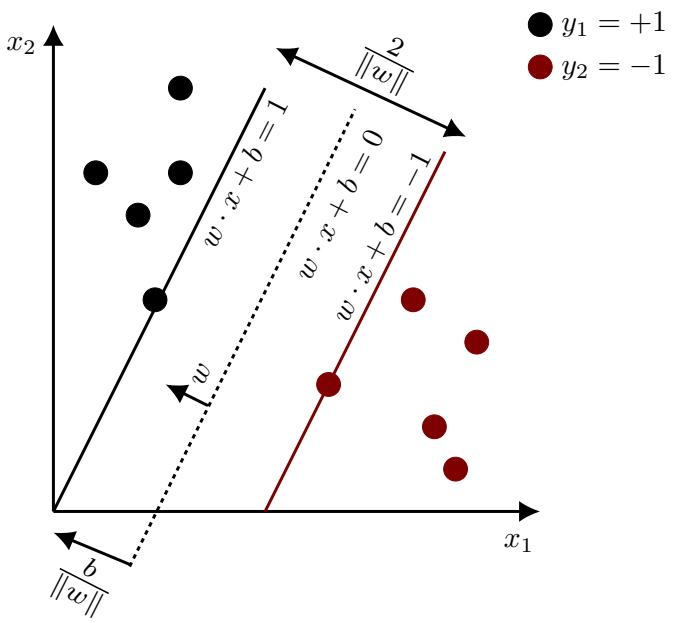

Figure 3.3: Sample linear training dataset.

3.3.2 Overview of Classification Using SVM

An SVM trains a classification algorithm to separate a two-class dataset [58]. Consider an input dataset $X_{m\times n}$, where n is the number of input features and m is the number of feature samples. Each feature sample x_i is associated with a class label of $y_i = \pm 1$. Therefore, an output dataset of $Y_{m\times 1}$ can be constructed by stacking the class labels. Finally, a training dataset is constructed as $T_{m\times(n+1)} = [X, Y]$. If T is linearly separable, SVM separates the data points by finding a hyperplane $f(x)$ in the n-dimensional space that satisfies

$$f(x) = w \cdot x + b = \sum_{j=1}^{n} w_j x_j + b = 0, \tag{3.6}$$

where w is the n-dimensional vector normal to the hyperplane and b is an offset value. A positive $f(x)$ indicates a class label of $+1$ and a negative $f(x)$ indicates a class label of -1. To optimally separate the classes, SVM finds the hyperplane

with maximum distance from the nearest data points of each class, i.e., support vectors (SV). This hyperplane is called the optimal or the maximum-margin hyperplane. As an example, consider the two-dimensional training dataset shown in Fig. 3.3. Two parallel lines with the largest distance between them can be selected to optimally separate the data points. These two lines are defined as

$$\langle w, x \rangle + b = 1, \tag{3.7}$$

and

$$\langle w, x \rangle + b = -1, \tag{3.8}$$

where any data point falling above (3.7) has a class label of $+1$ and any data point falling below (3.8) has a class label of -1. The region between the two lines is called the margin and the maximum-margin line lies halfway between them. The geometric distance between the two parallel lines is $\frac{2}{\|w\|}$ and the parameter $\frac{b}{\|w\|}$ determines the offset of the optimal line with respect to the origin along w. Hence, the margin between the two parallel lines is maximized by minimizing $\|w\|$:

$$\begin{aligned} &\min_{w,b} \ \frac{1}{2}\|w\|^2 \\ &\text{subject to } y_i(w^T x_i - b) \geq 1, \ \ i = 1, 2, \ldots, m. \end{aligned} \tag{3.9}$$

By accounting for noise in T, equation (3.9) becomes

$$\begin{aligned} &\min_{w,b} \ \frac{1}{2}\|w\|^2 + C\sum_{i=1}^{m}\zeta_i \\ &\text{subject to } \ y_i(w^T x_i - b) \geq 1 - \zeta_i, \ \ i = 1, 2, \ldots, m \\ &\qquad\qquad \zeta_i \geq 0, \ \ \forall i. \end{aligned} \tag{3.10}$$

where ζ_i is the slack variable measuring the distance between margin and the data points on the wrong side of the margin, and C is the penalty factor that achieves tradeoff between margin maximization and misclassification. Finally, the score function is defined as

$$f(x) = \sum_{i=1}^{N_{\text{SV}}} \alpha_i y_i x_i^T x + b, \tag{3.11}$$

where N_{SV} is the total number of SVs and α_i is a Lagrangian multiplier.

SVM uses the kernel trick to perform classification for a nonlinear dataset. A kernel is a mathematical function that maps the training dataset into a higher-dimensional feature space to enable linear classification. This function is defined as $K(x, y) = \phi(x)^T \phi(y)$, where $\phi(x)$ is a nonlinear vector function. Using this, the linear decision function is written as

$$f(x) = \sum_{i=1}^{N_{\text{SV}}} \alpha_i y_i K(x_i, x). \tag{3.12}$$

The most common kernel functions are: the linear kernel $K(x_i, x_j) = x_i^T x_j$, the polynomial kernel $K(x_i, x_j) = (\gamma(x_i \cdot x_j) + r)^d$ with $\gamma > 0$, and the Gaussian kernel $K(x_i, x_j) = \exp(-\gamma||x_i - x_j||^2)$, where $\gamma > 0$. The Gaussian kernel is used in this paper due to its superior ability for separating nonlinear datasets [55].

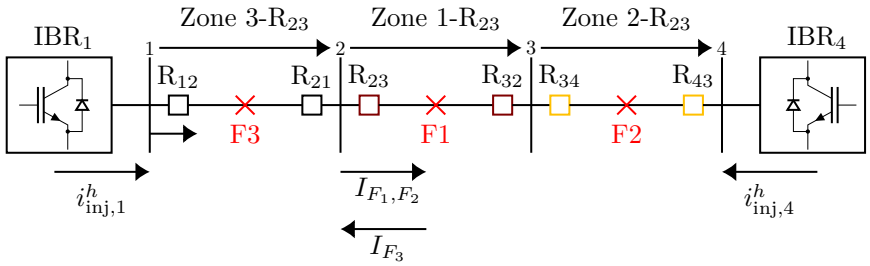

Figure 3.4: Proposed SVM-based directional relaying scheme.

3.3.3 Problem Formulation

Microgrid protection can be formulated as two binary classification problems: (a) directionality and (b) zone detection. Directionality refers to the problem of differentiating between forward and reverse faults. Zone detection is concerned with finding the location of the fault. Optimal coordination of the relays can be achieved by simultaneously solving these two problems in an efficient manner. Based on the scheme in [47], the IBRs start injecting harmonic currents as soon as the voltage drops due to a fault. Consider relay R_{23} in Fig. 3.4. For a forward fault at location F1, the relay measures the current I_{F_1}, which includes of the harmonic pattern $i^h_{\text{inj},1}$. However, for a reverse fault at location F3, the relay measures the current I_{F_3}, which includes the harmonic pattern $i^h_{\text{inj},4}$. Given that the two IBRs inject different harmonic patterns, relay R_{23} measures a different harmonic pattern orientation under forward and reverse faults. This results in a linearly separable training dataset for SVM to solve the directionality problem. Once again, take relay R_{23} as an example. For a forward fault at location F1, this relay measures the current I_{F_1}, which includes the harmonic pattern $i^h_{\text{inj},1}$. The relay also measures $i^h_{\text{inj},1}$ under a forward fault at location F2. However, IBR$_1$ experiences a smaller voltage reduction in this case and a part of its output power is consumed by the load at bus 1. Hence, relay R_{23} measures a harmonic pattern with the same orientation as for a fault in F1 but with a smaller magnitude.

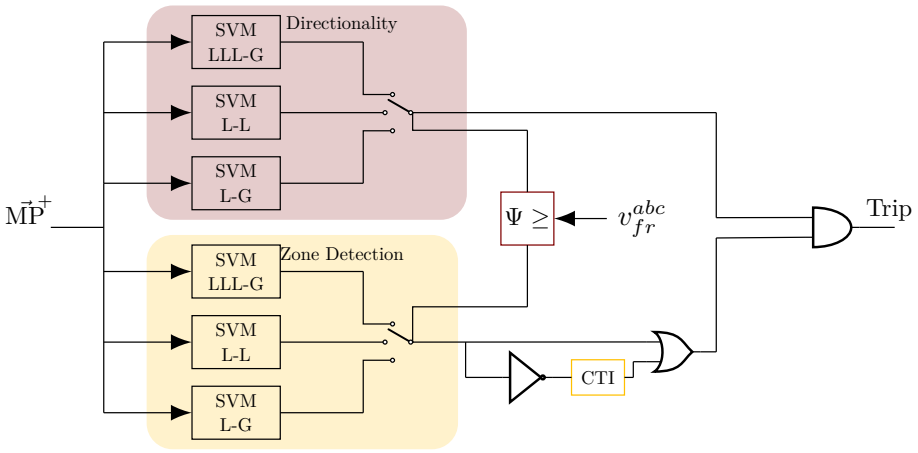

Figure 3.5: Proposed SVM-based directional relaying scheme.

Therefore, a dataset consisting of harmonic patterns measured under forward faults occurring along zones 1 and 2 of a relay can be used to train an SVM model for zone detection. However, the training dataset is no longer linear. Therefore, a Gaussian kernel is trained to separate the data points.

3.3.4 Proposed SVM-Based Directional Relaying

Fig. 3.5 shows the proposed SVM-based directional relaying scheme. There are three main types of faults in a power system: three-phase-to-ground, line-to-line, and line-to-ground. Therefore, three SVMs are chosen as directional elements, each for one type of fault. Similarly, three SVMs are selected as zone detection elements. A fault is flagged on a phase as soon as the relay senses its voltage is below 0.88 pu. This setting may mislead a relay into confusing an inrush current with a fault. However, an inrush current typically dies out quickly. Since it takes 3 fundamental cycles for FFT to extract the harmonic currents, the performance of the proposed scheme remains unaffected under an inrush current. The performance of the proposed scheme also remains untouched under an overloading scenario as the measured harmonic pattern is completely different than that under a fault. Depending on the type of fault flagged by the relay, the

corresponding directional SVM operates using the orientation of the recorded MP. If a forward fault is detected, a high output is flagged by the directional SVM. Otherwise, a low signal is issued and relay operation is blocked. The corresponding zone detection SVM also uses the recorded MP to detect the operating zone of the relay. A high signal is flagged if the fault is in the primary zone of the relay. A low signal is generated for an out-of-zone fault. In this case, the relay acts as a backup for the forward-seeing relay on the adjacent line and waits for a CTI of 10 cycles as set in [56]. If the fault is not cleared by then, the backup relay operates and de-energizes the line. In case the fault is not cleared in 15 cycles, all IBRs trip and the microgrid becomes de-energized.

3.3.5 Acquisition of Training Data

Fig. 3.6 shows the CIGRE MV North American distribution benchmark system [59]. This system is modeled in PSCAD/EMTDC software as the study system in this paper to implement and evaluate the proposed protection scheme. The top breakers in Fig. 3.6 are opened to establish islanded mode of operation. The bottom three breakers are closed to form a meshed topology. Two relays are placed on each line. Therefore, this system has 30 relays. The study system also included 14 IBRs, each connected to one bus through a Yg–Yg step-up transformer. The IBRs in the study system can operate in either the grid-following or grid-forming mode of operation. However, the injection of harmonics can be done in both modes. Moreover, the relays use harmonic currents as polarizing quantities. Hence, the proposed method is agnostic to IBR fault response. An optimization problem is solved in [47] to minimize the harmonic injection across all IBRs subject to relay detection and coordination. Table 3.1 summarizes the results of this optimization for the employed study system. For contingencies

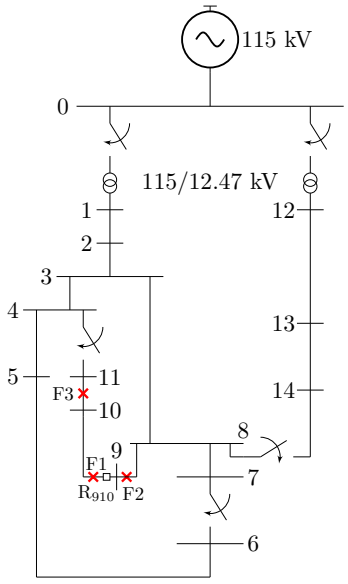

Figure 3.6: Employed study system: an IBR is connected to all buses 1–14.

Table 3.1: Optimal Injection Patterns for the Employed Study System

Bus	Rating (MVA)	Injection Pattern			Bus	Rating (MVA)	Injection Pattern		
		I3	I5	I7			I3	I5	I7
1	6.0	1	0	0	8	0.5	0	0	0
2	0.5	0	0	0	9	0.5	0	1	0
3	1.0	0	0	0	10	1.0	0	0	0
4	0.5	1	0	0	11	0.5	0	0	1
5	1.0	0	0	0	12	6.0	0	1	0
6	0.5	0	0	0	13	0.5	0	0	0
7	2.0	0	0	1	14	1.0	0	0	0

such as IBR outages and line outages, the optimization is repeated to update the injection patterns in Table 3.1 so that the relays measure the same harmonic current pattern as before. Therefore, the performance of the proposed method remains unaffected under such scenarios. In case of topology changes, the optimization may not result in relays measuring the same harmonics as before. Therefore, the SVMs must be retrained on the new patterns to protect the microgrid.

Forward and reverse ABC-G faults are applied at each relay station to obtain input data for training their LLL-G directionality SVMs. The MPs recorded by

the relays, consisting of harmonic current magnitudes from the initiation of the fault to the steady-state, are extracted and concatenated to create their input datasets. Therefore, The output dataset for each relay is created by assigning $+1$ as the class label for input data samples under forward faults and -1 for the input data samples under reverse faults. Finally, the training dataset is created by combining the input and output datasets. The same process is repeated by applying forward and reverse B-C and A-G faults at each relay station to create training datasets for the L-L and L-G directionality SVMs.

ABC-G faults are applied at 0%, 50%, and 100% of lines in zone 1 and zone 2 of each relay to acquire input data for training their LLL-G zone detection SVM. The MPs recorded by each relay are extracted and concatenated as their input dataset. Output datasets are created by assigning $+1$ class labels for input samples under primary zone faults and -1 to input samples under backup zone faults. Ultimately, the training dataset is created by combining the input and output datasets. The same process is repeated to create training datasets for the L-L and L-G zone detection SVMs by applying B-C and A-G faults at appropriate locations.

All directionality and zone detection training datasets are imported into MATLAB for prepossessing and training. In this paper, 80% of the input dataset is used for training, and the other 20% is used for testing. The input dataset X is normalized as

$$X_{\text{norm}} = \frac{X - \mu}{\sigma}, \tag{3.13}$$

where X_{norm} is the normalized input dataset and μ and σ are the mean and standard deviation of the input dataset. The normalized training datasets are

then used to train SVMs using the MATLAB function `fitcsvm`.

3.4 Performance Analysis

3.4.1 Model Verification

Fig. 3.7 shows the measured harmonic currents for a bolted ABC-G fault at the midpoint of line 9–10. Primary protection is provided by relays R910 and R109, while backup protection is provided by relays R89 and R1110. Relays R98 and R1011 are reverse-looking relays. The primary relays measure MPs with different orientations. This is because the IBRs near each relay inject a different pattern of harmonic currents. Relays on the adjacent lines measure the same pattern of harmonic currents as they see the same current. Fig. 3.8 shows the directionality and zone detection scores for the SVM relays on the primary and adjacent lines. This figure shows that the forward-looking relays have positive directionality scores, while the reverse-looking relays have negative directionality scores. Additionally, the primary relays have positive zone detection scores, while the backup relays have negative zone detection scores. Finally, the relays operate within 3.36 fundamental cycles, which complies with [56].

3.4.2 Fault Type

Fig. 3.9 shows the harmonic currents measured by relay R56 under ABC-G, B-C, and A-G faults at the midpoint of line 56. Fig. 3.9 shows that relay R56 measures the largest harmonic currents under an ABC-G fault, while it measures the smallest harmonic currents under an A-G fault. Fig. 3.10 shows the SVM directionality and zone detection scores for relay R56. This figure shows that the proposed protection scheme operates correctly under all types of faults.

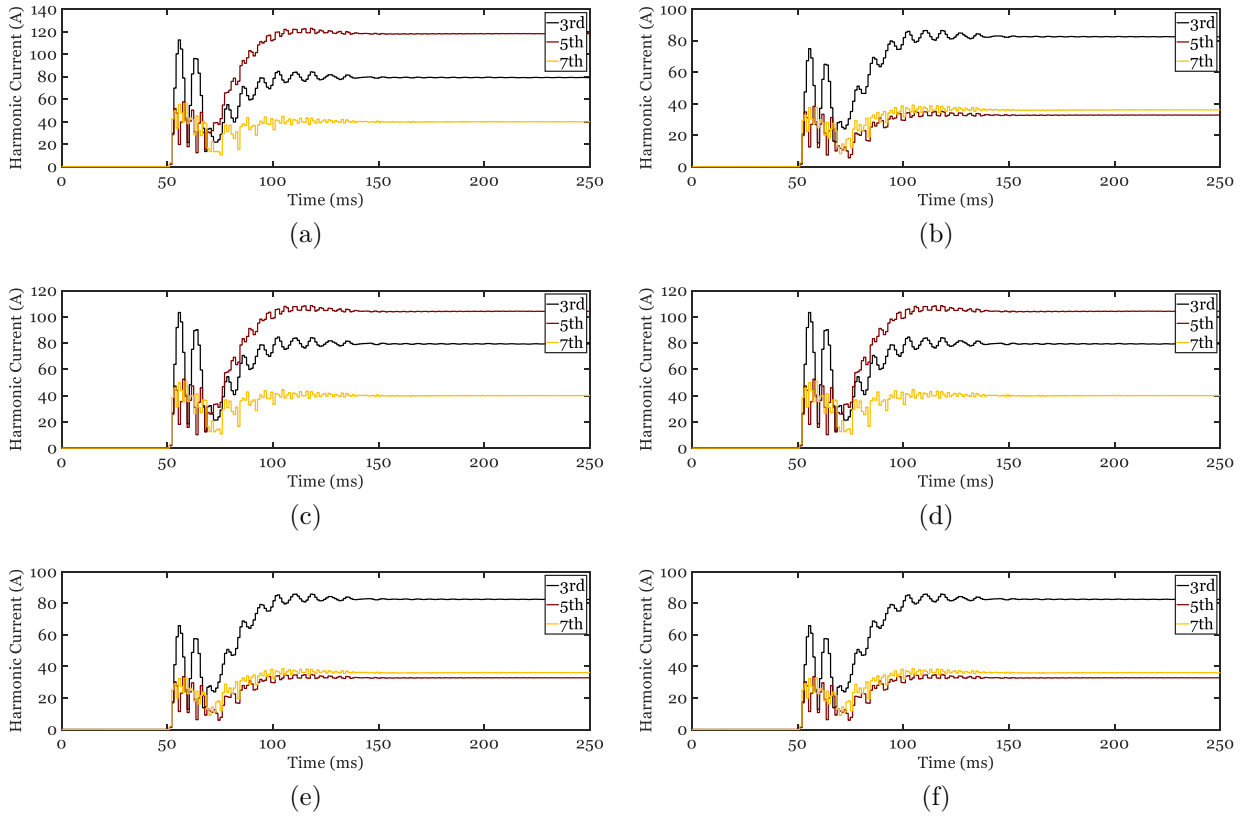

Figure 3.7: Measured harmonic currents by forward- and reverse-looking relays under a bolted ABC-G fault at the midpoint of line 9–10: (a) R910, (b) R109, (c) R89, (d) R98, (e) R1011, and (f) R1110.

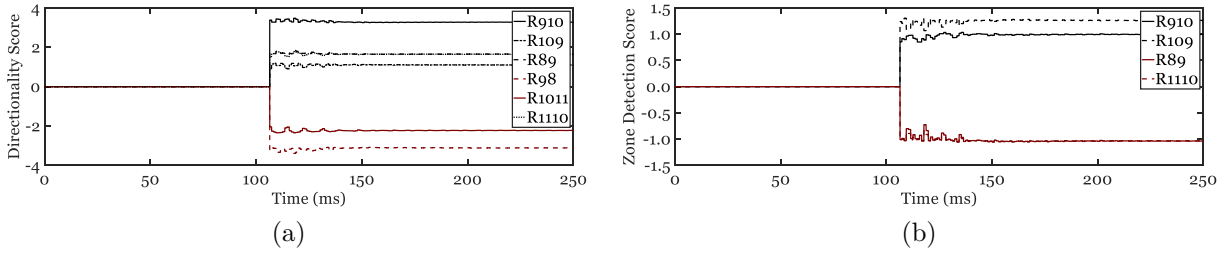

Figure 3.8: SVM (a) directionality and (b) zone detection scores for forward- and reverse-looking relays under a bolted ABC-G fault at the midpoint of line 9–10.

3.4.3 Fault Resistance

Fig. 3.11(a) shows the measured harmonic currents by relay R87 for an ABC-G fault with a fault resistance of 10 Ω at the midpoint of line 8–7. The 5th harmonic current has the largest magnitude, followed by the 3rd and 7th har-

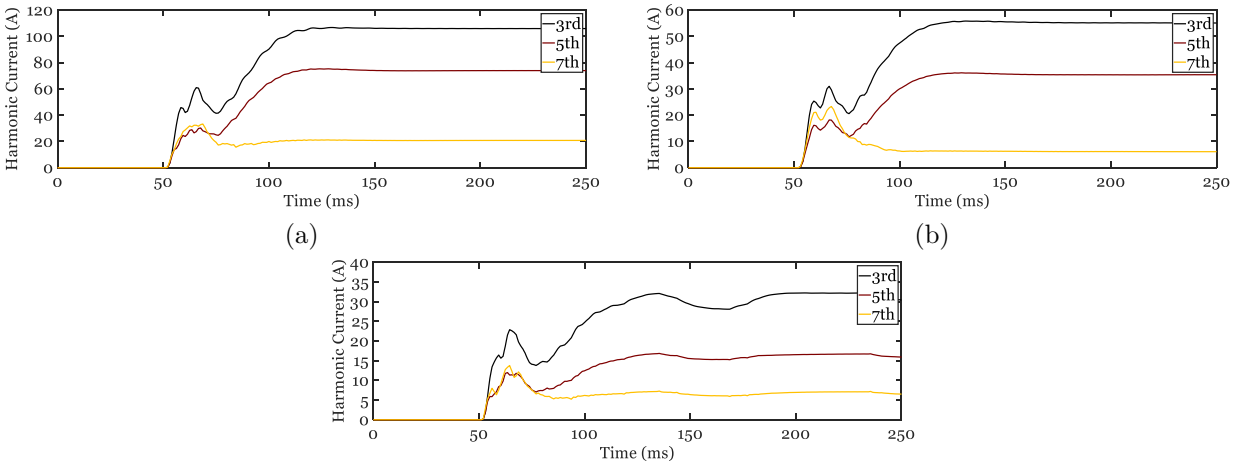

Figure 3.9: Harmonic current measurements by relay R56 under (a) ABC-G, (b) B-C, and (c) A-G faults at the midpoint of line 5–6.

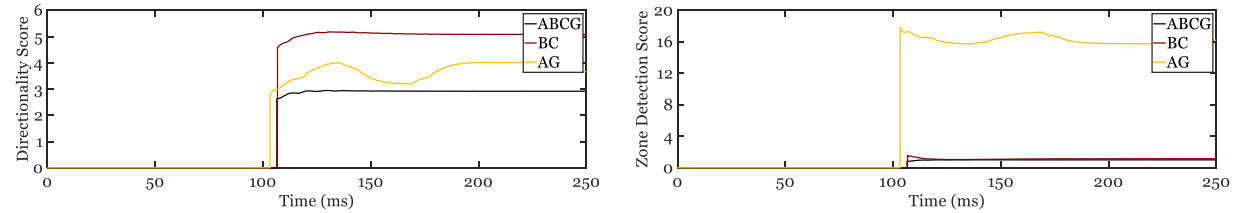

Figure 3.10: SVM (a) directionality and (b) zone detection scores for relay R56 under ABC-G, B-C, and A-G fault at the midpoint of line 5–6.

Table 3.2: Performance Comparison between CS-Based Protection and the Proposed Scheme

Fault Location	F67	F78	F910	F1011	F411	F38	F814
Relay	R65	R76	R98	R109	R1110	R89	R89
CS Score	0.87	0.84	0.84	0.87	0.81	0.83	0.82
SVM Directionality Score	−0.92	−1.11	−3.10	−3.38	−1.82	−1.53	−1.11

monics. Figs. 3.11(b) and (C) show the SVM directionality and zone detection scores for relay R87. Both elements operate correctly after 56 ms, unaffected by fault resistance.

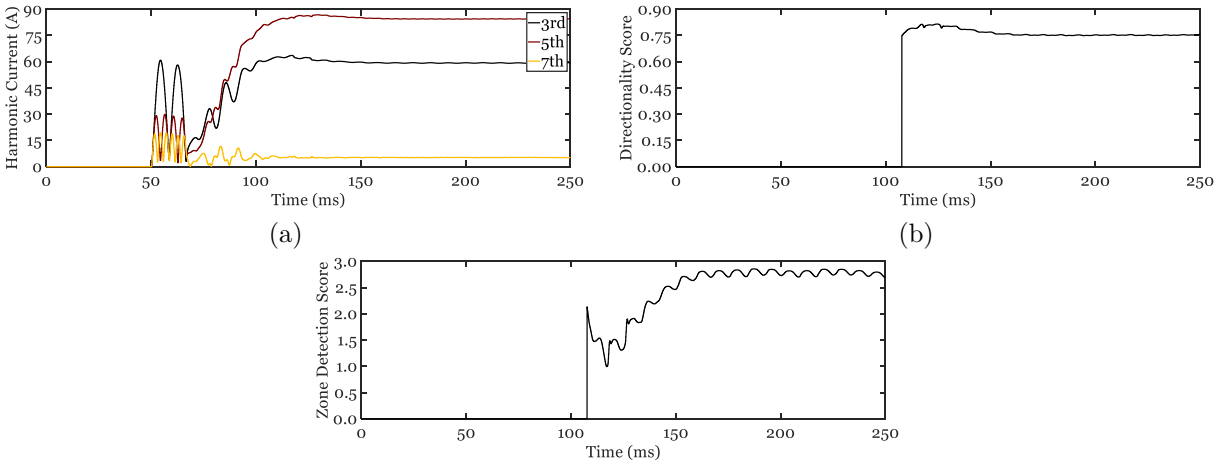

Figure 3.11: Performance summary for relay R87 under an ABC-G fault with a fault resistance of 10 Ω at the midpoint of line 8–7: (a) harmonic current measurements, (b) directionality score, and (c) zone detection score.

3.4.4 Performance Comparison

Table 3.2 compares the performance of the protection scheme in [47] with the proposed SVM-based protection scheme under bolted ABC-G faults at locations F67, F78, F910, F1011, F411, F38, and F814. This table shows that the CS score is above its threshold value of 0.85 for relay R65 at location F67 and relay R109 at location F1011, falsely declaring a forward fault. The CS score is also very close to surpassing is threshold value under the other cases. Although this issue can be fixed using POTT, using CS can be less reliable. On the other hand, the proposed SVM-based method performs correctly for all cases. The SVM directionality score is negative for all cases, correctly declaring a reverse fault. Therefore, the proposed method offers more robustness compared to the method proposed in [47].

Chapter 4

Protection of IBRs Against OC Converter Faults

4.1 Introduction

The modular multilevel converter (MMC) is an attractive topology due to many advantages, including voltage scalability, total modularity, and use of a single DC-link. An MMC consists of several identical semiconductor submodules (SM) connected in series in each phase. SMs consist of insulated-gate bipolar transistors (IGBT). IGBTs are highly fragile, and since an MMC has many IGBTs, they are the most likely elements to fail [61]. There are two types of IGBT failures: short-circuit (SC) and open-circuit (OC). The existing gate-drive circuits provide protection for SC failures. However, OC failures can remain undetected for a long time and cause overvoltage and overcurrent problems. They can also create consecutive OC failures and eventually make the MMC unstable. Moreover, OC faults make the voltages unbalanced and distorted. A faulted GFM MMC degrades the voltage quality throughout the microgrid and may trip other

Portions of this chapter are published as

[60] A. Mohammadhassani and A. Mehrizi-Sani, "Open-circuit submodule fault diagnosis in MMCs using support vector machines," IET Gener. Transm. Distrib., vol. 16, no. 24, pp. 5015-5025, Dec. 2022.

GFL converters as they rely on strong voltage measurements to remain online. Hence, an IGBT failure detection and localization method is required to activate the protection system of the MMC to ensure the reliable MMC and microgrid operation [53], [62], [63].

Various methods are proposed in the literature to detect OC SM faults in MMCs [64]–[73]. These methods can be divided into two groups: hardware-based methods and software-based methods. Hardware-based methods are simple and reliable, but add extra devices and circuitry to the basic MMC design. Moreover, they are not suitable for existing systems as they require restructuring the hardware. Software-based methods, however, do not require any extra devices for OC SM fault diagnosis. Sliding-mode observer is designed in [66] to detect and localize OC SM faults in MMCs. However, it has several drawbacks:

1. It relies on the precise switching model of each SM, which significantly increases their computational burden when the number of SMs is high;
2. They localize the fault when an SM capacitor voltage is higher than the healthy ones, which may significantly increase their detection time;
3. Accurate observer design requires a precise mathematical model of the system. The mathematical model of the MMC is high-order, nonlinear, and highly coupled. Thus, observer design for MMCs can become very complicated.

Kalman filter is utilized in [74] to detect and localize OC SM faults. However, this method has drawbacks as well:

1. Its robustness and accuracy could be put in jeopardy due to long delay between detection and localization;
2. Unless the prediction stage is accurate enough, the capacitor voltage estimation results can be poor.

Besides the shortcomings mentioned above, sliding-mode observer-based methods and Kalman filter-based methods also have some drawbacks in common:

1. They both may become ineffective under nearest-level modulation;
2. Neither method can classify the fault type;
3. Choosing the empirical threshold for these methods can be difficult under different MMC voltage or power ratings.

Utilizing state observers for OC SM fault diagnosis is proposed in [65]. However, it has a long detection time of 50–150 ms, and it is vulnerable to parameter uncertainties. A variance-based statistical method is proposed in [67] to diagnose OC SM faults in MMCs. However, it relies on empirical thresholds, which increase its detection time. Artificial neural networks (ANN) are used in [71] to only classify the OC SM fault. Support vector machine (SVM) is used in [72] to only detect and localize single OC SM faults under double switch failures. Moreover, its training dataset is small, which can affect its accuracy for acting on new data.

This chapter proposes a new method to detect, localize, and classify OC SM faults in MMCs. During OC SM faults, the sorting algorithm of the capacitor voltage balancing block always puts the capacitor voltages of the faulty SMs at the beginning or at the end of the sorted array, depending on arm current direction. Thus, by counting the number of times each SM appears at the beginning of the sorted array when arm current is negative and at the end of the sorted array when arm current is positive, a dataset can be constructed to train a two-class SVM for each SM to detect and localize the OC SM fault. Simultaneously, the sum of the number of times each SM appears at the beginning of the sorted array when arm current is positive and at the end of the sorted array when arm

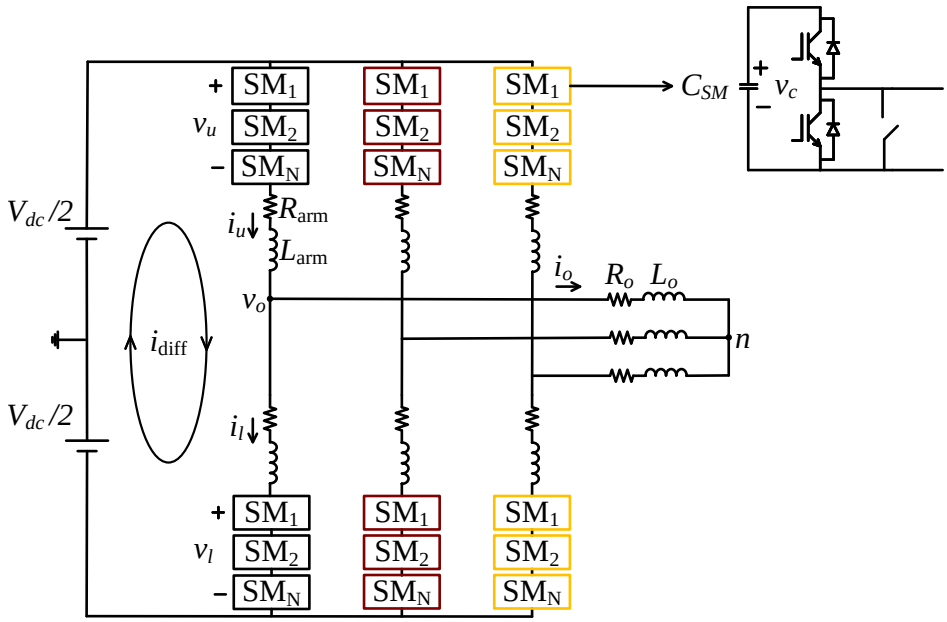

Figure 4.1: Generic topology of a three-phase MMC.

current is negative is used to create a dataset to train a multiclass SVM for each SM to classify the OC SM fault. This method has a consistent detection, localization, and classification time of one fundamental period. Additionally, it does not require any extra hardware or measurements and is very simple to implement.

The performance of the proposed solution is evaluated via various time-domain simulation case studies using a detailed model of an MMC with 4 SMs in each phase arm in PSCAD/EMTDC software.

The specific contributions of this chapter are:

- Statistical analysis of capacitor voltage balancing response to OC SM faults.
- Design of an SVM-based OC SM fault detection and localization method.
- Design of an SVM-based OC SM fault classification method.

4.2 Basics of Operation

4.2.1 Steady-State Operation

Fig. 4.1 shows the generic topology of a three-phase three-wire MMC feeding a balanced inductive load. Each phase consists of two arms, with each arm comprising of N series-connected SMs. Half-bridge SMs (HBSM) are considered in this paper as they are the most common choice [16]. Each HBSM comprises of a capacitor bank, two IGBTs with anti-parallel diodes, and a bidirectional switch to bypass it during OC SM faults.

The instantaneous arm voltages are accumulations of SM output voltages and can be defined using

$$\begin{aligned} v_{u,i} &= \sum_{j=1}^{N} n^i_{u,j} v^i_{cu,j} \\ v_{l,i} &= \sum_{j=1}^{N} n^i_{l,j} v^i_{cl,j} \\ n^i{}_{u,j}, n^i_{l,j} &\in \{0,1\} \\ i &= a,b,c, \end{aligned} \tag{4.1}$$

where $v_{u,i}$ and $v_{l,i}$ are the upper and lower arm output voltages, $n^i_{u,j}$ and $n^i_{l,j}$ are the upper arm and lower arm capacitor insertion indices, and $v^i_{cu,j}$ and $v^i_{cl,j}$ are the upper and lower arm capacitor voltages. The balanced steady-state value of the capacitor voltages V_c is

$$V_c = \frac{V^{\Sigma}_{cu,i}}{N} = \frac{V^{\Sigma}_{cl,i}}{N} = \frac{V_{dc}}{N}, \tag{4.2}$$

where $V_{cu,i}^{\Sigma}$, $V_{cl,i}^{\Sigma}$ are the sum of HBSM capacitor voltages in the upper and lower arms, respectively, and V_{dc} is the DC-side voltage. Therefore, (4.1) is rewritten as

$$\begin{aligned} v_{u,i} &= \frac{V_{cu,i}^{\Sigma}}{N} \sum_{j=1}^{N} n_{u,j}^{i} = N_{u,i} V_{cu,i}^{\Sigma} = N_{u,i} V_{dc} \\ v_{l,i} &= \frac{V_{cl,i}^{\Sigma}}{N} \sum_{j=1}^{N} n_{l,j}^{i} = N_{l,i} V_{cl,i}^{\Sigma} = N_{l,i} V_{dc} \\ N_{u,i}, N_{l,i} &\in \left\{ 0, \frac{1}{N}, \frac{2}{N}, \ldots, 1 \right\} \\ i &= a, b, c, \end{aligned} \tag{4.3}$$

where $N_{u,i}$ and $N_{l,i}$ are the upper and lower arm insertion indices. The line-to-neutral voltage $V_{o,i}$ is defined as

$$V_{o,i} = \frac{v_{l,i} - v_{u,i}}{2}. \tag{4.4}$$

The differential voltage $V_{\text{diff,i}}$ is defined as:

$$V_{\text{diff,i}} = V_{dc} - v_{u,i} - v_{l,i}. \tag{4.5}$$

The circulating current $i_{\text{diff,i}}$ and the output current $i_{o,i}$ of phase i are found as

$$\begin{aligned} i_{\text{diff,i}} &= \frac{i_{u,i} + i_{l,i}}{2} \\ i_{o,i} &= i_{u,i} - i_{l,i} \\ i &= a, b, c, \end{aligned} \tag{4.6}$$

where $i_{u,i}$ and $i_{l,i}$ are the upper and lower arm currents, as shown in Fig. 4.1.

Fig. 4.2 shows a single-phase MMC with $N = 2$. For this topology, there are

$2^2 = 4$ switching states for each arm and $2^4 = 16$ switching states in total. Under capacitor voltage balancing in the steady state, Each SM voltage is equal to $V_c = V_{dc}/2$. Therefore, the output voltage levels that can be produced by this topology are

1. To generate a voltage level of $V_o = V_{dc}/2$, the lower SMs should be inserted and the upper SMs should be bypassed. This means that $v_u = 0$ and $v_l = V_{dc}$. Hence, this requires one switching state and results in $N_u = 0$ and $N_l = 1$.
2. To generate a voltage level of $-V_{dc}/2$, the lower SMs should be bypassed and the upper SMs should be inserted. Therefore, $v_u = V_{dc}$ and $v_l = 0$. Hence, this requires one switching state and results in $N_u = 1$ and $N_l = 0$.
3. To generate a voltage level of 0, at least one SM needs to be bypassed in each arm. This can be obtained using four switching states. Therefore, $v_{u,l} \in \{(V_{dc}/2, V_{dc}/2), (V_{dc}, V_{dc})\}$ and $N_{u,l} \in \{(1/2, 1/2), (1, 1)\}$.

In conclusion, even though there are 16 switching states, only 6 combinations are needed to control the output voltage of this topology.

4.2.2 Dynamic Modeling

Once again, consider the example in Fig. 4.2. Using KVL around loops 1 and 2,

$$\begin{aligned}\frac{V_{dc}}{2} =& n_{u1}v_{cu1} + n_{u2}v_{cu2} + R_{arm}i_u + L_{arm}\frac{di_u}{dt} \\ &+ R_o i_o + L_o \frac{di_o}{dt} \\ \frac{V_{dc}}{2} =& n_{l1}v_{cl1} + n_{l2}v_{cl2} + R_{arm}i_l + L_{arm}\frac{di_l}{dt} \\ &- R_o i_o - L_o \frac{di_o}{dt},\end{aligned} \tag{4.7}$$

where L_{arm} is the arm inductance and R_{arm} is the arm resistance.

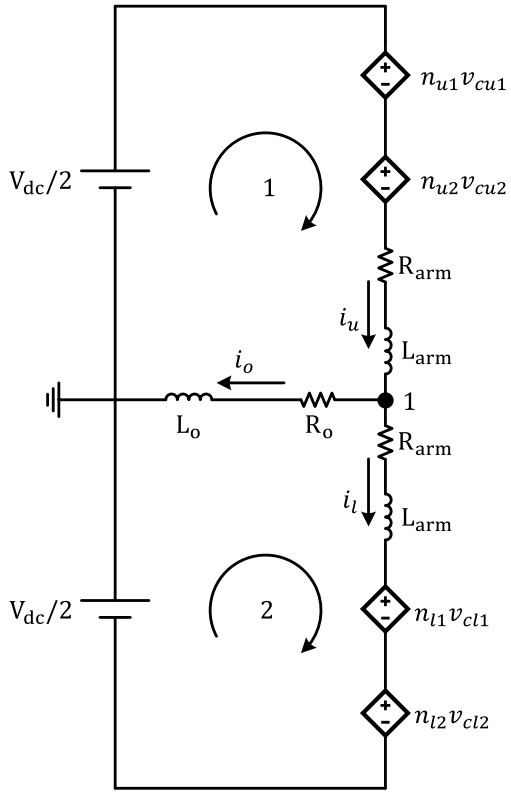

Figure 4.2: Equivalent circuit for a single-phase MMC with $N = 2$.

By adding the two equations in (4.7) and rewriting, the dynamic equation governing i_{diff} is found as

$$\begin{aligned}\frac{di_{\text{diff}}}{dt} =& \frac{1}{2L_{\text{arm}}}[V_{dc} - n_{u1}v_{cu1} - n_{u2}v_{cu2} - n_{l1}v_{cl1} - n_{l2}v_{cl2}] \\ &- \frac{R_{arm}}{L_{arm}}i_{\text{diff}} = \frac{V_{\text{diff}}}{2L_{\text{arm}}} - \frac{R_{arm}}{L_{arm}}i_{\text{diff}}.\end{aligned} \tag{4.8}$$

Equation (4.8) shows that i_{diff} is predominantly controlled using V_{diff}. By applying KCL for each SM capacitor, the dynamic equations governing the capacitor

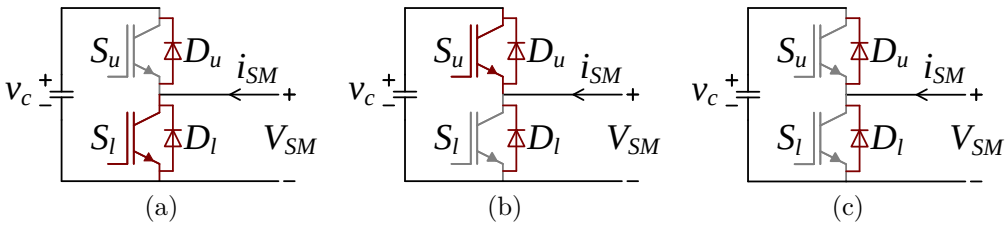

Figure 4.3: OC SM fault cases in MMCs with HBSMs: (a) S_u OC failure, (b) S_l OC failure, and (c) simultaneous S_u and S_l OC failures.

voltages are found as

$$\begin{aligned}
\frac{dv_{cu1}}{dt} &= \frac{n_{u1}}{C_{\text{SM}}} i_u \\
\frac{dv_{cu2}}{dt} &= \frac{n_{u2}}{C_{\text{SM}}} i_u \\
\frac{dv_{cl1}}{dt} &= \frac{n_{l1}}{C_{\text{SM}}} i_l \\
\frac{dv_{cl2}}{dt} &= \frac{n_{l2}}{C_{\text{SM}}} i_l,
\end{aligned} \tag{4.9}$$

where C_{SM} is the HBSM capacitance. Equation (4.9) shows that the capacitor voltages are related to switched arm currents. By rewriting (4.8) and (4.9) for sum of capacitor voltages using (4.2) and generalizing, the complete dynamic model of the MMC is found as

$$\begin{cases}
\dfrac{di_{\text{diff,i}}}{dt} = \dfrac{1}{2L_{\text{arm}}} V_{\text{diff,i}} - \dfrac{R_{\text{arm}}}{L_{\text{arm}}} i_{\text{diff,i}} \\
\dfrac{dV^{\Sigma}_{cu,i}}{dt} = \dfrac{NN_{u,i}}{C_{\text{SM}}} i_{u,i} \\
\dfrac{dV^{\Sigma}_{cl,i}}{dt} = \dfrac{NN_{l,i}}{C_{\text{SM}}} i_{l,i}.
\end{cases} \tag{4.10}$$

4.3 MMC Operation under OC SM Faults

Fig. 4.3 shows the three types of OC SM faults depending on the failed IGBT: OC failure in the upper IGBT (S_u), OC failure in the lower IGBT (S_l), and

Table 4.1: Effects of S_u OC Failure on MMC Operation

SM Current i_{SM}	**Voltage Response**	
	Normal Operation	S_u OC Failure
Positive	Insert (Charging) Bypass (Unchanged)	Insert (Charging) Bypass (Unchanged)
Negative	Insert (Discharging) Bypass (Unchanged)	Insert (Unchanged) Bypass (Unchanged)

OC failure in both IGBTs (S_u and S_l). The MMC has a different response to each OC IGBT failure case. Therefore, MMC operation is analyzed for each case according to the reference SM current direction depicted in Fig. 4.3.

4.3.1 S_u OC Fault

Table 4.1 summarizes the effects of S_u OC failure on MMC operation. If i_{SM} is positive, S_u OC failure does not affect MMC operation, as the current passes through D_u and C_{SM}, while charging and through S_l while bypassed. However, if i_{SM} is negative, the current flows only through D_l. Therefore, the HBSM capacitor loses its ability to discharge under S_u failures. However, it only charges when it is inserted during positive arm current.

4.3.2 S_l OC Failure

Table 4.2 summarizes the effects of MMC operation under S_l OC failure. In this case, MMC operation is unaffected if i_{SM} is negative. Therefore, the HBSM capacitor can discharge when the HBSM is inserted. However, when the i_{SM} is positive, the HBSM current flows via D_u and C_{SM}, regardless of the control command. Therefore, the HBSM capacitor charges for the entire duration of positive arm current. Therefore, the charging speed of the HBSM capacitor is faster than that under S_u faults.

Table 4.2: Effects of S_l OC Failure on MMC Operation

SM Current i_{SM}	**Voltage Response**	
	Normal Operation	S_l OC Failure
Positive	Insert (Charging) Bypass (Unchanged)	Insert (Charging) Bypass (Charging)
Negative	Insert (Discharging) Bypass (Unchanged)	Insert (Discharging) Bypass (Unchanged)

Table 4.3: Effects of Simultaneous S_u and S_l OC Failures on MMC Operation

SM Current i_{SM}	**Voltage Response**	
	Normal Operation	S_u&S_l OC Failure
Positive	Insert (Charging) Bypass (Unchanged)	Insert (Charging) Bypass (Charging)
Negative	Insert (Discharging) Bypass (Unchanged)	Insert (Unchanged) Bypass (Unchanged)

4.3.3 Simultaneous S_u and S_l OC Failures

Table 4.3 summarizes the effects of simultaneous S_u and S_l OC failures on MMC operation. In this case, the MMC operation is affected for both arm current directions. When i_{SM} is positive, the HBSM is not bypassed and the HBSM capacitor keeps charging through D_u. Therefore, the HBSM capacitor charges during the entire positive arm current time period. When i_{SM} is negative, the HBSM is bypassed via D_l and does not discharge. Therefore, the HBSM capacitor voltage remains unchanged for the entire duration of negative arm current. In summary, the HBSM capacitor keeps charging with a rate higher than that under both S_u and S_l failures.

4.4 Proposed OC SM Fault Diagnosis Method

4.4.1 Capacitor Voltage Balancing During OC SM Failures

Capacitor voltage balancing is an essential block of the MMC control system. This block makes sure that the charging and discharging of SM capacitors in each phase arm are balanced, so that the MMC can properly accomplish its control objectives. The capacitor voltage balancing algorithm used in this paper is summarized as below:

1. If arm current is positive, capacitors need to be charged. Thus, the capacitor voltages are sorted in ascending order and capacitors with lower voltages are inserted.
2. If arm current is negative, capacitors need to be discharged. Thus, the capacitor voltages are sorted in descending order and capacitors with higher voltages are inserted.

The sum of the number of times the ith capacitor voltage appears in the first slot of the sorting array during negative arm current and in the last slot during positive arm current $N_{\text{sum},i}^{\text{discharge}}$ for one fundamental period T_o shows how severely the capacitor voltage balancing algorithm wants to discharge that capacitor. Ideally, $N_{\text{sum},i}^{\text{discharge}}$ has an integer value, which is calculated using

$$N_{\text{sum},i}^{\text{discharge}} = \frac{T_o}{NT_{\text{SW}}}, \tag{4.11}$$

where T_{SW} is the switching period and N is the number of SMs in one arm. However, this does not hold true in practice as N and T_{SW} are designed according

to different rules. Therefore, $N_{\text{sum},i}^{\text{discharge}}$ becomes a random variable with a mean of

$$\mu = \frac{T_o}{NT_{\text{SW}}}. \tag{4.12}$$

Using l samples of $N_{\text{sum},i}^{\text{discharge}}$, the standard deviation σ of $N_{\text{sum},i}^{\text{discharge}}$ is

$$\sigma = \sqrt{\frac{1}{l}\sum_{j=1}^{l}\left(N_{\text{sum},i,j}^{\text{discharge}} - \mu\right)^2}. \tag{4.13}$$

Using (4.12) and (4.13), a Gaussian distribution $f\left(N_{\text{sum},i}^{\text{discharge}}\right)$ can be fit to $N_{\text{sum},i}^{\text{discharge}}$ as

$$f\left(N_{\text{sum},i}^{\text{discharge}}\right) = \frac{1}{\sigma\sqrt{2\pi}} e^{-\frac{1}{2}\left(\frac{N_{\text{sum},i}^{\text{discharge}} - \mu}{\sigma}\right)^2}. \tag{4.14}$$

The probability of $N_{\text{sum},i}^{\text{discharge}}$ falling between a and b is found by calculating the area under the curve in (4.14) using

$$P[a \leq N_{\text{sum},i}^{\text{discharge}} \leq b] = \int_a^b f\left(N_{\text{sum},i}^{\text{discharge}}\right) dN_{\text{sum},i}^{\text{discharge}}. \tag{4.15}$$

$N_{\text{sum},i}^{\text{discharge}}$ can be used to detect and localize OC SM faults. Fig. 4.4(a) shows a graphical representation of $f\left(N_{\text{sum}}^{\text{discharge}}\right)$ during normal operation. Around 99.7% of the area under the curve in Fig. 4.4(a) is covered by values between $\mu - 2\sigma$ and $\mu + 2\sigma$. That is, it is most likely that $N_{\text{sum},i}^{\text{discharge}}$ will fall within this range during normal operation of the MMC. On the other hand, as shown in Fig. 4.4(b), the capacitor voltage of the faulty SM increases beyond that of the remaining healthy SMs during OC SM faults. This means that the capacitor voltage balancing algorithm keeps trying to discharge it and always puts it either in the first slot or the last slot of the sorting array. Hence, its $N_{\text{sum},i}^{\text{discharge}}$ increases

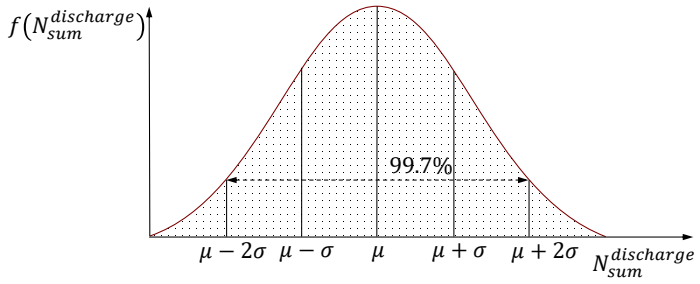

(a)

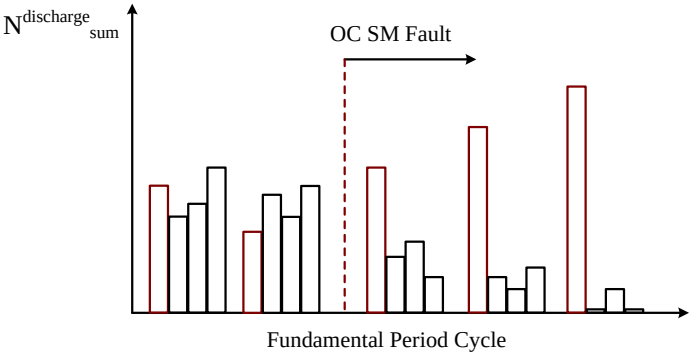

(b)

Figure 4.4: Sample graphical representations of (a) $f(N_{\text{sum}}^{\text{discharge}})$ during normal operation and (b) $N_{\text{sum}}^{\text{discharge}}$ during normal and faulty operation.

at the onset of an OC SM fault and finally saturates at T_o/T_{SW}. This means that the probability of $N_{\text{sum}}^{\text{discharge}}$ appearing in the normal region decreases for the faulty SM until it becomes zero. This shows that $N_{\text{sum},i}^{\text{discharge}}$ can be used to detect and localize OC SM faults. Analogous to $N_{\text{sum},i}^{\text{discharge}}$, the sum of the number of times the ith capacitor voltage appears in the first slot of the sorting array during negative arm current and in the last slot during positive arm current $N_{\text{sum},i}^{\text{charge}}$ for one fundamental period T_o shows how severely the capacitor voltage balancing algorithm needs to charge that capacitor. $N_{\text{sum},i}^{\text{charge}}$ can be used to distinguish between the three types of OC SM faults. The capacitor voltages of the faulty SM increases with a different rate of change under each type of fault. Therefore, its $N_{\text{sum},i}^{\text{charge}}$ decreases to zero with a different rate of change under each type of fault. The capacitor voltages of the remaining healthy SMs respond differently

to the three types of OC SM faults. Thus, $N_{\text{sum},i}^{\text{charge}}$ values of the SMs are different under each type of fault and they can be used to distinguish between OC SM fault.

4.4.2 OC SM Fault Diagnosis Using SVM

OC SM fault diagnosis can be solved as a classification problem in the realm of machine learning. Classification refers to a problem where a class label is predicted for a sample input data. An established classification method is the support vector machine (SVM) [58]. SVM eliminates the need for setting empirical thresholds. Moreover, SVM provides superior classification performance using the kernel trick with faster training. Additionally, it offers a simpler implementation, which boosts its testing speed [75]. Therefore, it is a viable and better solution to the problem of OC SM fault diagnosis. SVM separates two classes via finding an optimal hyperplane in a multidimensional space. For linearly-separable datasets, the optimal hyperplane that separates the two classes with target labels $t_i = \pm 1$ is defined as

$$y(x) = w^T \phi(x) + b, \tag{4.16}$$

where $y(x)$ is the score, w is the vector containing the weight factors, $\phi(x)$ is a feature-space transformation, and b is the bias. In a two-dimensional input space, $y(x)$ becomes a straight line, such the one shown in Fig. 4.5. If $y(x) > 0$, the label $+1$ is predicted; otherwise, the label -1 is predicted. The objective of SVM is to maximize the margin ρ between selected support vectors of the two

classes or minimize $\|w\|$ by solving

$$\begin{aligned} &\min_{w} \ \frac{1}{2}||w||^2 + C\sum_{i=1}^{n}\zeta_i \\ &\text{subject to } \ t_i\left(w\cdot x_i + b\right) \geq 1-\zeta_i, \ \ \zeta_i \geq 0 \ \ \forall i, \end{aligned} \tag{4.17}$$

where C is a cost parameter, n is the length of the training dataset, and ζ_i is the penalty assigned for the ith nonseparable feature vector. This problem is usually simplified into its dual form and easily solved by quadratic programming:

$$\begin{aligned} &\max \ L_D = \sum_i \alpha_i - \frac{1}{2}\sum_{i,j}\alpha_i\alpha_j y_i y_j x_i^T x_j \\ &\text{subject to } \ 0 \leq \alpha_i \leq C \ \ \forall i, \ \ \sum_i \alpha_i y_i = 0, \end{aligned} \tag{4.18}$$

where α is a Lagrangian multiplier. To improve classification for nonseparable datasets, a kernel function $K(x_i, x_j) = \phi(x_i)^T\phi(x_j)$ is used. Kernels are mathematical functions that are used to convert linearly inseparable input datasets to linearly separable ones by converting the input dataset to one with higher dimensions. Three major types of kernel functions are the linear kernel $K(x_i, x_j) = {x_i}^T x_j$, the polynomial kernel $K\left(x_i, x_j\right) = \left(\gamma\left(x_i \cdot x_j\right) + r\right)^d$, and the Gaussian kernel $K\left(x_i, x_j\right) = \exp\left(-\gamma||x_i - x_j||^2\right)$. After the proper kernel is selected, the optimal hyperplane in (4.16) becomes

$$y\left(x\right) = \text{sign}\left(\sum_{i=1}^{n}\alpha_i t_i K\left(x, x_i\right) + b\right), \tag{4.19}$$

where b is calculated by solving $\alpha_i\left(t_i\left(w\cdot x_i + b\right) - 1\right) = 0, i = 1, \ldots, n$, such that α_i is not zero. Two SVMs are trained for each SM: one for detection and localization of OC SM faults and another for classifying the fault type. The

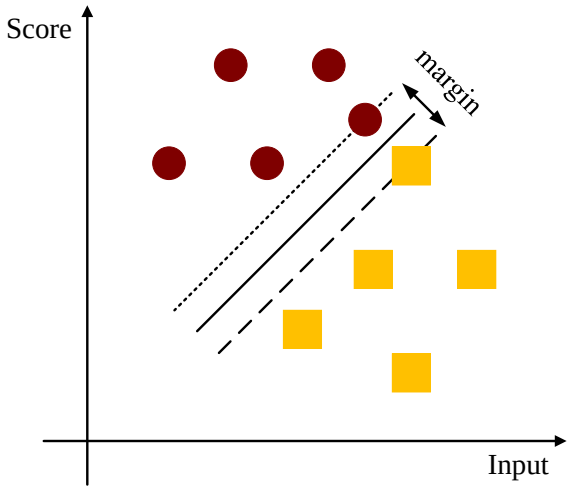

Figure 4.5: A linearly-separable sample training data.

feature samples for the detection and localization SVM of one SM consist of $N_{\text{sum},i}^{\text{discharge}}$ data from all SMs in the same arm obtained by applying all three types of OC SM faults on that particular SM. In this way, the SVM detects and localizes the OC SM fault simultaneously in T_o seconds. The `fitcsvm` function in MATLAB is used to train the detection and localization SVM. The Gaussian kernel is selected for this purpose due to its ability to classify highly nonseparable datasets. To classify the OC SM fault type, a multiclass SVM is trained for each SM using the $N_{\text{sum},i}^{\text{charge}}$ data from all SMs in the same arm as feature samples obtained by applying all three types of OC SM faults on that particular SM. Afterwards, the `fitcecoc` function in MATLAB is used to train the OC fault classification SVM using the Gaussian kernel. Solving classification problems with multiple classes is not inherently supported by SVM. Therefore, various coding designs are available to break down the multiclass classification problem into multiple two-class ones. The *one-versus-one* method is used in this paper as the coding design. This method splits a multiclass classification problem into multiple two-class classification problems. The multiclass dataset is split into one dataset for each class against every other class and the class with the majority

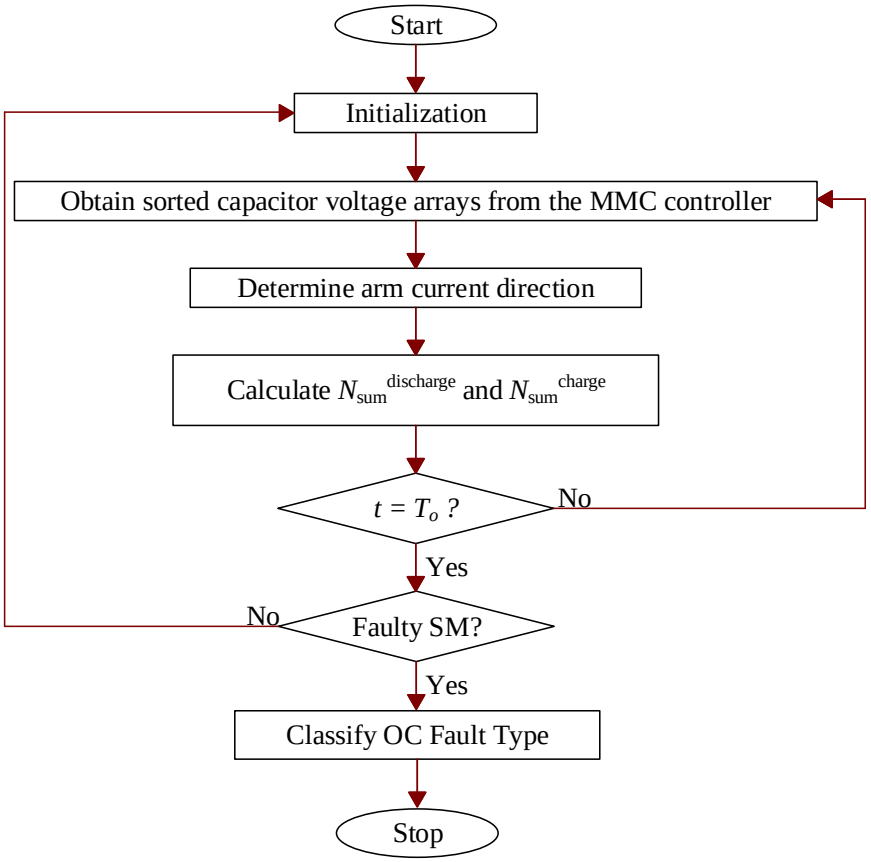

Figure 4.6: Proposed SVM-based OC SM fault diagnosis method.

of votes is predicted as the class label. Fig. 4.6 summarizes the proposed SVM-based OC SM fault diagnosis method:

1. Initialize timer, $N_{\text{sum},i}^{\text{discharge}}$, and $N_{\text{sum},i}^{\text{charge}}$.
2. Obtain the sorted capacitor voltage arrays from the MMC controller.
3. Determine arm current direction.
4. Calculate $N_{\text{sum},i}^{\text{discharge}}$ and $N_{\text{sum},i}^{\text{charge}}$ for each SM according to arm current direction.
5. If timer has reached T_o, pass $N_{\text{sum},i}^{\text{discharge}}$ of each SM to its detection and localization SVM. Otherwise, go to step two.
6. If a fault is detected, pass $N_{\text{sum},i}^{\text{charge}}$ of all SMs to the fault classification SVM of the faulty SM to classify fault type.

4.5 Performance Evaluation

4.5.1 Training Data Acquisition and Statistical Analysis

A detailed model of a three-phase nine-level MMC with $N = 4$ is built in PSCAD/EMTDC using the topology shown in Fig. 4.1 to simulate all types of OC SM faults on each SM to obtain training data for each SVM. Table 4.4 summarizes the simulation parameters. The capacitance is calculated using the method in [76] to achieve a 5% voltage ripple. The switching angles are calculated using exchange market algorithm [77] to eliminate harmonics 5 to 43. The MPC controller proposed in [53] is used in this paper. The OC SM fault should be diagnosed in less than 100 ms to avoid subsequent damage to other devices [66]. Therefore, 20 fundamental cycles worth of training data is extracted from the simulation, of which 10 fundamental cycles belong to normal operation and 10 fundamental cycles belong to abnormal operation. Each type of fault is simulated at ten different time instances to create a diverse training dataset for each SM. Training dataset for detection and localization SVM of one SM consists of $N_{\text{sum},i}^{\text{discharge}}$ of that SM under each type of fault. Therefore, the size of the feature matrix is 600×1 for each SM with an average training time of 2.12 s. The training dataset for the fault type classification SVM of one SM consists of $N_{\text{sum},i}^{\text{charge}}$ of all four SMs in one arm under each type of fault. To increase the accuracy of the fault type classification SVM, the variance and Euclidean norm of each feature sample is also added to the feature matrix of each SM. Thus, the feature matrix grows to have a size of 600×6 for each SM with an average training time of 3.04 s. The number of features and training instances in the proposed method increases with the number of SMs per arm. The computational cost of SVM

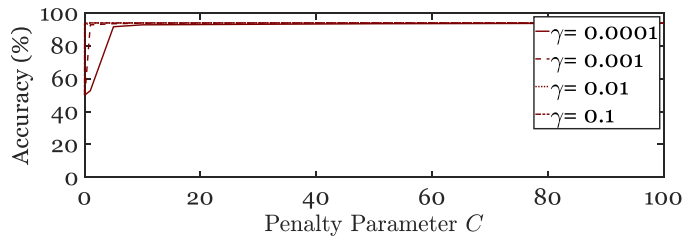

(a)

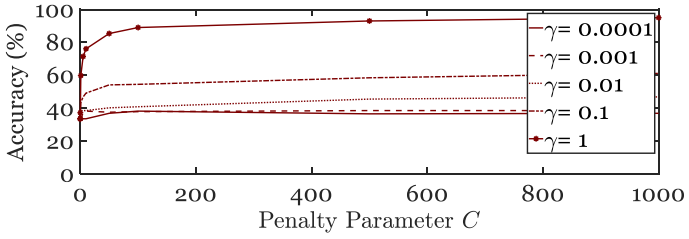

(b)

Figure 4.7: Learning curves for (a) detection and localization SVM and (b) classification SVM of SM_{ua1}.

increases like t^2 for smaller values of C, while it increases like t^3 for larger values of C. Therefore, the number of training samples should not be too high to avoid long training and testing times for SVM [78]. An SM has the same response to an OC SM fault regardless of its position in the phase arm. Therefore, a fault detection and localization trained for one SM can be used for all SMs in that arm. Moreover, phase shift does not have an effect on the response of capacitor voltage balancing to OC SM faults. Therefore, the trained detection and localization SVM can be used for all SMs in an MMC. The capacitor voltages of the remaining healthy SMs remain balanced under OC SM faults. Therefore, $N_{\text{sum}}^{\text{charge}}$ data obtained from the faulty SM and a selected number of remaining healthy SMs is sufficient for training the fault type classification SVM. The trained fault type classification SVM, however, is not going to respond accurately to faults in other SMs as it needs a relatively larger training dataset to be accurate enough. However, even though classifying the OC SM fault type is desirable, it does not affect the performance of the detection and localization SVM, which diag-

Table 4.4: Simulation Parameters

Parameter	**Value**
Number of HBSMs in each phase arm N	4
DC-link voltage V_{dc}	10.87 kV
HBSM capacitance C_{SM}	1200 μF
Arm inductance L_{arm}	9 mH
Load resistance R_o	12 Ω
Load inductance L_o	4 mH
Fundamental frequency f_o	60 Hz
Modulation index m_a	0.8
Sampling frequency f_s	50 kHz
Rated V_c for normal operation	2.72 kV
Rated V_c for FT operation	3.62 kV

noses and bypasses the faulty SM in only one fundamental period cycle. Both SVM models are trained for γ and C values of $0.0001, 0.001, 0.01, 0.1, 1$. Model accuracy is then calculated for all pairs of γ and C using

$$\text{Accuracy}\% = \frac{\text{Number of Correctly Predicted Samples}}{\text{Total Number of Samples}}. \tag{4.20}$$

Next, model accuracy is plotted versus γ and C and the best performing model is chosen for implementation.Fig. 4.7(a) shows the training accuracy curves for the detection and localization SVM. The parameters $\gamma = 0.001$ and $C = 5$ are selected for the detection and localization SVM, resulting in an accuracy of 94.18%. Fig. 4.7(b) shows the training accuracy curves for the fault type classification SVM The parameters $\gamma = 1$ and $C = 500$ are selected for the detection and localization SVM, yielding an accuracy of 93.02%.

4.5.2 Case 1: S_u Fault in SM$_{ua1}$

To evaluate the performance of the proposed OC SM fault diagnosis method on new data, an OC fault is applied to the top switch in SM$_1$ in the upper arm of phase a at $t = 100$ ms. Fig. 4.8(a) shows v_{cua}. Prior to $t = 100$ ms, the capacitor voltages are balanced at 2.5 kV each. After $t = 100$ ms, the capacitor voltages

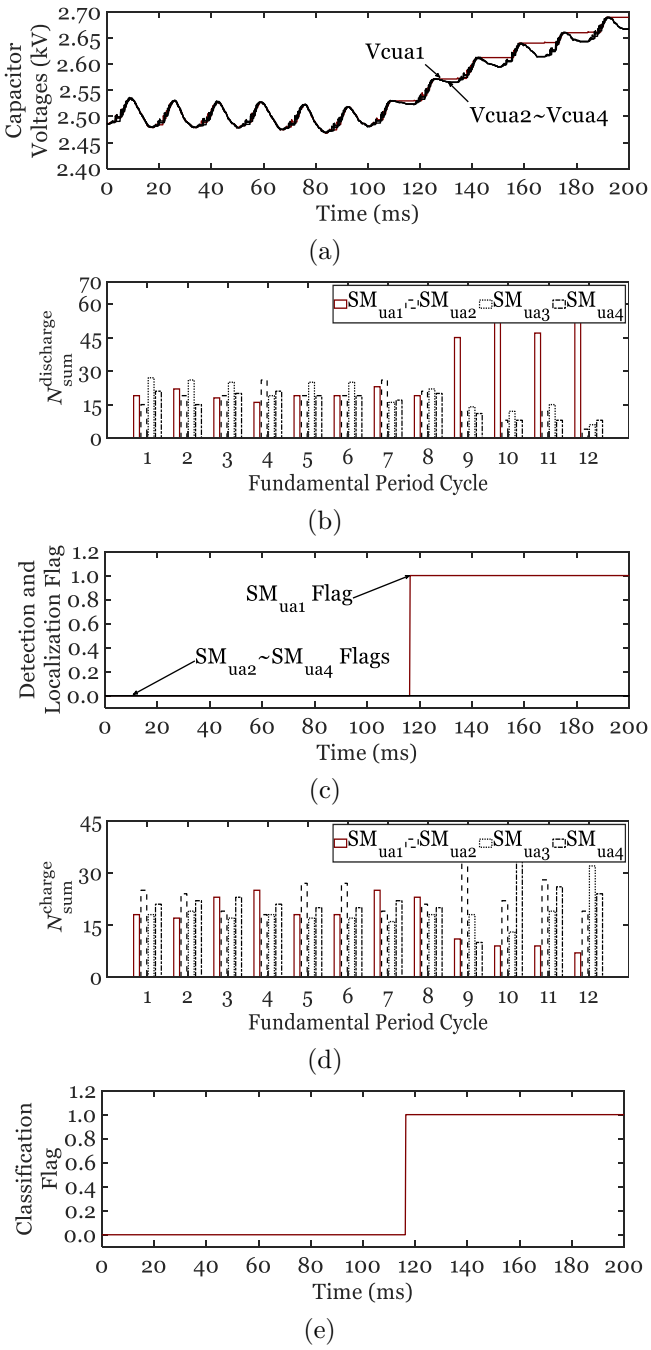

Figure 4.8: Simulation results after applying a S_u fault in SM_{ua1}: (a) capacitor voltages of SMs in the upper arm of phase a, (b) $N_{sum}^{discharge}$ for SMs in the upper arm of phase a, (c) detection and localization flag for SMs in the upper arm of phase a, (d) N_{sum}^{charge} for SMs in the upper arm of phase a, and (e) classification flag for SM_{ua1}.

start to increase, as described in Table 4.1. Fig. 4.8(b) shows $N_{sum}^{discharge}$ for SMs in the upper arm of phase a at each fundamental period cycle during simulation.

Fig. 4.8(b) shows that before $t = 100$ ms, or the 6th fundamental period cycle, $N_{\text{sum}}^{\text{discharge}}$ for all SMs is between 10 and 30. Fig. 4.8(b) also shows that $N_{\text{sum}}^{\text{discharge}}$ values remain in the same range for up to two fundamental period cycles after $t = 100$ ms. After that, $N_{\text{sum}}^{\text{discharge}}$ starts to increase drastically for SM_{ua1} and decrease significantly for the other SMs. Fig. 4.8(c) shows that SVM detects and localizes the OC SM fault in one fundamental period cycle, or 16.67 ms. Fig. 4.8(d) shows $N_{\text{sum}}^{\text{charge}}$ for SMs in the upper arm of phase a. Similar to $N_{\text{sum}}^{\text{discharge}}$, $N_{\text{sum}}^{\text{charge}}$ remains close to its prefault values for two fundamental period cycles after the fault. Afterwards, $N_{\text{sum}}^{\text{charge}}$ for SM_{ua1} drastically decreases, while others increase. Fig. 4.8(e) shows that SVM predicts the correct type of fault in one fundamental period cycle or 16.67 ms.

4.5.3 Case 2: S_l Fault in SM_{ua1}

Fig. 4.9(a) shows v_{cua}. Prior to $t = 100$ ms, capacitor voltages are balanced at 2.5 kV each. At $t = 100$ ms, a S_l fault occurs in SM_{ua1} and its capacitor voltage starts to increase, while other capacitor voltages start to decrease. Fig. 4.9(b) shows $N_{\text{sum}}^{\text{discharge}}$ for SMs in the upper arm of phase a. Prior to $t = 100$ ms, or the 6th fundamental cycle, $N_{\text{sum}}^{\text{discharge}}$ varies between 10 and 30. This figure also shows that $N_{\text{sum}}^{\text{discharge}}$ values remain in the same range for up to two fundamental period cycles after $t = 100$ ms. After that, $N_{\text{sum}}^{\text{discharge}}$ starts to increase drastically for SM_{ua1} and decrease significantly for other SMs. Fig. 4.9(c) shows that SVM is able to detect and localize the fault in 16.67 ms. Fig. 4.9(d) shows $N_{\text{sum}}^{\text{charge}}$ for SMs in the upper arm of phase a. Similar to $N_{\text{sum}}^{\text{discharge}}$, $N_{\text{sum}}^{\text{charge}}$ remains close to its prefault values for two fundamental period cycles after the fault. Afterwards, $N_{\text{sum}}^{\text{charge}}$ for SM_{ua1} drastically decreases while others increase. Fig. 4.9(e) shows that SVM predicts the correct type of fault in 16.67 ms.

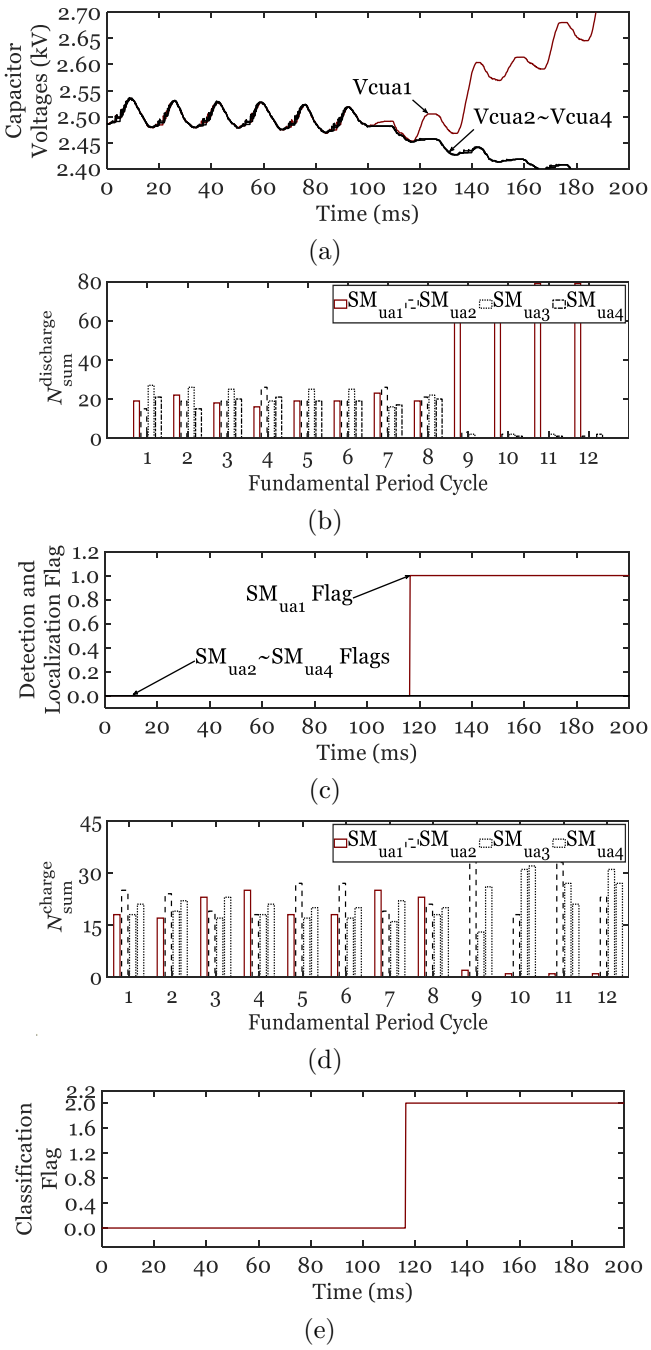

Figure 4.9: Simulation results after applying a S_l fault in SM$_{ua1}$: (a) capacitor voltages of SMs in the upper arm of phase a, (b) $N_{\text{sum}}^{\text{discharge}}$ for SMs in the upper arm of phase a, (c) detection and localization flag for SMs in the upper arm of phase a, (d) $N_{\text{sum}}^{\text{charge}}$ for SMs in the upper arm of phase a, and (e) classification flag for SM$_{ua1}$.

4.5.4 Case 3: Simultaneous S_u and S_l Faults in SM$_{ua1}$

Fig. 4.10(a) shows v_{cua}. Prior to $t = 100$ ms, the capacitor voltages are balanced at 2.5 kV each. At $t = 100$ ms, simultaneous S_u and S_l faults occur in SM$_{ua1}$.

Table 4.5: Performance Comparison with other Proposed Methods

Fault Diagnosis Method	Su Failure Diagnosis Time	Sl Failure Diagnosis Time	Su&Sl Failure Diagnosis Time
Proposed Method	16.67 ms	16.67 ms	16.67 ms
[67]	27 ms	11 ms	N/A
[68]	15.3 ms	9.2 ms	9 ms
[70]	12 ms	10 ms	N/A
[79]	11.9 ms	11.8 ms	N/A

Fig. 4.10(a) shows that v_{cua1} immediately starts to increase at the onset of the fault, while getting bypassed intermittently, and others decrease. Fig. 4.10(b) shows $N_{\text{sum}}^{\text{discharge}}$ for SMs in the upper arm of phase a. Prior to $t = 100$ ms, or the 6th fundamental cycle, $N_{\text{sum}}^{\text{discharge}}$ varies between 10 and 30. This figure also shows that $N_{\text{sum}}^{\text{discharge}}$ values remain in the same range for up to two fundamental period cycles after $t = 100$ ms. After that, $N_{\text{sum}}^{\text{discharge}}$ starts to increase drastically for SM_{ua1} and decrease significantly for other SMs. Fig. 4.10(c) shows that SVM is able to detect and localize the fault in 16.67 ms. Fig. 4.10(d) shows $N_{\text{sum}}^{\text{charge}}$ for SMs in the upper arm of phase a. Similar to $N_{\text{sum}}^{\text{discharge}}$, $N_{\text{sum}}^{\text{charge}}$ remains close to its prefault values for two fundamental period cycles after the fault. Afterwards, $N_{\text{sum}}^{\text{charge}}$ for SM_{ua1} starts to drastically decrease while it increases for other SMs. Fig. 4.10(e) shows that SVM predicts the correct type of fault in 16.67 ms.

4.5.5 Performance Comparison

Table 4.5 summarizes the performance of the proposed method and some other recently published methods under all three types of OC SM faults. This table shows that the proposed method offers a consistent diagnosis time of 16.67 ms for all types of OC SM faults. On the other hand, this is not the case for the other listed methods. The method proposed in [67] diagnoses S_u failures in 27 ms and S_l failures in 11 ms. However, it cannot diagnose S_u&S_l failures. The method proposed in [68] diagnoses S_u failures in 15.3 ms, which is more than 6 ms longer

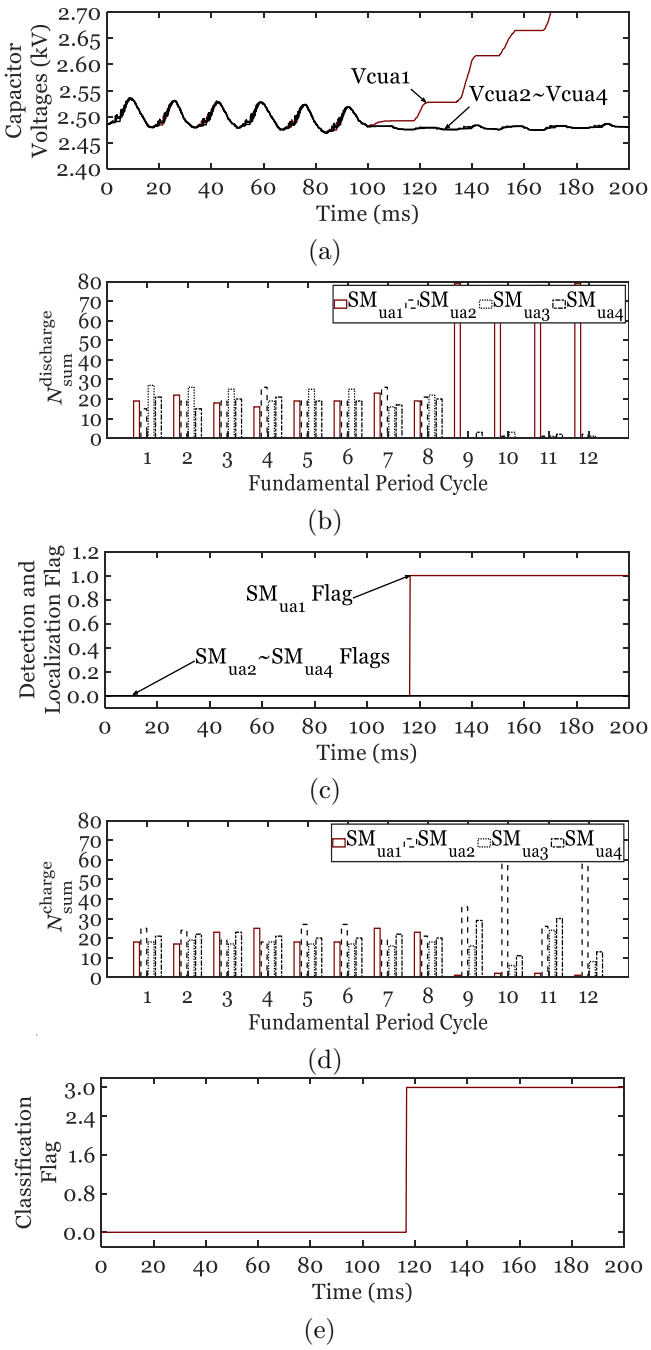

Figure 4.10: Simulation results after applying S_u and S_l faults in SM$_{ua1}$: (a) capacitor voltages of SMs in the upper arm of phase a, (b) $N_{\text{sum}}^{\text{discharge}}$ for SMs in the upper arm of phase a, (c) detection and localization flag for SMs in the upper arm of phase a, (d) $N_{\text{sum}}^{\text{charge}}$ for SMs in the upper arm of phase a, and (e) classification flag for SM$_{ua1}$.

than its diagnosis time for the other two types of faults. It is desirable that the fault diagnosis scheme has a consistently fast response to all types of OC

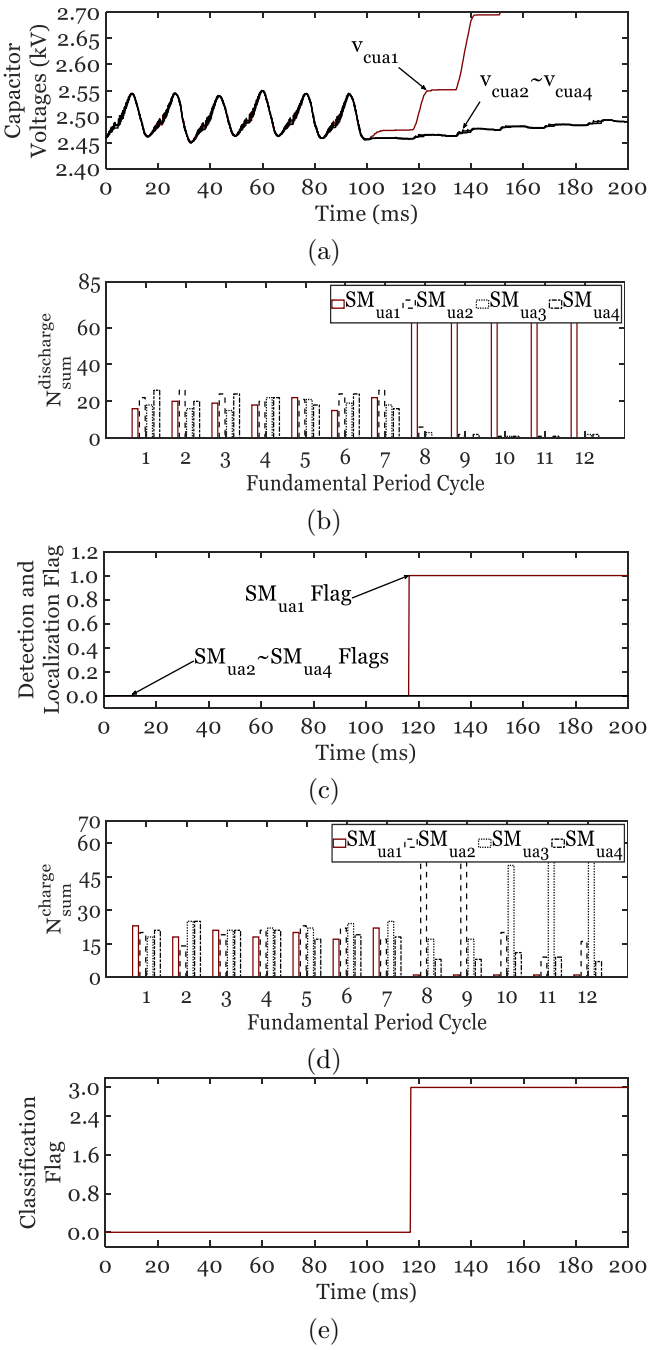

Figure 4.11: Simulation results after applying S_u and S_l faults in SM_{ua1} with $C_{\mathrm{SM}}^{\mathrm{new}} = 0.8C_{\mathrm{SM}}$ and $L_{\mathrm{arm}}^{\mathrm{new}} = 1.2L_{\mathrm{arm}}$: (a) capacitor voltages of SMs in the upper arm of phase a, (b) $N_{\mathrm{sum}}^{\mathrm{discharge}}$ for SMs in the upper arm of phase a, (c) detection and localization flag for SMs in the upper arm of phase a, (d) $N_{\mathrm{sum}}^{\mathrm{charge}}$ for SMs in the upper arm of phase a, and (e) classification flag for SM_{ua1}.

SM faults. Moreover, it can only diagnose OC SM faults under NLM control. Additionally, this method utilizes several threshold values to diagnose OC SM faults without providing an analytical solution to their values. Therefore, designing these threshold values can become difficult under different MMC designs and ratings. The method proposed in [70] detects S_u failures in 12 ms, which is 2 ms longer than its diagnosis time for S_l failures. The method proposed in [79] provides more consistent diagnosis times of 11.9 ms and 11.8 ms for S_u and S_l failures. However, none of these methods can diagnose S_u&S_l failures.

4.5.6 Parametric Sensitivity to Parameter Changes

Fig. 4.11(a) shows v_{cua} with $C_{\text{SM}}^{\text{new}} = 0.8C_{\text{SM}}$ and $L_{\text{arm}}^{\text{new}} = 1.2L_{\text{arm}}$. Prior to $t = 100$ ms, the MMC is operating normally. At $t = 100$ ms, or the 6th fundamental period cycle, S_u and S_l failures occur in SM_{ua1}. This figure shows that v_{cua1} increases sharply at the onset of the fault. Fig. 4.11(b) shows $N_{\text{sum}}^{\text{discharge}}$ for SMs in the upper arm of phase a. This figure shows that $N_{\text{sum}}^{\text{discharge}}$ stays within normal bounds until the 7th fundamental period cycle, and becomes compromised afterwards. The proposed method, however, detects and localizes the fault in one fundamental period cycle, 16.67 ms, as shown in Fig. 4.11(c). Fig. 4.11(d) shows $N_{\text{sum}}^{\text{charge}}$ for SMs in the upper arm of phase a. This figure shows that $N_{\text{sum}}^{\text{charge}}$ stays within normal bounds until the 7th fundamental period cycle, and becomes compromised afterwards. The proposed method, however, classifies the fault type in one fundamental period cycle, 16.67 ms, as shown in Fig. 4.11(e).

Chapter 5

Fault-Tolerant Control of IBRs Under OC Faults

Immediately after the OC SM fault diagnosis, the MMC control system must enter the fault-tolerant (FT) mode of operation. Various methods are introduced in the literature to enable fault-tolerant (FT) operation of MMCs [81]–[87]. These methods can be categorized into two groups: hardware-based methods and software-based methods. Hardware-based methods incorporate redundant SMs in each phase, inserted in place of bypassed faulty SMs. However, most of these methods utilize redundant SMs with uncharged capacitors (cold SMs) [84]. Inserting cold SMs into the circuit causes transients and distortions in the output voltage. In addition, cold SMs reduce the semiconductor utilization factor of an MMC. Some redundancy-based methods use pre-charged (hot) SMs [85], [86]. Hot SMs are inserted into circuit even during the normal operation of MMCs. However, this results in increased switching and conduction losses. On the other hand, transient response of the output voltage is better and semiconductor uti-

Portions of this chapter are published as

[80] A. Mohammadhassani and A. Mehrizi-Sani, "Fast and fault-tolerant model predictive control of MMCs under selective harmonic elimination," IET Gener. Transm. Distrib., vol. 17, no. 1, pp. 240-251, Jan. 2023.

lization factor is higher. Despite their advantages, both redundancy-based methods have two drawbacks in common [87]: First, utilizing redundant SMs increases the cost and size of the converter. Second, FT operation of MMCs is achieved only when the number of redundant SMs is higher than the number of faulty SMs.

In contrast, software-based methods modify the modulation technique of an MMC to add FT capabilities to its operation. These methods are less common. References [81], [82] study modifying modulation techniques for FT operation of multicell converters. However, they do not maintain the harmonic performance. The merits of modifying space vector modulation (SVM) for FT operation of MMCs are explored in [83]. However, SVM design becomes very complicated when the number of voltage levels increases beyond three. In addition, this method does not use any circulating current controllers during FT mode, which adversely affects the harmonic performance of SVM. Reference [22] modifies the phase-shifted carrier modulation technique (PSC) to enable FT operation in MMCs. However, this method still uses redundant SMs. The method proposed in [88] maintains balance among line voltages by slightly increasing the capacitor voltages when the number of failed SMs is low. Otherwise, a zero-sequence voltage is injected to enable FT control. However, this method still uses redundant SMs and increases the ripple percentage in capacitor voltages. Moreover, it fails to maintain the output power of the MMC when there is a higher number of failed SMs. An FT control scheme for modular multilevel DC/DC converters is proposed in [89]. However, this method significantly increases the capacitor voltage ripples after SM failures and has a longer settling time. A DC bus voltage control-based method for FT operation of MMCs is proposed in [90]. However,

it only maximizes the line voltages and fails to maintain the MMC power supply. Additionally, the DC-link current ripple is increased. An FT control strategy is proposed for MMC-based static compensators (STATCOM) in [91]. However, redundant SMs are still in use. Moreover, it has a lower efficiency under FT operation with different power losses in each arm. Additionally, zero-sequence voltage is injected to balance the line voltages, which increases the capacitor voltage ripples.

A widely known modulation scheme is the selective harmonic elimination (SHE). In SHE, the switching angles are explicitly calculated to achieve the desired harmonic performance. This technique is commonly used in cascaded H-bridge inverters (CHB) [77], [92]. FT SHE methods are proposed in [93], [94] for CHBs. However, these methods only maximize the line voltages during faults. Moreover, these methods combine phase disposition and SHE to achieve their objectives, which makes the overall problem more complex. SHE is not widely employed in MMCs yet. This is because MMCs are commonly used in high-voltage applications, where the number of voltage levels is very high. For instance, an MMC requires 200–400 SMs per arm to reach ±400 kV (DC) in an HVDC system [95]. Therefore, the number of switching angles is also very high. This significantly complicates SHE; thus, other modulation techniques such as the nearest level modulation (NLM) are used for such applications. Simultaneously, MMCs are beginning to gain favor in applications such as medium-voltage microgrids [96], [97], where the number of SMs is less than 20 per arm. Thus, the advantages of SHE can be explored for MMCs in these applications [98], and FT SHE methods can be designed to increase the reliability of MMC operation [53]. On the other hand, the unequal and sometimes large difference between the switching

angles in SHE can cause large ripples in the circulating current in previously proposed circulating current controllers [99]–[101]. This may cause the circulating current controller to become unstable or create large disturbances in the output voltage. A method is proposed in [98] to limit the circulating current ripple by applying redundant switching states and using two upper and lower limits. However, this method has a slow response. Moreover, choosing the limits is an empirical process, which can become difficult under different MMC ratings. Therefore, a circulating current controller should also be designed to address the aforementioned challenges.

This chapter proposes an FT SHE-MPC strategy for MMCs. A procedure is proposed to properly design the FT SHE waveforms to preserve the harmonic performance of the faulty phase voltage and its fundamental component. An MPC-based controller is proposed to stabilize the operation of the MMC while implementing SHE during normal and FT operation. MPC is an effective strategy for multi-objective and nonlinear models [102], [103]. The proposed controller increases the capacitor voltages during FT operation to complete the transition into FT operation and maintain the fundamental component of the faulty phase voltage. To verify the performance of the proposed solution, a detailed model of an MMC with 4 SMs in each arm that is modeled in PSCAD/EMTDC software. Real-time results are also acquired using RTDS to confirm the results obtained using PSCAD/EMTDC.

The main contributions of this chapter are:

- FT SHE-PWM waveform design procedure.
- FT SHE-PWM mathematical derivation.
- MPC-based circulating current controller for normal and FT operation.

5.1 Proposed FT SHE Waveform Design Procedure

5.1.1 Overview of the $(2N+1)$-Level SHE

Fig. 5.1(a) shows the general $(2N+1)$-level phase output voltage waveform $V_{o,i}$ of an MMC with SHE. The waveform has quarter-wave symmetry. There are k switching angles in one quarter wave, which corresponds to k degrees of freedom. Due to quarter-wave symmetry, the Fourier series expansion of $V_{o,i}$ has only odd sine coefficients:

$$\begin{aligned} V_{o,i}(\omega_o t) &= \sum_{n=1,3,5,7,\ldots}^{\infty} b_n \sin(n\omega_o t) \\ b_n &= \frac{2V_c}{n\pi} \sum_{i=1}^{k} m_i \cos(n\alpha_i) \\ m_i &= \begin{cases} 1, & \text{Rising step} \\ -1, & \text{Falling step} \end{cases} \\ 0 < \alpha_1 <& \alpha_2 < \ldots < \alpha_{k-1} < \alpha_k < \frac{\pi}{2}, \end{aligned} \tag{5.1}$$

where ω_o is the fundamental frequency. The general $(2N+1)$-level SHE problem is defined in (5.2), which is solved offline to obtain switching angles for normal operation. This formulation can be solved using different methods, e.g., using Groebner bases and symmetrical polynomials [104] and virtual angles [98], which are verified on commercially available software packages such as Maple18, Mathematica, and MATLAB. The first equation corresponds to the fundamental component, and the remaining $k-1$ equations correspond to the low-order harmonics to be eliminated. Since a three-phase system is studied, triplen harmonics

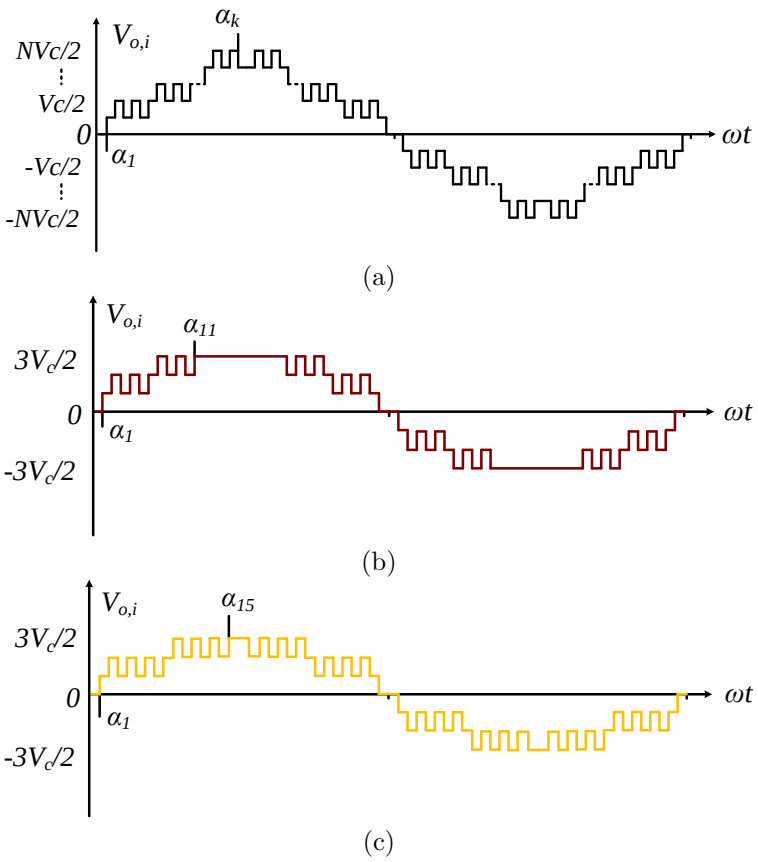

Figure 5.1: $V_{o,i}$ waveform during (a) normal operation, (b) an HBSM failure, and (c) FT operation when $M = 1$.

are canceled in line voltages and are not considered in this formulation.

$$\begin{cases} \dfrac{2V_{dc}}{\pi N}\displaystyle\sum_{i=1}^{k} m_i \cos(\alpha_i) = \dfrac{m_a V_{dc}}{2} \\ \dfrac{2V_{dc}}{5\pi N}\displaystyle\sum_{i=1}^{k} m_i \cos(5\alpha_i) = 0 \\ \dfrac{2V_{dc}}{7\pi N}\displaystyle\sum_{i=1}^{k} m_i \cos(7\alpha_i) = 0 \\ \quad\vdots \\ \dfrac{2V_{dc}}{l\pi N}\displaystyle\sum_{i=1}^{k} m_i \cos(l\alpha_i) = 0, \end{cases} \tag{5.2}$$

where $0 \leq m_a \leq 1$, and l is the highest harmonic to be eliminated.

5.1.2 Proposed FT SHE

To design the FT SHE method, the effect of bypassed HBSMs on $V_{o,i}$ is studied first. When one HBSM is bypassed in the upper and lower arms of one phase, the number of voltage levels in $V_{o,i}$ reduces to $2(N-1)+1 = 2N-1$. When $M < N$ HBSMs are bypassed in the upper and lower arms of one phase, the number of voltage levels in $V_{o,i}$ reduces to $2(N-M)+1$. This means that the maximum voltage available for the faulty phase reduces, which in turn makes the line voltages unbalanced and reduces the transferred power. Moreover, the harmonic performance of $V_{o,i}$ and power quality of the MMC deteriorate.

To address this issue, the number of switching angles in the corrupted $V_{o,i}$ waveform is increased so that the same number of harmonic components are eliminated as in the prefailure case and its fundamental component is preserved. The waveforms need to be designed for each value of M. The maximum value of M depends on the required level of redundancy. Hence, the more waveforms designed, the more fault-tolerant the converter becomes. However, this also increases the complexity of the controller and requires a larger memory.

As an example, consider the FT SHE waveform design procedure for a nine-level MMC with $N = 4$ and $M = 1$. The $V_{o,i}$ waveform for normal operation of this MMC has 15 switching angles in each quarter-wave. Therefore, 14 low-order harmonics can be eliminated while the fundamental component is controlled at its setpoint. When $M = 1$, the faulty HBSM and another HBSM in the opposite arm are bypassed. Hence, the faulty phase can no longer generate $\pm 2V_c$ voltage levels (highest levels). As shown in Fig. 5.1(b), the number of switching angles

Table 5.1: Solution Summary for the Proposed FT SHE during Normal Operation

Modulation Index M_a	$V_{o1}\%$	$V_{o5}\%$	$V_{o7}\%$	$V_{o11}\%$	$V_{o13}\%$	$V_{o17}\%$	$V_{o19}\%$	$V_{o23}\%$	$V_{o25}\%$	$V_{o29}\%$	$V_{o31}\%$	$V_{o33}\%$	$V_{o37}\%$	$V_{o39}\%$	$V_{o43}\%$	THD%
0.5	100.17	0.28	0.39	0.01	0.40	2.12	2.57	2.64	2.12	0.92	0.07	0.90	0.96	0.58	0.48	5.00
0.6	100.11	0.14	0.19	0.07	0.08	0.82	1.20	1.77	1.88	1.44	1.24	0.52	0.19	0.11	0.23	3.58
0.7	99.85	0.21	0.17	0.34	0.06	0.44	0.58	0.09	0.07	0.19	0.30	0.66	0.60	0.68	1.23	1.91
0.8	100.13	0.09	0.04	0.29	0.42	0.09	0.32	1.05	0.94	0.69	1.03	0.47	0.39	0.42	0.71	2.23
0.9	99.83	0.05	0.21	0.30	0.15	0.52	0.79	0.09	0.52	0.78	0.73	0.24	0.83	0.14	0.08	1.80
1	100.15	0.20	0.24	0.04	0.11	0.09	0.17	0.57	0.69	0.45	0.35	0.35	0.54	0.01	0.47	1.38

in one quarter-wave is reduced to 11, which degrades its harmonic performance. To design the FT $V_{o,i}$ waveform as discussed, additional switching angles are required to be added to the waveform. These switching angles can be arbitrarily placed in the waveform shown in Fig. 5.1(b) as long as its quarter-wave symmetry is maintained. Fig. 5.1(c) shows the designed FT $V_{o,i}$ waveform. The difference between the number of switching angles in the waveform shown in Figs. 5.1(b) and (c) is 4. Thus, by adding two extra voltage steps, the number of switching angles can return to 15, ensuring that the harmonic performance of $V_{o,i}$ is preserved. The switching angles for constructing the FT SHE waveforms and preserving the fundamental component of $V_{o,i}$ are found by solving (5.2) with N changed to $N - M = N - 1$ for the faulty phase.

Tables 5.1 and 5.2 show the SHE solution results using the method proposed in [77]. SHE solutions are available for $0.5 \leq M_a \leq 1$ during normal operation and for $0.7 \leq M_a \leq 1$ during FT operation. However, the solution range depends on the employed solver. The SHE solutions control the fundamental harmonic at its set point and control the low-order harmonics below 3% during both modes of operation. Additionally, the total harmonic distortion (THD) is less than or equal to 5% during both modes of operation. Therefore, the proposed FT SHE method complies with IEEE Standard 519 [105].

Fig. 5.2 summarizes the proposed design procedure for FT waveforms:

1. Design the $(2N + 1)$-level SHE waveforms according to Fig. 5.1(a).

Table 5.2: Solution Summary for the Proposed FT SHE during FT Operation

Modulation Index M_a	$V_{o1}\%$	$V_{o5}\%$	$V_{o7}\%$	$V_{o11}\%$	$V_{o13}\%$	$V_{o17}\%$	$V_{o19}\%$	$V_{o23}\%$	$V_{o25}\%$	$V_{o29}\%$	$V_{o31}\%$	$V_{o33}\%$	$V_{o37}\%$	$V_{o39}\%$	$V_{o43}\%$	THD%
0.7	100.04	0.03	0.36	0.24	0.50	0.37	0.22	0.92	0.51	0.68	0.17	0.42	0.65	0.42	1.53	2.31
0.8	100.13	0.09	0.60	0.65	0.22	0.18	0.72	0.15	1.72	0.42	0.05	0.38	0.96	0.80	1.44	2.88
0.9	100.08	0.03	0.04	0.07	0.04	0.13	0.06	0.03	0.04	0.10	0.06	0.09	0.12	0.10	0.14	0.31
1	99.90	0.05	0.01	0.00	0.09	0.20	0.32	0.18	0.30	0.36	0.28	0.54	0.23	0.06	0.26	0.95

2. Choose the maximum design value for M.

3. If the shortage of switching angles is an even number, add half as many voltage steps to the faulted waveform. Otherwise, find the closest largest even number and add half as many voltage steps to the faulted waveform.

4. Continue designing waveforms until the final value of M is reached.

5.2 Proposed MPC-Based Strategy for Circulating Current Control

Implementing SHE requires stable control of $i_{\text{diff,i}}$, $V^{\Sigma}_{cu,i}$, and $V^{\Sigma}_{cl,i}$ while generating the correct SHE waveform. This paper proposes an MPC-based $i_{\text{diff,i}}$ controller to stabilize the MMC during normal and FT operation and prevent distortion in the output voltage. The proposed controller receives the designed SHE waveforms, chooses the optimum $N_{u,i}$ and $N_{l,i}$, and balances $V^{\Sigma}_{cu,i}$ and $V^{\Sigma}_{cl,i}$ to control the output voltages. The proposed controller also increases V_c during FT operation to preserve the fundamental component of the faulty output voltage and balance the line voltages.

Fig. 5.3 shows the proposed controller. If $M = 0$, the controller operates in the normal mode. Otherwise, FT operation is activated. The proposed controller receives the reference SHE waveform $V^{*}_{o,i}$ and the sampled values of $i_{\text{diff,i}}$, $V^{\Sigma}_{cu,i}$, and $V^{\Sigma}_{cl,i}$ to predict their next sampled values using forward Euler's method. This

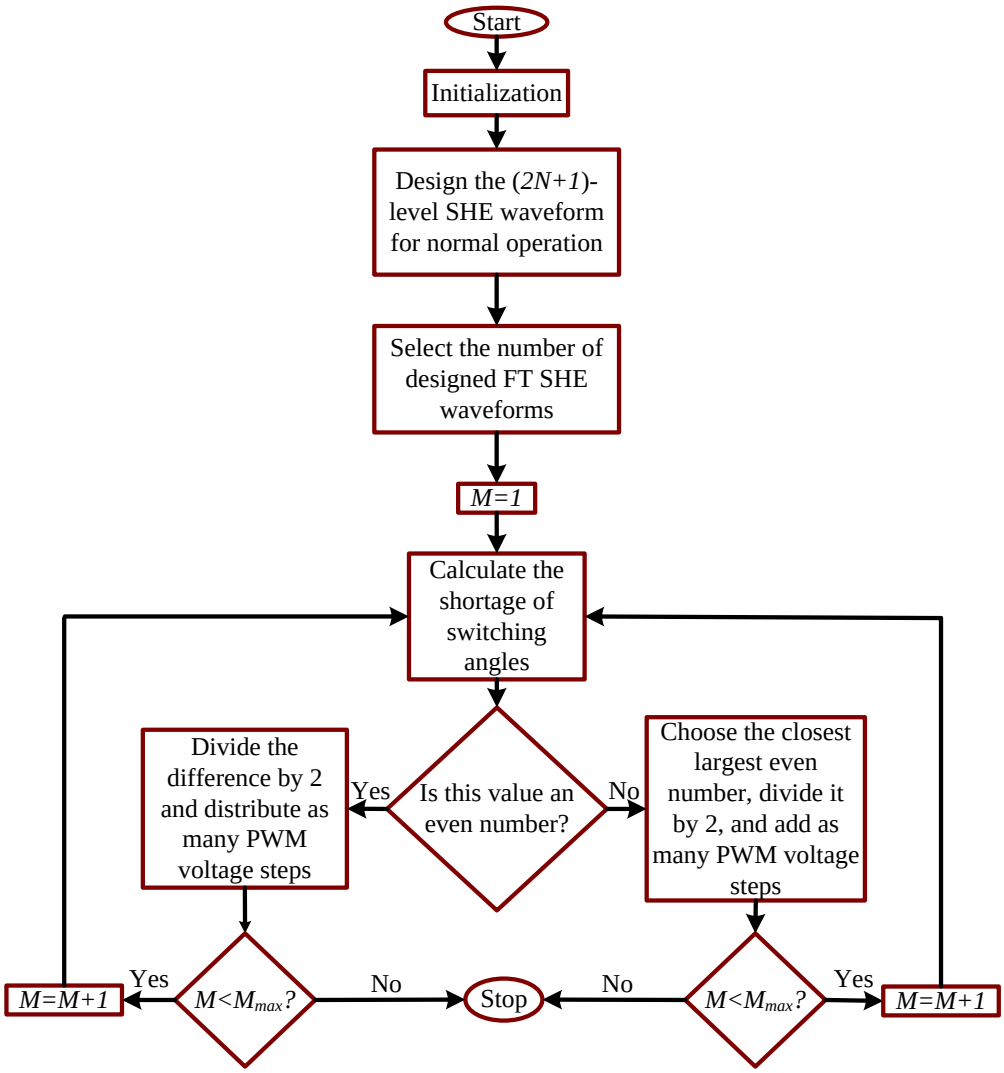

Figure 5.2: Proposed process for designing the FT SHE waveforms.

is done through a discrete form of (4.10) with a sampling period of T_s

$$\begin{cases} i_{\text{diff,i}}((n+1)T_s) = a_1 V_{\text{diff,i}}(nT_s) + a_2 i_{\text{diff,i}}(nT_s) \\ V^{\Sigma}_{cu,i}((n+1)T_s) = a_3 i_{u,i}(nT_s) + V^{\Sigma}_{cu,i}(nT_s) \\ V^{\Sigma}_{cl,i}((n+1)T_s) = a_4 i_{l,i}(nT_s) + V^{\Sigma}_{cl,i}(nT_s), \end{cases} \tag{5.3}$$

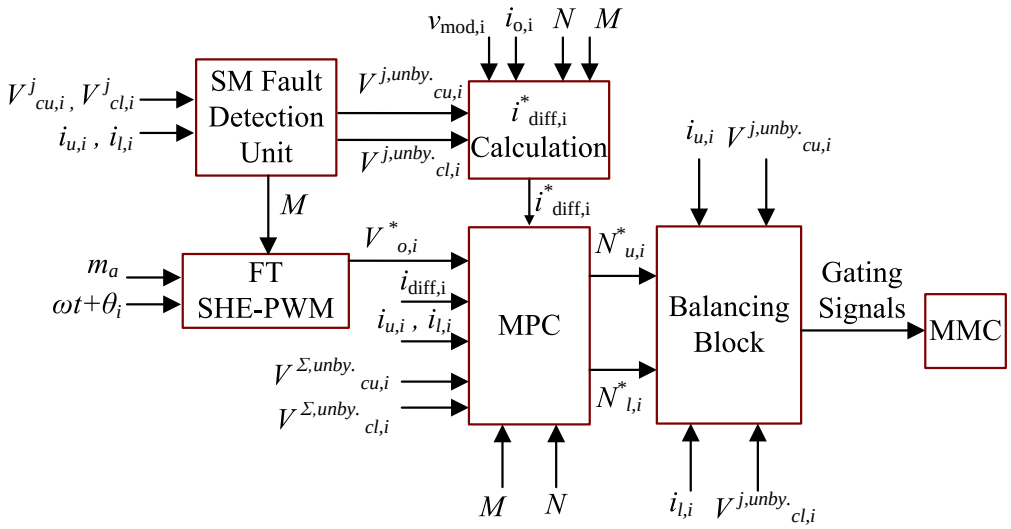

Figure 5.3: Proposed MPC-based circulating current controller.

where

$$\begin{cases} a_1 = \dfrac{T_s}{2L_{\text{arm}}}, \;\; a_2 = 1 - \dfrac{T_s R_{\text{arm}}}{L_{\text{arm}}} \\ a_3 = \dfrac{T_s(N-M)N_{u,i}}{C_{\text{SM}}} \\ a_4 = \dfrac{T_s(N-M)N_{l,i}}{C_{\text{SM}}}. \end{cases} \tag{5.4}$$

$N_{u,i}$ and $N_{l,i}$ are defined as

$$N_{u,i}, N_{l,i} \in \{0, \frac{1}{N-M}, \frac{2}{N-M}, \ldots, 1\}. \tag{5.5}$$

Equation (5.5) defines a limited set. The optimum $N_{u,i}$ and $N_{l,i}$ that minimize the cost function defined in (5.6) are chosen and fed to the balancing block. This block determines which HBSMs to insert or bypass according to their V_c values and arm current directions. Using the method proposed in [98], the switching frequency of the proposed method is set to that by the SHE block. However, MPC controls $i_{\text{diff,i}}$ by determining $N_{u,i}$ and $N_{l,i}$. Therefore, it adds extra switchings

to properly control the MMC.

$$\text{Cost} = \sigma \| X\left((n+1)\,T_s\right) - X^*\left((n+1)\,T_s\right) \|_2^2, \tag{5.6}$$

where σ is vector containing the weight factors, X is the state vector, X^* is the reference state vector, and $\|\cdot\|_2$ is the Euclidean norm. The weighting factors are determined using the per-unit conversion method in [106] to set $i_{\text{diff,i}}$ as the main control objective while setting the relative importance of $V_{cu,i}^{\Sigma}$ and $V_{cl,i}^{\Sigma}$. In contrast to the SHE-MPC strategy in [101], the proposed MPC method does not treat the SHE waveform as an input to the MPC cost function. Instead, it predicts the state variables for each voltage level in the reference SHE waveform and chooses the optimum $N_{u,i}$ and $N_{l,i}$ to tighten control on the output voltage and ensure fast and stable control of circulating currents. To maintain energy balance between the DC and AC sides and balance the energy through phase arms, the method proposed in [107], also shown in Fig. 5.4, is used to generate i_{diff}^* based on the instantaneous information of the MMC, including the instantaneous values of sum of capacitor voltages and the output current.

If an HBSM fails, the proposed controller increases the V_c values by the amount defined in (5.7) to complete the transition to FT operation. To maintain $V_{cu,i}^{\Sigma}$ and $V_{cl,i}^{\Sigma}$ at V_{dc} after M HBSM failures, V_c should be increased to $V_{dc}/(N-M)$ requiring larger capacitors. However, as N increases, the increase in capacitor voltages ΔV_c during HBSM failures decreases:

$$\Delta V_c = \frac{M V_{dc}}{N(N-M)}. \tag{5.7}$$

Even though this method requires overdesign, it is less costly than conventional

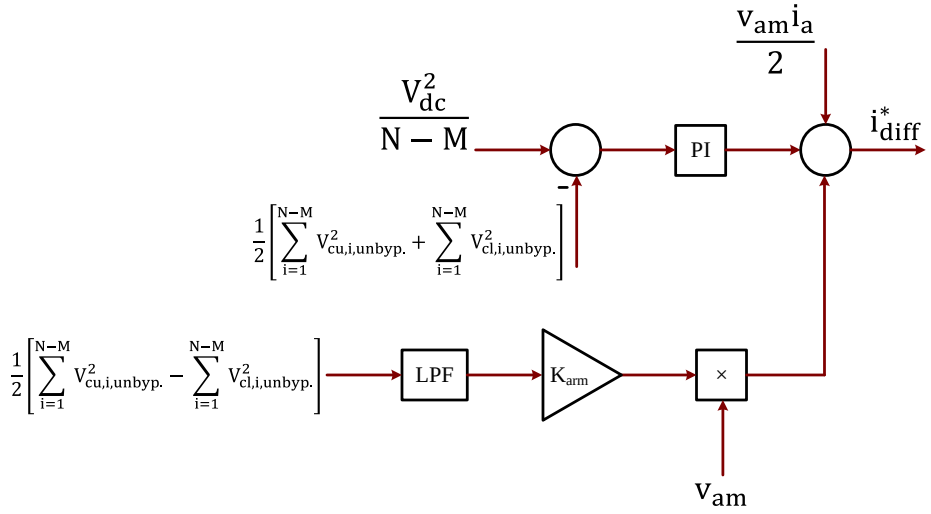

Figure 5.4: Control loop for generating i^*_{diff}.

redundancy-based methods, which add extra HBSMs [83].

To better illustrate the proposed control strategy, consider a single-phase MMC with $N = 2$. The proposed SHE-MPC strategy generates the designed output voltage waveform while simultaneously maintaining the capacitor voltages at $V_{dc}/2$ and controlling the circulating currents. To achieve these objectives during normal operation, the proposed controller selects the optimal insertion index from the set below for each output voltage level.

$$N_{u,i}, N_{l,i} \in \{0, \frac{1}{2}, 1\}. \tag{5.8}$$

In case of a single HBSM failure, the proposed strategy bypasses the failed HBSM and its corresponding HBSM in the opposite arm. Therefore, the available insertion indices are changed to

$$N_{u,i}, N_{l,i} \in \{0, 1\}. \tag{5.9}$$

The proposed SHE-MPC applies the new optimal insertion indices to increase the capacitor voltages to V_{dc}, control the circulating currents, and generate the FT SHE output voltage waveform. Therefore, it maintains the fundamental harmonic of the output voltage and preserves its harmonic quality.

5.3 Performance Evaluation: Offline

5.3.1 Steady-State Performance

Fig. 5.5(a) shows the capacitor voltages of phase a. The proposed method successfully controls the capacitor voltages at 2.72 kV with a ripple of 4.89%. Fig. 5.5(b) shows $i_{\text{diff,a}}$; it correctly follows its reference with a maximum of 106.1 A. Fig. 5.5(c) shows the output currents. The proposed method generates balanced three-phase output currents with a peak magnitude of 335.3 A. Fig. 5.5(d) shows the output voltages. The proposed method generates balanced three-phase output voltages with a peak magnitude of 4 kV. Fig. 5.5(e) shows the harmonic spectrum of the output voltages: the peak value of the fundamental component is 4 kV, and the low-order harmonics are eliminated.

5.3.2 Response to Change in m_a

This section evaluates the response of the proposed method to a step change in m_a during normal operation. Fig. 5.6(a) shows the capacitor voltages of phase a. At $t = 50$ ms, m_a increases in a step from 0.8 to 1. After a small transient with an overshoot to 2.87 kV, the capacitor voltages stabilize at 2.72 kV with a ripple of 5.03%. The settling time of capacitor voltages is 50 ms, which is almost half of that for the method proposed in [98]. Fig. 5.6(b) shows $i_{\text{diff,a}}$. At $t = 50$ ms, m_a increases in a step from 0.8 to 1. $i_{\text{diff,a}}$ successfully follows its new

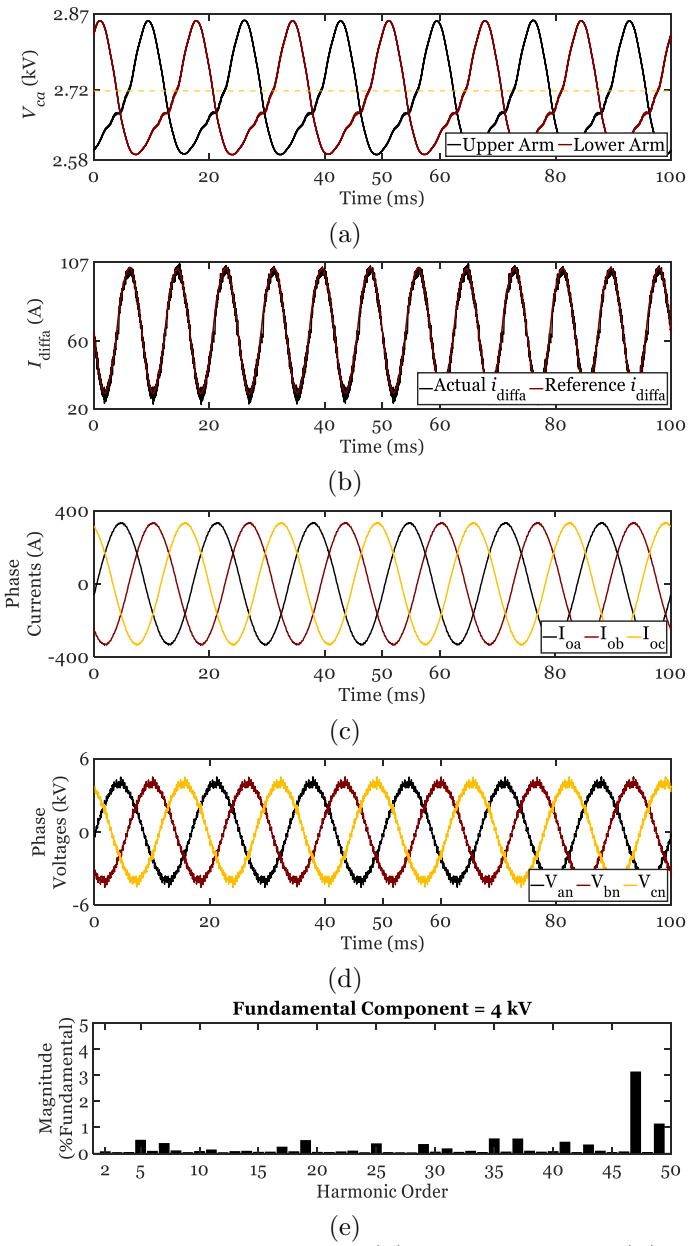

Figure 5.5: Steady-state simulation results for (a) $v^a_{cu,j}$ and $v^a_{cl,j}$, (b) $i_{\text{diff,a}}$, (c) $i_{o,i}$, (d) $V_{o,i}$, and (e) harmonic spectrum of $V_{o,i}$.

reference, increasing its maximum to 156.3 A. The settling time for the circulating current is 20 ms, which is almost one-fifth of that for the method proposed in [98]. Fig. 5.6(c) shows the output currents. The proposed method successfully generates balanced three-phase output currents and increases their peak magnitude to 413.8 A. Fig. 5.6(d) shows the output voltages. The proposed method

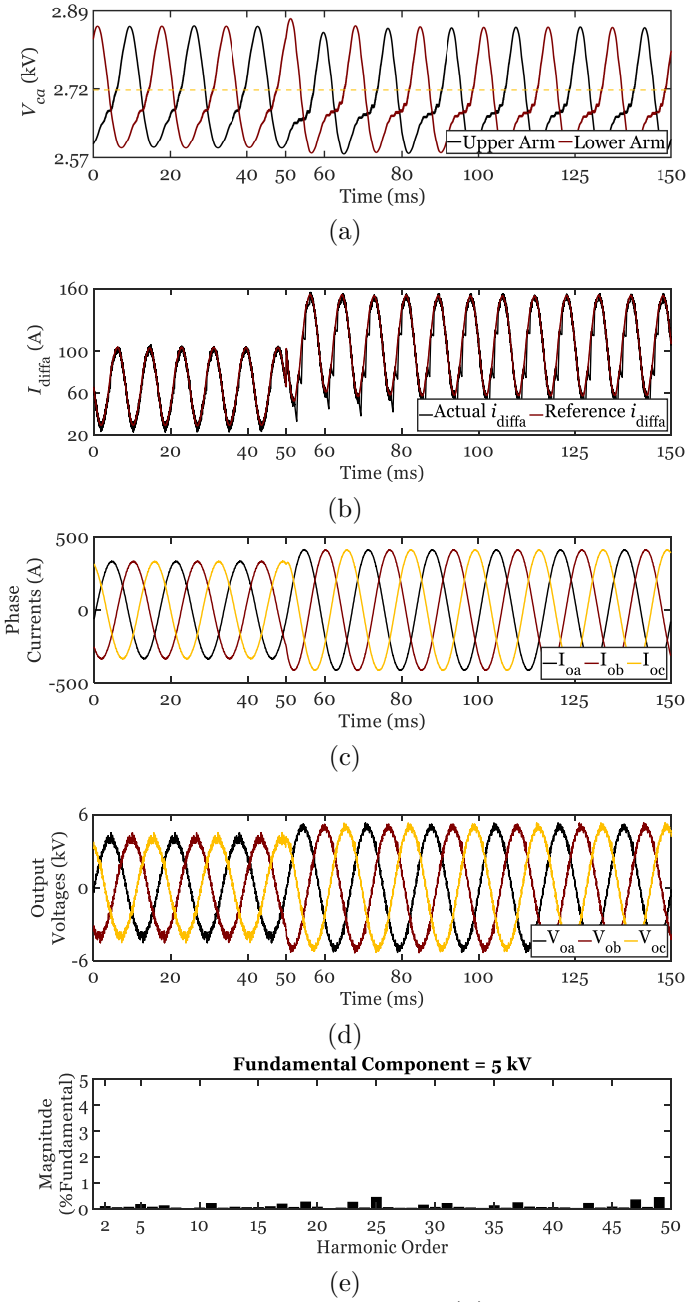

Figure 5.6: Simulation results for step change in m_a: (a) $v^a_{cu,j}$ and $v^a_{cl,j}$, (b) $i_{\text{diff,a}}$, (c) $i_{o,i}$, (d) $V_{o,i}$, and (e) harmonic spectrum of $V_{o,i}$ with $m_a = 1$.

successfully generates balanced three-phase output voltages and increases their peak magnitude to 5 kV. Fig. 5.6(e) shows the harmonic spectrum of the output voltages. The peak value of the fundamental component is increased to 5 kV while eliminating the low-order harmonics.

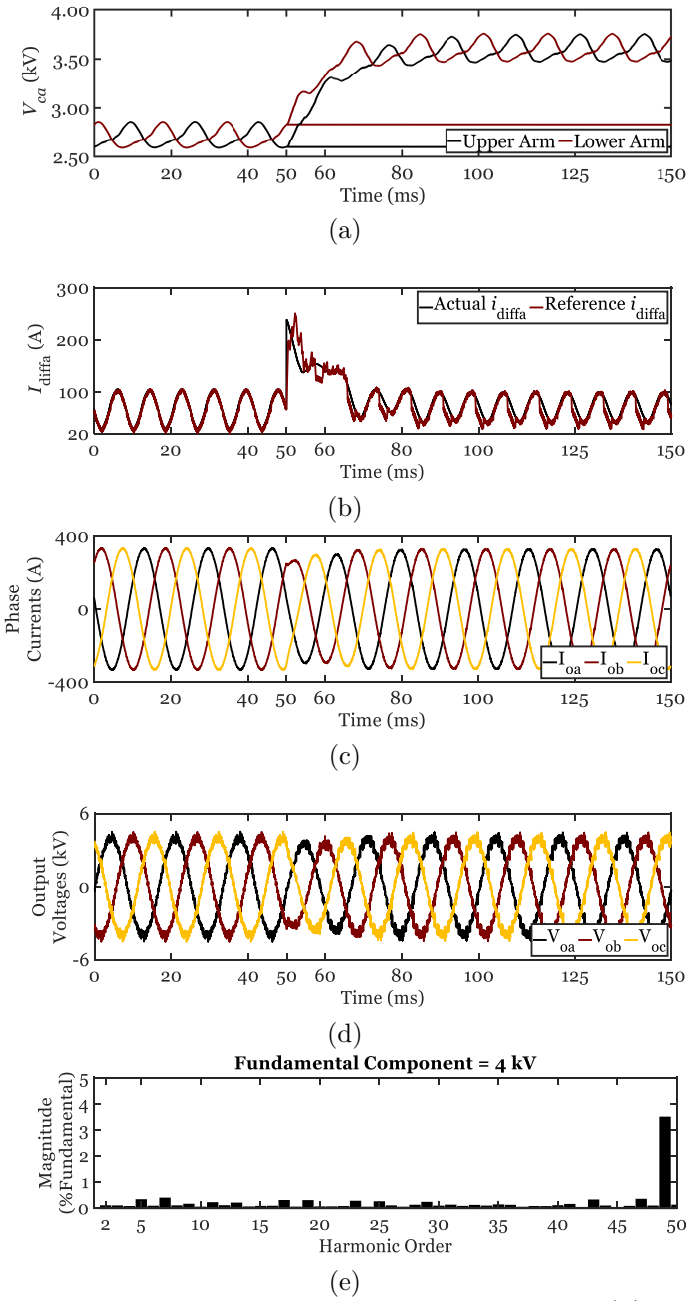

Figure 5.7: Simulation results after an HBSM failure in phase a: (a) $v^a_{cu,j}$ and $v^a_{cl,j}$, (b) $i_{\text{diff,a}}$, (c) $i_{o,i}$, (d) $V_{o,i}$, and (e) harmonic spectrum of $V_{o,a}$.

5.3.3 Response to HBSM Failures

This case study evaluates the performance of the proposed method under HBSM failures. Fig. 5.7(a) shows the capacitor voltages of phase a. At $t = 50$ ms, SM_{u1a}

and SM_{l1a} are bypassed and FT operation is established. The proposed method stabilizes the remaining capacitor voltages at 3.62 kV with a ripple of 3.85% at $t = 126.43$ ms. Fig. 5.7(b) shows $i_{\text{diff,a}}$; it stabilizes with a maximum of 99.8 A at $t = 126.43$ ms and an overshoot to 248.6 A. The settling time of capacitor voltages and circulating current is 76.43 ms, which is significantly faster than the method proposed in [108] which takes 428.8 ms to establish FT operation. Fig. 5.7(c) shows the output currents. The proposed method generates balanced three-phase output currents and keeps their peak magnitude constant. Fig. 5.7(d) shows the output voltages. The proposed method generates balanced three-phase output voltages with modified waveforms. Fig. 5.7(e) shows the harmonic spectrum of output voltages during FT operation; the low-order harmonics are still eliminated and the peak value of the fundamental component is preserved.

5.4 Performance Evaluation: Real-Time

This section evaluates the performance of the proposed method in real-time to validate the results of Section 4.5. The MMC system is modeled on an RTDS NovaCor chassis with one core. It is modeled in the substep environment using the CHAINV5 model. This model uses a surrogate circuit to model each HBSM. The surrogate circuit consists of an upward diode, a capacitor, and a discharge resistor in parallel. In an electromagnetic transient simulation, HBSM capacitor branches are modeled with a resistance and a Thevenin history voltage source (V_{hc}). Alternating calculations of the HBSM capacitor voltage and V_{hc} occur during each time step. In addition, the MMC model in RTDS includes DC-link resistances, but not the parallel bypass switches. Instead, the bottom switch of the faulty HBSM is turned on to bypass that HBSM.

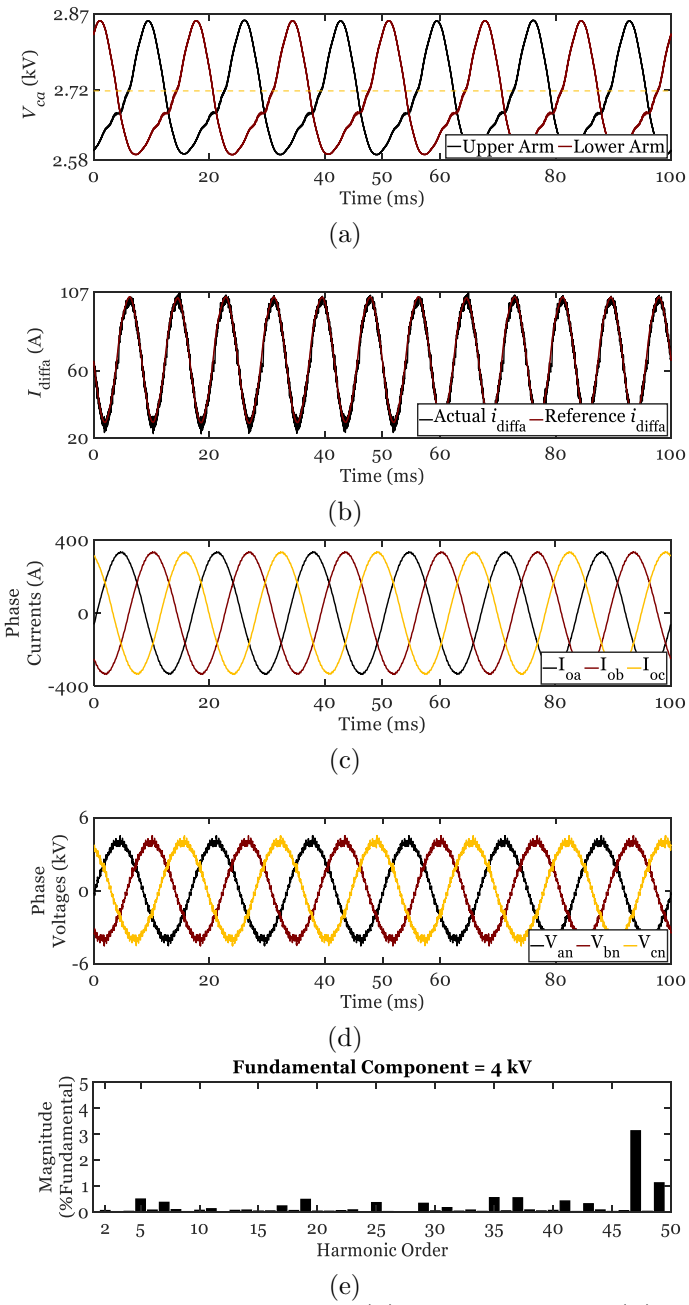

Figure 5.8: Real-time steady-state results for (a) $v^a_{cu,j}$ and $v^a_{cl,j}$, (b) $i_{\text{diff,a}}$, (c) $i_{o,i}$, (d) $V_{o,i}$, and (e) harmonic spectrum of $V_{o,a}$ during normal operation.

5.4.1 Steady-State Performance

This section evaluates the steady-state performance of the proposed method in real time. Fig. 5.8(a) shows the real-time steady-state results for capacitor

voltages of phase a during normal operation. The proposed method successfully stabilizes the capacitor voltages at 2.72 kV with a ripple of 4.87%. Therefore, real-time and offline capacitor voltage results are similar. Fig. 5.8(b) shows the real-time steady-state results for $i_{\text{diff,a}}$ during normal operation. It follows its reference and has a maximum of 108.6 A. Real-time and offline results for $i_{\text{diff,a}}$ are similar. Fig. 5.8(c) shows the output currents. The proposed method generates balanced three-phase output currents with a peak magnitude of 333.2 A. Therefore, real-time and offline results are similar. Fig. 5.8(d) shows $V_{o,i}$. The proposed method generates balanced three-phase output voltages with a peak magnitude of 4 kV, similar to offline results. Fig. 5.8(e) shows the harmonic spectrum of $V_{o,i}$. The peak value of the fundamental component is 4 kV, and the low-order harmonics are eliminated, similar to offline results.

5.4.2 Response to HBSM Failures

This section evaluates the performance of the proposed method under HBSM failures in real time. At $t = 50$ ms, SM_{u1a} and SM_{l1a} are bypassed and FT operation is established. Fig. 5.9(a) shows the capacitor voltages of phase a. The proposed method stabilizes the remaining capacitor voltages at 3.62 kV with a ripple of 3.81% at $t = 126.43$ ms, similar to their offline response. Fig. 5.9(b) shows $i_{\text{diff,a}}$; it stabilizes with a maximum of 103.4 A at $t = 126.43$ ms and an overshoot to 243.8 A, similar to the offline results. Fig. 5.9(c) shows the output currents. The proposed method generates balanced three-phase output currents and keeps their peak magnitude constant. Fig. 5.9(d) shows the real-time results for $V_{o,i}$ during FT operation. The proposed method generates balanced three-phase output voltages with a peak magnitude of 4 kV during FT operation and changes their waveforms. Fig. 5.9(e) shows the harmonic spectrum for real-time output

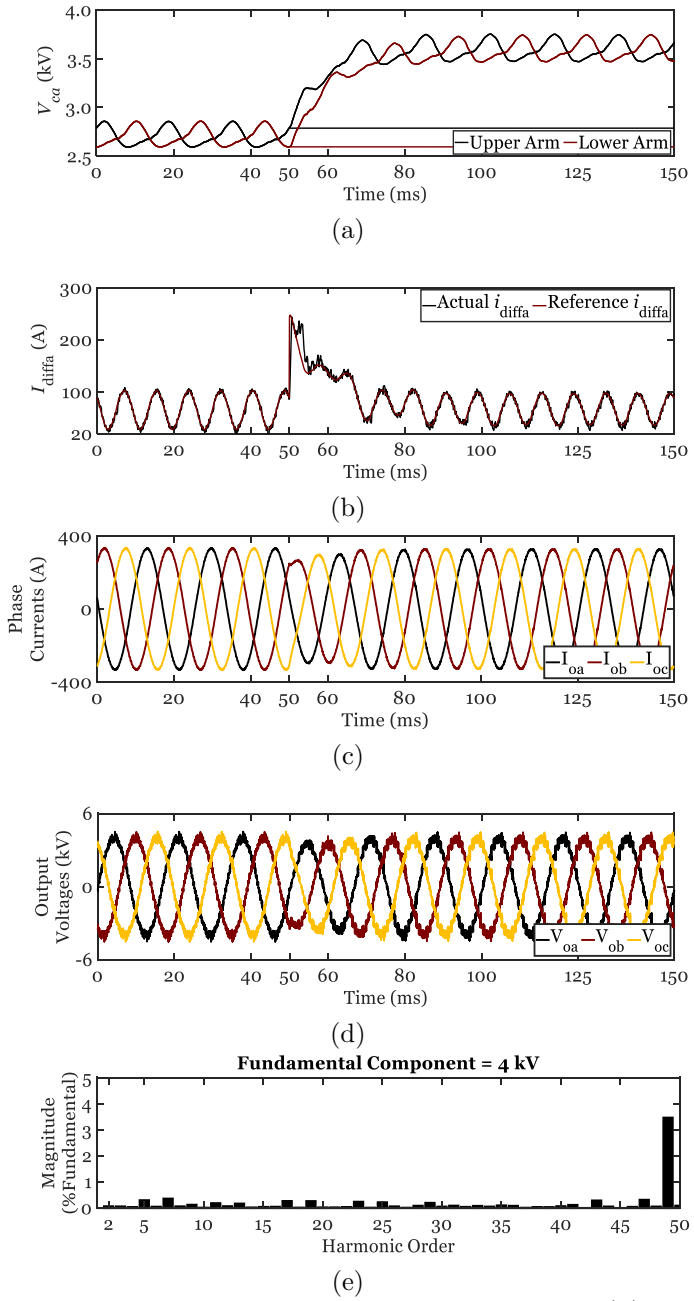

Figure 5.9: Real-time results after an HBSM failure in phase a: (a) $v^a_{cu,j}$ and $v^a_{cl,j}$, (b) $i_{\text{diff,a}}$, (c) $i_{o,i}$, (d) $V_{o,i}$, and (e) harmonic spectrum of $V_{o,a}$ during FT operation.

voltages during FT operation. The low-order harmonics are eliminated, and the fundamental component is preserved. Therefore, the harmonic performance of real-time and offline output voltages are similar.

Table 5.3: Performance Comparison with Recently Proposed Methods

Method	Capacitor Voltage Ripple		Transition Time
	Normal Operation	FT Operation	
Proposed	4.89%	3.85%	76.43 ms
[4]	10%	13%	428.8 ms
[12]	13.33%	10.69%	230 ms
[13]	4%	4%	200 ms
[14]	2.80%	2%	130 ms

5.4.3 Performance Comparison

Table 5.3 summarizes the performance of the proposed method in comparison with some of the most recently proposed methods. The proposed method has the lowest transition time into FT operation. Additionally, it has a lower capacitor voltage ripple percentage than the methods proposed in [108] and [88]. The methods proposed in [89] and [90] have a smaller capacitor voltage ripple percentage than the proposed method. However, this difference is very small.

Chapter 6

Conclusions

6.1 Summary

This dissertation proposes solutions to four distinct problems to solve the issues of protection and cybersecurity in inverter-based microgrids:

1. A signal reconstruction module based on autocorrelation and cross-correlation that makes IBRs and the microgrid resilient to FDI attacks on the tracking errors communicated between IBRs for the purpose of distributed set point modulation;
2. A fast and reliable nonpilot directional protection scheme that detects and isolates system faults by interpreting measured current harmonic patterns using SVM;
3. A fast and reliable MMC protection scheme that diagnoses OC SM faults using SVM by acting upon the measured capacitor voltage charging and discharging patterns; and
4. A fast SHE-MPC strategy to enable seamless transition of IBRs into the FT mode of operation.

Although these four solutions address different issues in an inverter-based microgrid, their ultimate aim is to maintain normal operation of the microgrid against disturbances.

Several test systems, ranging from a detailed MMC model to small and large microgrids, are employed to evaluate the performance of the proposed solutions. Performance evaluation of the proposed solutions are conducted in PSCAD/EMTDC and MATLAB software packages, with algorithms implemented using Fortran, MATLAB, and Python.

6.2 Conclusions

Inverter-based microgrids using distributed control face serious cybersecurity challenges, especially against FDI attacks. Additionally, protecting an inverter-based microgrid against system faults is very challenging as IBRs exhibit limited fault current levels as well as an unconventional response to faults. Moreover, IBRs should be protected from faults on their power electronic devices to prevent them from shutting down or having an adverse impact on microgrid control. This dissertation addresses these challenges via three distinct solutions.

The main conclusions of this dissertation are as follows.

- A distributed implementation of SPM, i.e., CSPM, is required due to the inefficiencies of centralized control. Cybersecurity challenges in CSPM, especially against FDI attacks, are mitigated using the proposed signal reconstruction module. The proposed cybersecure CSPM strategy is able to significantly reduce the amount of injected noise into the IBR measurements and prevent IBRs and microgrids from becoming unstable.
- Protecting microgrids from system faults is challenging and requires revised thinking to propose novel schemes. Relying on different polarization quantities such as harmonic currents provides better security in terms of coordination.

Using SVM as a decision maker to develop a nonpilot directional scheme provides sensitivity and selectivity.

- Utilizing the charge and discharge patterns of capacitor voltages in MMCs to detect OC faults can result in a fast and reliable diagnosis algorithm. This algorithm is also agnostic to changes in MMC circuit parameters.
- Properly distributing the burden of a lost SM across the remaining SMs can avoid the need for redundant SMs in an MMC and prevent its size and cost from growing. Additionally, generating the circulating current reference in relationship to capacitor voltages and output current enables the stable control of circulating currents in MMCs operating under the SHE regime.

The performance requirements of the proposed solution for GFM IBRs are as below:

1. GFM IBRs should have the communication capability to implement CSPM in real-time. This capability should span across all control levels;
2. GFM IBRs should have the computational capability to implement SDP in real-time for stable and effective performance of the proposed signal reconstruction module. The solver speed of SDP can be increased by properly configuring its settings. These settings include but are not limited to input size, sampling frequency, warm start, and acceleration;
3. GFM IBRs should have the capability to inject harmonic currents during faults while adhering to the grid code. Moreover, GFM IBRs should stop injecting harmonics immediately after the fault is cleared and return to normal operation without creating large-scale disturbances;
4. GFM IBRs should have the capability to ride through IGBT switch faults by

equally distributing the lost contribution of the bypassed faulty SMs across the remaining healthy SMs. Oversizing the SM elements such as capacitor banks and IGBTs may be required but can be minimized by achieving tradeoff between the number of SMs and the required amount of redundancy.

6.3 Contributions

The contributions of this dissertation are as below.

- This dissertation contributes to solving cybersecurity issues in the distributed control of microgrids by proposing and evaluating a signal-reconstruction module by relying on autocorrelation and cross-correlation measurements and using SDP that makes distributed control more resilient to potential FDI attacks.
- This dissertation proposes and evaluates a system protection scheme that uses SVM to interpret harmonic currents injected by IBRs to detect and isolate system faults and enable reliable protection coordination.
- This dissertation proposes an OC SM fault diagnosis scheme that uses SVM to diagnose capacitor voltage charge and discharge patterns to detect, localize, and classify such faults in only 16.67 ms.
- This dissertation proposes an SHE-MPC strategy to enable seamless transition of IBRs into the FT mode of operation while properly controlling their operation.

6.4 Future Work

A few suggested areas for future work are provided below:

- Currently, the real-time operation of the proposed SDP-based signal reconstruction method is provided for slower control levels, such as secondary and tertiary controls. The SDP solver algorithm can be further enhanced to be applicable to primary control as well.

- In the proposed SVM-based system protection scheme, it is assumed that all IBRs are operating in the GFM mode. However, this may not always be the case as some IBRs may operate in the GFL mode. The effects of variation in the output power of GFL units on harmonic injection and the performance of the proposed method should be studied. The proposed method should also be evaluated under high-impedance faults.

- The proposed OC SM fault diagnosis method may become computationally restrictive for MMCs with large number of SMs. Therefore, a future area of research on this topic is to design a simplified training process for the employed SVMs. Another future prospect of this topic is to further increase the accuracy of the classification SVM. Although the presence of this SVM is not critical, an accurate classification of the OC SM fault can provide useful information to the maintenance crew. Finally, the proposed method diagnoses OC SM fault in 16.67 ms. This can be further reduced to make the proposed solution more comparable with hardware-based methods.

- The proposed FT SHE-MPC adds significant stability to controlling the circulating currents when an MMC is operating using SHE. However, the circulating current ripples can be reduced. Moreover, the overshoot in circulating currents can be further reduced during after an OC SM failure.

6.5 Publications

6.5.1 Journal Articles

1. A. Mohammadhassani and A. Mehrizi-Sani, "Nonpilot directional protection of a microgrid," *IET Gener. Transm. Distrib.*, Apr. 2023, under review (Publication ID: GTD-2023-04-0319).

2. B. Choudhury, A. Mohammadhassani, B. Alexander, R. Iyer, A. Mehrizi-Sani, V. K. Shah, and J. H. Reed, "Control coordination in inverter-Based microgrids using AoI-based 5G schedulers," *IET Smart Grid*, Mar. 2023, under review (Publication ID: STG-2023-03-0024).

3. A. Mohammadhassani and A. Mehrizi-Sani, "Fast and fault-tolerant model predictive control of MMCs under selective harmonic elimination," *IET Gener. Transm. Distrib.*, vol. 17, no. 1, pp. 240-251, Jan. 2023.

4. A. Mohammadhassani and A. Mehrizi-Sani, "Open-circuit submodule fault diagnosis in MMCs using support vector machines," *IET Gener. Transm. Distrib.*, vol. 16, no. 24, pp. 5015-5025, Dec. 2022.

6.5.2 Conference Papers

1. B. Alexander, A. Mohammadhassani and A. Mehrizi-Sani, "Resilient power sharing in 100% inverter-based power systems under GPS spoofing attacks ," *IEEE Power Energy Soc. General Meeting (PESGM)*, Feb. 2023.

2. A. Mohammadhassani, Y. Akbar, A. Mehrizi-Sani, and H. Wang, "Cyber vulnerability assessment of microgrids with 5G-enabled distributed control," *IEEE Power Energy Soc. General Meeting (PESGM)*, Oct. 2022.

3. S. Venkatachari, A. Mohammadhassani, and A. Mehrizi-Sani, "Submodule fault detection in MMCs using support vector classification," *IEEE Power Energy Soc. Innov. Smart Grid Tech. Conf. Europe (ISGT Europe)*, Dec. 2021.

4. A. Mohammadhassani, A. Mehrizi-Sani, and K. Saleh, "Fault current directionality in islanded microgrids using SVM and synthetic harmonic injection," *IEEE Intl. Symp. Ind. Electron.*, Nov. 2021.

5. A. Mohammadhassani, N. Skoff, and A. Mehrizi-Sani, "Performance analysis of distance protection in presence of Type III wind turbine generators," *IEEE Innov. Smart Grid Tech. Conf. (ISGT)*, Mar. 2021.

6. A. Mohammadhassani, A. Teymouri, A. Mehrizi-Sani, and K. Tehrani, "Performance evaluation of a microgrid under cyberattacks," *IEEE Intl. Conf. Syst. Syst. Eng. (SoSE)*, Jul. 2020.

7. A. Mohammadhassani and A. Mehrizi-Sani, "A fault-tolerant selective harmonic elimination method for modular multilevel converters," *IEEE Power Energy Soc. General Meeting (PESGM)*, Dec. 2020.

Bibliography

[1] H. Saadat, *Power System Analysis Third Edition*. PSA Publishing LLC, 2011.

[2] B. Kroposki, B. Johnson, Y. Zhang, V. Gevorgian, P. Denholm, B.-M. Hodge, and B. Hannegan, "Achieving a 100% renewable grid: Operating electric power systems with extremely high levels of variable renewable energy," *IEEE Power Energy Mag.*, vol. 15, no. 2, pp. 61–73, Mar. 2017.

[3] A. Hoke, V. Gevorgian, S. Shah, P. Koralewicz, R. W. Kenyon, and B. Kroposki, "Island power systems with high levels of inverter-based resources: Stability and reliability challenges," *IEEE Electrific. Mag.*, vol. 9, no. 1, pp. 74–91, Mar. 2021.

[4] M. Yazdanian and A. Mehrizi-Sani, "Internal model-based current control of the RL filter-based voltage-sourced converter," *IEEE Trans. Energy Convers.*, vol. 29, no. 4, pp. 873–881, Dec. 2014.

[5] S. Leitner, M. Yazdanian, S. Ziaeinejad, A. Mehrizi-Sani, and A. Muetze, "Internal model-based active resonance damping current control of a grid-connected voltage-sourced converter with an LCL filter," *IEEE Trans. Power Syst.*, vol. 33, no. 6, pp. 6025–6036, Nov. 2018.

[6] R. H. Lasseter, Z. Chen, and D. Pattabiraman, "Grid-forming inverters: A critical asset for the power grid," *IEEE Trans. Emerg. Sel. Topics Power Electron.*, vol. 8, no. 2, pp. 925–935, Jun. 2020.

[7] J. Matevosyan, B. Badrzadeh, T. Prevost, E. Quitmann, D. Ramasubramanian, H. Urdal, S. Achilles, J. MacDowell, S. Hsien Huang, V. Vital,

J. OSullivan, and R. Quint, "Grid-forming inverters: Are they the key for high renewable penetration?" *IEEE Power Energy Mag.*, vol. 21, no. 2, pp. 77–86, Mar. 2023.

[8] T. Kim, N. G. Barry, W. Kim, S. Santoso, W. Wang, R. C. Dugan, and D. Ramasubramanian, "Voltage balancing capability of grid-forming inverters," *IEEE Open Access J. Power Energy*, vol. 9, pp. 479–488, Oct. 2022.

[9] M. Lu, "Virtual oscillator grid-forming inverters: State of the art, modeling, and stability," *IEEE Trans. Power Electron.*, vol. 37, no. 10, pp. 11 579–11 591, Oct. 2022.

[10] S. Geng and I. A. Hiskens, "Unified grid-forming/following inverter control," *IEEE Open Access J. Power Energy*, vol. 9, pp. 489–500, Oct. 2022.

[11] T. Liu and X. Wang, "Unified voltage control for grid-forming inverters," *IEEE Trans. Ind. Electron.*, Apr. 2023, accepted for publication.

[12] N. Hatziargyriou, *Microgrids: Architectures and Control*. Wiley-IEEE Press, 2014, ch. 1, pp. 1–24.

[13] D. E. Olivares, A. Mehrizi-Sani, A. H. Etemadi, C. A. Cañizares, R. Iravani, M. Kazerani, A. H. Hajimiragha, O. Gomis-Bellmunt, M. Saeedifard, R. Palma-Behnke, G. A. Jiménez-Estévez, and N. D. Hatziargyriou, "Trends in microgrid control," *IEEE Trans. Smart Grid*, vol. 5, no. 4, pp. 1905–1919, Jul. 2014.

[14] F. Mohammadi, B. Mohammadi-Ivatloo, G. B. Gharehpetian, M. H. Ali, W. Wei, O. Erdinç, and M. Shirkhani, "Robust control strategies for microgrids: A review," *IEEE Syst. J.*, vol. 16, no. 2, pp. 2401–2412, Jun. 2022.

[15] A. Hooshyar and R. Iravani, "Microgrid protection," *Proc. IEEE*, vol. 105, no. 7, pp. 1332–1353, Jul. 2017.

[16] M. A. Perez, S. Bernet, J. Rodriguez, S. Kouro, and R. Lizana, "Circuit topologies, modeling, control schemes, and applications of modular multilevel converters," *IEEE Trans. Power Electron.*, vol. 30, no. 1, pp. 4–17, Jan. 2015.

[17] Z. Li, M. Shahidehpour, and F. Aminifar, "Cybersecurity in distributed power systems," *Proc. IEEE*, vol. 105, no. 7, pp. 1367–1388, Jul. 2017.

[18] M. Yazdanian and A. Mehrizi-Sani, "Distributed control techniques in microgrids," *IEEE Trans. Smart Grid*, vol. 5, no. 6, pp. 2901–2909, Nov. 2014.

[19] S. Horowitz and A. G. Phadke, *Power System Relaying*. John Wiley & Sons, 2008.

[20] A. Yazdani and R. Iravani, *Voltage-Sourced Converters in Power Systems: Modeling, Control, and Applications*. Wiley-IEEE Press, 2010.

[21] B. Mahamedi, J. Zhu, M. Eskandari, L. Li, and A. MehriziSani, "Analysis of fault response of inverter-interfaced distributed generators in sequence networks," *IEEE Ind. Appl. Soc. Annu. Meeting (IAS)*, 2018.

[22] J. Wang and Y. Tang, "A fault-tolerant operation method for medium voltage modular multilevel converters with phase-shifted carrier modulation," *IEEE Trans. Power Electron.*, vol. 34, no. 10, pp. 9459–9470, Oct. 2019.

[23] B. Choudhury, A. Mohammadhassani, B. Alexander, R. Iyer, A. Mehrizi-Sani, J. H. Reed, and V. K. Shah, "Control coordination in inverter-based microgrids using aoi-based 5G schedulers," *IET Smart Grid*, Mar. 2023, under review.

[24] H. Ghaffarzadeh and A. Mehrizi-Sani, "Adaptive set point modulation to mitigate transients in power systems," *IET Gener., Transm. Distrib.*, vol. 14, no. 23, pp. 5463–5470, Dec. 2020.

[25] A. Mehrizi-Sani and R. Iravani, "Online set point modulation to enhance microgrid dynamic response: Theoretical foundation," *IEEE Trans. Power Syst.*, vol. 27, no. 4, pp. 2167–2174, Nov. 2012.

[26] A. Mehrizi-Sani and R. Iravani, "Online set point adjustment for trajectory shaping in microgrid applications," *IEEE Trans. Power Syst.*, vol. 27, no. 1, pp. 216–223, Feb. 2012.

[27] M. Syed, A. Mehrizi-Sani, M. Robowska, E. Guillo-Sansano, D. Wang, and G. Burt, "Dynamically robust coordinated set point tracking of distributed DERs at point of common coupling," *Intl. J. Elec. Power Energy Syst.*, vol. 143, no. 108481, 2022.

[28] A. Mohammadhassani, Y. Akbar, A. MehriziSani, and H. Wang, "Cyber vulnerability assessment of microgrids with 5G-enabled distributed control," *IEEE Power Energy Soc. General Meeting (PESGM)*, Jul. 2022.

[29] K. Li, L. Yuan, Z. Zhao, S. Lu, and Y. Zhang, "Fault-tolerant control of MMC with hot reserved submodules based on carrier phase shift modulation," *IEEE Trans. Power Electron.*, vol. 32, no. 9, pp. 6778–6791, Sep. 2017.

[30] S. Tan, J. M. Guerrero, P. Xie, R. Han, and J. C. Vasquez, "Brief survey on attack detection methods for cyber-physical systems," *IEEE Syst. J.*, vol. 14, no. 4, pp. 5329–5339, Dec. 2020.

[31] T. Meyers and B. Mather, "Empirical evaluation of GPS clock accuracy for isochronous droop-based inverters," *IEEE Energy Convers. Congr. Expo.*

(ECCE), Oct. 2021.

[32] B. Alexander, A. Mohammadhassani, and A. Mehrizi-Sani, "Resilient power sharing in a 100% inverter-based power system under GPS spoofing attacks," *IEEE Power Energy Soc. General Meeting (PESGM)*, Oct. 2023, accepted for publication.

[33] L. Tong, G. Xu, B. Hassibi, and T. Kailath, "Blind channel identification based on second-order statistics: a frequency-domain approach," *IEEE Trans. Inf. Theory*, vol. 41, no. 1, pp. 329–334, Jan. 1995.

[34] K. Jaganathan and B. Hassibi, "Reconstruction of signals from their autocorrelation and cross-correlation vectors, with applications to phase retrieval and blind channel estimation," *IEEE Trans. Signal Process.*, vol. 67, no. 11, pp. 2937–2946, Jun. 2019.

[35] L. Vandenberghe and S. Boyd, "Semidefinite programming," *SIAM Review*, vol. 38, no. 1, Mar. 1996.

[36] S. Arora, E. Hazan, and S. Kale, "Fast algorithms for approximate semidefinite programming using the multiplicative weights update method," *Annu. IEEE Symp. Found. Computer Sci. (FOCS)*, Oct. 2005.

[37] B. Huang, S. Jiang, Z. Song, R. Tao, and R. Zhang, "Solving SDP faster: A robust IPM framework and efficient implementation," *IEEE Annu. Symp. Found. Computer Sci. (FOCS)*, Oct. 2022.

[38] A. Mohammadhassani and A. Mehrizi-Sani, "Nonpilot directional protection of a microgrid," *IET Gener. Transm. Distrib.*, Apr. 2023, under review.

[39] A. Hooshyar, E. F. El-Saadany, and M. Sanaye-Pasand, "Fault type classification in microgrids including photovoltaic DGs," *IEEE Trans. Smart Grid*, vol. 7, no. 5, pp. 2218–2229, Sep. 2016.

[40] S. Venkata, M. Reno, W. Bower, S. Manson, J. Reilly, and G. Sey Jr., "Microgrid protection: Advancing the state of the art," *Sandia National Laboratories*, no. SAND2019-3167, Mar. 2019.

[41] X. Li, A. Dyko, and G. M. Burt, "Traveling wave-based protection scheme for inverter-dominated microgrid using mathematical morphology," *IEEE Trans. Smart Grid*, vol. 5, no. 5, pp. 2211–2218, Sep. 2014.

[42] K. A. Saleh, A. Hooshyar, and E. F. El-Saadany, "Ultra-high-speed traveling-wave-based protection scheme for medium-voltage DC microgrids," *IEEE Trans. Smart Grid*, vol. 10, no. 2, pp. 1440–1451, Mar. 2019.

[43] D. Liu, A. Dyko, Q. Hong, D. Tzelepis, and C. D. Booth, "Transient wavelet energy-based protection scheme for inverter-dominated microgrid," *IEEE Trans. Smart Grid*, vol. 13, no. 4, pp. 2533–2546, Jul. 2022.

[44] K. O. Oureilidis and C. S. Demoulias, "A fault clearing method in converter-dominated microgrids with conventional protection means," *IEEE Trans. Power Del.*, vol. 31, no. 6, pp. 4628–4640, Jun. 2016.

[45] Z. Chen, X. Pei, M. Yang, L. Peng, and P. Shi, "A novel protection scheme for inverter-interfaced microgrid (IIM) operated in islanded mode," *IEEE Trans. Power Electron.*, vol. 33, no. 9, pp. 7684–7697, Sep. 2018.

[46] A. Soleimanisardoo, H. Kazemi Karegar, and H. H. Zeineldin, "Differential frequency protection scheme based on off-nominal frequency injections for inverter-based islanded microgrids," *IEEE Trans. Smart Grid*, vol. 10, no. 2, pp. 2107–2114, Mar. 2019.

[47] K. Saleh, M. A. Allam, and A. Mehrizi-Sani, "Protection of inverter-based islanded microgrids via synthetic harmonic current pattern injection," *IEEE Trans. Power Del.*, vol. 36, no. 4, pp. 2434–2445, Aug. 2021.

[48] K. A. Saleh and A. Mehrizi-Sani, "Harmonic directional overcurrent relay for islanded microgrids with inverter-based DGs," *IEEE Syst. J.*, vol. 15, no. 2, pp. 2720–2731, Jun. 2021.

[49] E. Casagrande, W. L. Woon, H. H. Zeineldin, and D. Svetinovic, "A differential sequence component protection scheme for microgrids with inverter-based distributed generators," *IEEE Trans. Smart Grid*, vol. 5, no. 1, pp. 29–37, Jan. 2014.

[50] S. Kar, S. R. Samantaray, and M. D. Zadeh, "Data-mining model based intelligent differential microgrid protection scheme," *IEEE Syst. J.*, vol. 11, no. 2, pp. 1161–1169, Jun. 2017.

[51] J. J. Q. Yu, Y. Hou, A. Y. S. Lam, and V. O. K. Li, "Intelligent fault detection scheme for microgrids with wavelet-based deep neural networks," *IEEE Trans. Smart Grid*, vol. 10, no. 2, pp. 1694–1703, Mar. 2019.

[52] Working Group on Microgrid Protection Systems, "Microgrid protection systems," *IEEE Power and Energy Society*, no. PES-TR71, Aug. 2019.

[53] A. Mohammadhassani and A. Mehrizi-Sani, "A fault tolerant selective harmonic elimination method for modular multilevel converters," *IEEE Power Energy Soc. General Meeting*, Aug. 2020.

[54] V. V. Vijayachandran and U. J. Shenoy, "Implementation of support-vector-machine-based relay coordination scheme for distribution system with renewables," *IEEE J. Emerg. Sel. Top. Ind. Electron.*, vol. 2, no. 3, pp. 324–333, Aug. 2021.

[55] A. Srivastava and S. Parida, "A robust fault detection and location prediction module using support vector machine and Gaussian process regression for AC microgrid," *IEEE Trans. Ind. Appl.*, vol. 58, no. 1, pp. 930–939, Jan. 2022.

[56] *IEEE Standard for Interconnection and Interoperability of Distributed Energy Resources with Associated Electric Power Systems Interfaces*, IEEE Standard 1547-2018, Apr. 2018.

[57] K. Behrendt, N. Fischer, and C. Labuschagne, "Considerations for using harmonic blocking and harmonic restraint techniques on transformer differential relays," *SEL J. Reliable Power*, vol. 2, no. 3, Sep. 2011.

[58] C. M. Bishop, "Pattern recognition and machine learning," *Springer*, 2006.

[59] H. Farhangi and G. Joos, "Microgrid benchmarks," in *Microgrid Planning and Design: A Concise Guide*. Wiley-IEEE Press, 2019, ch. 2, pp. 25–36.

[60] A. Mohammadhassani and A. Mehrizi-Sani, "Open-circuit submodule fault diagnosis in MMCs using support vector machines," *IET Gener. Transm. Distrib.*, vol. 16, no. 24, pp. 5015–5025, Dec. 2022.

[61] S. Yang, A. Bryant, P. Mawby, D. Xiang, L. Ran, and P. Tavner, "An industry-based survey of reliability in power electronic converters," *IEEE Trans. Ind. Appl.*, vol. 47, no. 3, pp. 1441–1451, May 2011.

[62] X. Meng, J. Han, L. M. Bieber, L. Wang, W. Li, and J. Belanger, "A universal blocking-module-based average value model of modular multilevel converters with different types of submodules," *IEEE Trans. Energy Convers.*, vol. 35, no. 1, pp. 53–66, Mar. 2020.

[63] P. Hu, Z. He, S. Li, and J. M. Guerrero, "Non-ideal proportional resonant control for modular multilevel converters under sub-module fault condi-

tions," *IEEE Trans. Energy Convers.*, vol. 34, no. 4, pp. 1741–1750, Dec. 2019.

[64] J. Wang, H. Ma, and Z. Bai, "A submodule fault ride-through strategy for modular multilevel converters with nearest level modulation," *IEEE Trans. Power Electron.*, vol. 33, no. 2, pp. 1597–1608, Feb. 2018.

[65] B. Li, Y. Zhang, R. Yang, G. Wang, and D. Xu, "An IGBT open-circuit fault detection method for modular multilevel converters," *2015 Int. Conf. Power Electron. ECCE Asia (ICPE-ECCE Asia)*, Jun. 2015.

[66] S. Shao, A. J. Watson, J. C. Clare, and P. W. Wheeler, "Robustness analysis and experimental validation of a fault detection and isolation method for the modular multilevel converter," *IEEE Trans. Power Electron.*, vol. 31, no. 5, pp. 3794–3805, May 2016.

[67] H. Yang, W. Zhou, J. Sheng, H. Luo, C. Li, W. Li, and X. He, "A statistical submodule open-circuit failure diagnosis method for modular multilevel converters (MMCs) with variance measurement," *IEEE Open J. Power Electron.*, vol. 1, pp. 180–189, May 2020.

[68] Z. Geng, M. Han, Z. W. Khan, and X. Zhang, "Detection and localization strategy for switch open-circuit fault in modular multilevel converters," *IEEE Trans. Power Del.*, vol. 35, no. 6, pp. 2630–2640, Dec. 2020.

[69] Z. Wang and L. Peng, "Grouping capacitor voltage estimation and fault diagnosis with capacitance self-updating in modular multilevel converters," *IEEE Trans. Power Electron.*, vol. 36, no. 2, pp. 1532–1543, Feb. 2021.

[70] F. Deng, M. Jin, C. Liu, M. Liserre, and W. Chen, "Switch open-circuit fault localization strategy for MMCs using sliding-time window based fea-

tures extraction algorithm," *IEEE Trans. Ind. Electron.*, vol. 68, no. 10, pp. 10 193–10 206, Oct. 2021.

[71] Z. Ke, J. Pan, R. Na, K. Potty, J. Zhang, J. Wang, and L. Xu, "Single-submodule open-circuit fault diagnosis for a modular multi-level converter using artificial intelligent-based techniques," *IEEE Appl. Power Electron. Conf. Expo. (APEC)*, pp. 3056–3063, Mar. 2019.

[72] S. Venkatachari, A. Mohammadhassani, and A. Mehrizi-Sani, "Submodule fault detection in MMCs using support vector classification," *IEEE Innov. Smart Grid Tech. Conf. Eur.*, Oct. 2021.

[73] A. Ghazanfari and Y. A.-R. I. Mohamed, "New submodule improving fault-tolerant capability of modular multilevel converters," *IEEE Trans. Energy Convers.*, vol. 35, no. 2, pp. 662–671, Jun. 2020.

[74] F. Deng, Z. Chen, M. R. Khan, and R. Zhu, "Fault detection and localization method for modular multilevel converters," *IEEE Trans. Power Electron.*, vol. 30, no. 5, pp. 2721–2732, May 2015.

[75] A. A. Abdelsalam, A. A. Salem, E. S. Oda, and A. A. Eldesouky, "Islanding detection of microgrid incorporating inverter based DGs using long short-term memory network," *IEEE Access*, vol. 8, pp. 106 471–106 486, Jun. 2020.

[76] Q. Tu, Z. Xu, and L. Xu, "Reduced switching-frequency modulation and circulating current suppression for modular multilevel converters," *IEEE Trans. Power Del.*, vol. 26, no. 3, pp. 2009–2017, Jul. 2011.

[77] A. MohammadHassani and E. Babaei, "Exchange market algorithm for selective harmonic elimination in cascaded multilevel inverters," *13th Int. Conf. Theory Appl. of Fuzzy Syst. Soft Comp.*, pp. 594–601, Dec. 2019.

[78] J. Nalepa and M. Kawulok, "Selecting training sets for support vector machines: a review," *Artif. Intell. Rev.*, vol. 52, pp. 857–900, Jan. 2019.

[79] D. Zhou, H. Qiu, S. Yang, and Y. Tang, "Submodule voltage similarity-based open-circuit fault diagnosis for modular multilevel converters," *IEEE Trans. Power Electron.*, vol. 34, no. 8, pp. 8008–8016, Aug. 2019.

[80] A. Mohammadhassani and A. Mehrizi-Sani, "Fast and fault-tolerant model predictive control of mmcs under selective harmonic elimination," *IET Gener. Transm. Distrib.*, vol. 17, no. 1, pp. 240–251, Jan. 2023.

[81] P. W. Hammond and M. F. Aiello, "Multiphase power supply with series connected power cells with failed cell bypass," U.S. Patents US5 986 909A, 2001.

[82] J. Rodriguez, P. W. Hammond, J. Pontt, R. Musalem, P. Lezana, and M. J. Escobar, "Operation of a medium-voltage drive under faulty conditions," *IEEE Trans. Ind. Electron.*, vol. 52, no. 4, pp. 1080–1085, Aug. 2005.

[83] M. Aleenejad, H. Mahmoudi, S. Jafarishiadeh, and R. Ahmadi, "Fault-tolerant space vector modulation for modular multilevel converters with bypassed faulty submodules," *IEEE Trans. Ind. Electron.*, vol. 66, no. 3, pp. 2463–2473, Mar. 2019.

[84] P. Hu, D. Jiang, Y. Zhou, Y. Liang, J. Guo, and Z. Lin, "Energy-balancing control strategy for modular multilevel converters under submodule fault conditions," *IEEE Trans. Power Electron.*, vol. 29, no. 9, pp. 5021–5030, Sep. 2014.

[85] Q. Yang, J. Qin, and M. Saeedifard, "Analysis, detection, and location of open-switch submodule failures in a modular multilevel converter," *IEEE Trans. Power Del.*, vol. 31, no. 1, pp. 155–164, Feb. 2016.

[86] F. Deng, Y. Tian, R. Zhu, and Z. Chen, "Fault-tolerant approach for modular multilevel converters under submodule faults," *IEEE Trans. Ind. Electron.*, vol. 63, no. 11, pp. 7253–7263, Nov. 2016.

[87] Q. Yang, J. Qin, and M. Saeedifard, "A postfault strategy to control the modular multilevel converter under submodule failure," *IEEE Trans. Power Del.*, vol. 31, no. 6, pp. 2453–2463, Dec. 2016.

[88] Q. Xiao, J. Wang, Y. Jin, L. Chen, H. Jia, T. Dragievi, and R. Teodorescu, "A novel operation scheme for modular multilevel converter with enhanced ride-through capability of submodule faults," *IEEE J. Emerg. Sel. Top. Power Electron.*, vol. 9, no. 2, pp. 1258–1268, Apr. 2021.

[89] R. Razani and Y. A.-R. I. Mohamed, "Fault-tolerant operation of the DC/DC modular multilevel converter under submodule failure," *IEEE J. Emerg. Sel. Top. Power Electron.*, vol. 9, no. 5, pp. 6139–6151, Oct. 2021.

[90] S. Farzamkia, H. Iman-Eini, A. Khoshkbar-Sadigh, and M. Noushak, "A software-based fault-tolerant strategy for modular multilevel converter using DC bus voltage control," *IEEE J. Emerg. Sel. Top. Power Electron.*, vol. 9, no. 3, pp. 3436–3445, Jun. 2021.

[91] Y. Jin, Q. Xiao, J. Pou, H. Jia, Y. Ji, R. Teodorescu, and F. Blaabjerg, "A novel fault-tolerant operation approach for the modular multilevel converter-based STATCOM with the enhanced operation capability," *IEEE J. Emerg. Sel. Top. Power Electron.*, 2022, accepted for publication.

[92] S. Ziaeinejad, Y. Sangsefidi, and A. Mehrizi-Sani, "A generalized switching strategy and capacitor sizing algorithm for granular multilevel converters," *IEEE Trans. Ind. Electron.*, vol. 65, no. 6, pp. 4443–4453, Jun. 2018.

[93] M. Aleenejad, H. Mahmoudi, P. Moamaei, and R. Ahmadi, "A new fault-tolerant strategy based on a modified selective harmonic technique for three-phase multilevel converters with a single faulty cell," *IEEE Trans. Power Electron.*, vol. 31, no. 4, pp. 3141–3150, Apr. 2016.

[94] M. Aleenejad, H. Mahmoudi, and R. Ahmadi, "Multifault tolerance strategy for three-phase multilevel converters based on a half-wave symmetrical selective harmonic elimination technique," *IEEE Trans. Power Electron.*, vol. 32, no. 10, pp. 7980–7989, Oct. 2017.

[95] Siemens, "The smart way HVDC plus-one step ahead." [Online]. Available: https://www.energy.siemens.com/us/en/power-transmission/hvdc/hvdcplus/

[96] S. Yang, J. Fang, Y. Tang, H. Qiu, C. Dong, and P. Wang, "Modular multilevel converter synthetic inertia-based frequency support for medium-voltage microgrids," *IEEE Trans. Ind. Electron.*, vol. 66, no. 11, pp. 8992–9002, Nov. 2019.

[97] Q. Xiao, Y. Jin, L. Chen, X. Yu, H. Jia, H. Liu, R. Teodorescu, and F. Blaabjerg, "A simple operation approach for modular multilevel converter under grid voltage swell in medium-voltage microgrids," *IEEE Access*, vol. 7, pp. 147 280–147 291, Oct. 2019.

[98] A. Pérez-Basante, S. Ceballos, G. Konstantinou, J. Pou, J. Andreu, and I. M. de Alegría, "(2N+1) selective harmonic elimination-PWM for modular multilevel converters: A generalized formulation and a circulating current control method," *IEEE Trans. Power Electron.*, vol. 33, no. 1, pp. 802–818, Jan. 2018.

[99] D. Samajdar, T. Bhattacharya, and S. Dey, "A reduced switching frequency sorting algorithm for modular multilevel converter with circulating current suppression feature," *IEEE Trans. Power Electron.*, vol. 34, no. 11, pp. 10 480–10 491, Nov. 2019.

[100] S. Yang, P. Wang, Y. Tang, M. Zagrodnik, X. Hu, and K. J. Tseng, "Circulating current suppression in modular multilevel converters with even-harmonic repetitive control," *IEEE Trans. Ind. Electron.*, vol. 54, no. 1, pp. 298–309, Jan. 2018.

[101] R. P. Aguilera, P. Acuña, P. Lezana, G. Konstantinou, B. Wu, S. Bernet, and V. G. Agelidis, "Selective harmonic elimination model predictive control for multilevel power converters," *IEEE Trans. Power Electron.*, vol. 32, no. 3, pp. 2416–2426, Mar. 2017.

[102] Y. Sangsefidi, S. Ziaeinejad, and A. Mehrizi-Sani, "Low switching frequency-based predictive control of a grid-connected voltage-sourced converter," *IEEE Trans. Energy Convers.*, vol. 32, no. 2, pp. 686–697, Jun. 2017.

[103] A. Y. Fard and M. B. Shadmand, "Cooperative model predictive control scheme for dispersed smart inverters at the grid edge," *IEEE Texas Power Energy Conf.*, Feb. 2020.

[104] K. Yang, Q. Zhang, R. Yuan, W. Yu, J. Yuan, and J. Wang, "Selective harmonic elimination with groebner bases and symmetric polynomials," *IEEE Trans. Power Electron.*, vol. 31, no. 4, pp. 2742–2752, Apr. 2016.

[105] Working Group on Recommended Practices and Requirements for Harmonic Control in Electric Power Systems, "IEEE standard for harmonic control in electric power systems," Aug. 2022.

[106] M. Narimani, B. Wu, V. Yaramasu, and N. R. Zargari, "Finite control-set model predictive control (FCS-MPC) of nested neutral point-clamped (NNPC) converter," *IEEE Trans. Power Electron.*, vol. 30, no. 12, pp. 7262–7269, Dec. 2015.

[107] J. Pou, S. Ceballos, G. Konstantinou, V. G. Agelidis, R. Picas, and J. Zaragoza, "Circulating current injection methods based on instantaneous information for the modular multilevel converter," *IEEE Trans. Ind. Electron.*, vol. 62, no. 2, pp. 777–788, Feb. 2015.

[108] S. Yang, Y. Tang, and P. Wang, "Seamless fault-tolerant operation of a modular multilevel converter with switch open-circuit fault diagnosis in a distributed control architecture," *IEEE Trans. Power Electron.*, vol. 33, no. 8, pp. 7058–7070, Feb. 2018.